Commande d'un robot collaboratif redondant en interaction avec des humains dans un contexte de manipulation et d'assemblage

Thèse

Pascal Labrecque

Doctorat en génie mécanique
Philosophiæ doctor (Ph. D.)

Québec, Canada

Commande d'un robot collaboratif redondant en interaction avec des humains dans un contexte de manipulation et d'assemblage

Thèse

Pascal Labrecque

Sous la direction de:

Clément Gosselin, directeur de recherche

Résumé

Cette thèse présente deux nouvelles architectures de commande pour les interactions physiques humain-robot (pHRIs). Ces architectures sont spécifiquement développées dans une vision d'implantation en industrie pour les manipulations d'assemblage. En effet, deux types de robots collaboratifs adaptés à différentes contraintes de l'industrie et ayant des interfaces d'interactions physiques différentes sont étudiés en utilisant chacun leur propre architecture de commande.

Le premier robot collaboratif développé est un manipulateur entièrement actionné permettant des pHRIs dans son espace libre, c.-à-d., des interactions unilatérales, et des pHRIs lorsque ses mouvements sont contraints par un environnement quelconque, c.-à-d., des interactions bilatérales. Les interactions de l'humain peuvent s'effectuer sur n'importe quelles parties du robot grâce aux capteurs de couples dans les articulations. Cependant, si une amplification des forces de l'humain sur l'environnement est désirée, alors il est nécessaire d'utiliser le capteur d'efforts supplémentaire attaché au robot. Ceci permet à la commande, en combinant les lectures du capteur d'efforts à l'effecteur, d'utiliser le ratio des forces appliquées indépendamment par l'opérateur et par l'environnement afin de générer l'amplification désirée. Cette loi de commande est basée sur l'admittance variable qui a déjà démontré ses bénéfices pour les interactions unilatérales. Ici, l'admittance variable est adaptée aux interactions bilatérales afin d'obtenir un seul algorithme de commande pour tous les états. Une loi de transition continue peut alors être définie afin d'atteindre les performances optimales pour chaque mode d'interaction qui, en fait, nécessitent chacun des valeurs de paramètres spécifiques.

Le cheminement et les résultats pour arriver à cette première architecture de commande sont présentés en trois étapes. Premièrement, la loi de commande est implémentée sur un prototype à un degré de liberté (ddl) afin de tester le potentiel d'amplification et de transition, ainsi que la stabilité de l'interaction. Deuxièmement, un algorithme d'optimisation du régulateur pour les interactions bilatérales avec un robot à plusieurs ddls est développé. Cet algorithme vérifie la stabilité robuste du système en utilisant l'approche des valeurs singulières structurées (μ-analysis), pour ensuite faire une optimisation des régulateurs stables en fonction d'une variable liée à la configuration du manipulateur. Ceci permet d'obtenir une loi de commande variable qui rend le système stable de façon robuste en atteignant des performances optimales peu

importe la configuration des articulations du robot. La loi de commande trouvée utilise un séquencement de gain pour les paramètres du régulateur par admittance durant les interactions bilatérales. La stabilité et la performance du système sont validées avec des tests d'impact sur différents environnements. Finalement, la loi de commande en admittance variable optimale est implémentée et validée sur un robot manipulateur à plusieurs ddls (Kuka LWR 4) à l'aide de suivis de trajectoire pour des interactions unilatérales et bilatérales.

Le deuxième robot collaboratif développé est un manipulateur partiellement actif et partiellement passif. L'architecture mécanique du robot est appelée macro-mini. Tous les degrés de liberté actionnés faisant partie du macro manipulateur sont doublés par les articulations passives du mini manipulateur. Le robot est alors sous-actionné. L'opérateur humain interagit uniquement avec le mini manipulateur, et donc, avec les articulations passives ce qui élimine tous délais dans la dynamique d'interaction. Ce robot collaboratif permet de définir une loi de commande qui génère une très faible impédance lors des interactions de l'opérateur, et ce, même pour des charges utiles élevées. Malgré que des amplifications de force ne peuvent être produites, les interactions bilatérales ont une stabilité assurée peu importe la situation. Aussi, les modes coopératif et autonome du robot utilisent les mêmes valeurs de paramètres de commande ce qui permet une transition imperceptible d'un à l'autre. La nouvelle loi de commande est comparée sur plusieurs aspects avec la commande en admittance variable précédemment développée. Les résultats démontrent que cette nouvelle loi de commande combinée à l'architecture active-passive du macro-mini manipulateur, appelé uMan, permet des interactions intuitives et sécuritaires bien supérieures à ce qu'un système entièrement actionné peut générer. De plus, pour l'assistance autonome, une détection de collision avancée et une planification de trajectoire adaptée à l'architecture du robot sont développées. Des validations expérimentales sont présentées afin d'évaluer la facilité à produire des manipulations fines, de démontrer la sécurité du système et d'établir la viabilité du concept en industrie.

Abstract

This thesis presents two novel control architectures for physical human-robot interactions (pHRIs) which are specifically designed for the assembly industry. Indeed, two types of pHRI manipulators, each adapted to different industrial constraints and with different physical interaction interfaces, are studied each with their own control architecture.

The first pHRI manipulator designed is fully actuated and allows pHRIs in its free space, i.e., unilateral interactions, as well as pHRIs when its motion is constrained by the environment, i.e., bilateral interactions. The human force input can be applied on any of the manipulator's links because of the torque sensors in the robot joints. However, if a human force amplification is desired on the environment, then it is required to use the additional force sensor appended to the robot. Using this approach, combined with the signal of the force sensor at the end-effector, it is then possible to use the ratio between the human and environment forces in order to generate the desired amplification. This control law is based on the concept of variable admittance control which has already demonstrated its great benefits for unilateral interactions. Here, this concept is extended to bilateral interactions in order to obtain a single control algorithm for both states. A continuous transition can thus be implemented between both interaction modes which require different parameter values in order to achieve their optimal performance.

The workflow and results to achieve this first control architecture are presented in three steps. Firstly, the control law is implemented on a single-degree-of-freedom (dof) prototype in order to test the amplification and transition potential, as well as the stability of the interaction. Secondly, a control optimisation algorithm is developed for bilateral interactions with a multi-dof robot. This algorithm assesses the system's robust stability using the structured singular value approach (μ-analysis), to afterwards, optimize the stable controllers in relation to a manipulator's configuration-dependent variable. This approach leads to a variable control law yielding a robustly stable system that can reach optimal performances for any robot configuration. In fact, the admittance regulator parameters follow a gain scheduling paradigm for bilateral interactions. The stability and performance of the system are assessed using impact tests on different environments. Finally, the optimal variable admittance control law is implemented and validated on a multi-dof robot (Kuka LWR 4) using different trajectory

tracking tasks for unilateral and bilateral interactions.

The second pHRI manipulator designed is partially active and partially passive. The robot's mechanical architecture is known as a macro-mini. All actuated dofs — which are part of the macro manipulator — are doubled with passive joints — which are part of the mini manipulator. This robot is therefore underactuated. The human operator interacts solely with the mini manipulator and, thereby, solely with the passive joints which leads to an interaction dynamics free of any delay. It is possible with this pHRI manipulator to define a control law that yields an extremely low interaction impedance, even for heavy payloads. Despite the fact that force amplification is impractical with this kind of mechanism, bilateral interactions are stable for all sorts of contact. Moreover, the robot's cooperative and autonomous modes use similar control parameter values which enables an imperceptible transition from one mode to the other. The new control law is compared on different aspects with the previously-defined variable admittance control law. Results show that this new control law combined with the active-passive macro-mini manipulator, also known as uMan, leads to intuitive and safe interactions that are considerably superior to any interaction using a fully actuated manipulator. Furthermore, for the autonomous mode, an advanced collision detection and a specifically-adapted trajectory planning are developed. Experimental validations are presented in order to assess the ease of fine manipulation, to demonstrate the system's safety, and to establish the viability of the concept for the industry.

Table des matières

Liste des tableaux

Liste des figures

Liste des vidéos

Toutes les vidéos sont disponibles à l'adresse suivante :

http://robot.gmc.ulaval.ca/publications/these-de-doctorat

à la section [36] Pascal Labrecque.

À mes parents,
À mes frères et soeurs,

Et à ma tendre moitié, Myriam.

There is not much good spending
twelve hours a day in a black hole
in the ground all your life long if
there's nothing there, no secret,
no treasure, nothing hidden.

Ursula K. Le Guin

Remerciements

Toutes ces années d'études ont été possibles grâce à mes parents qui m'ont, non seulement supporté de façon inconditionnelle, mais qui m'ont surtout appris à m'émerveiller face à la connaissance et à la compréhension des éléments qui nous entourent, que ça soit par la lecture, les voyages, les discours sur la vie, ou même, la multitude d'activités et de repas exotiques que peu de jeunes avaient la chance d'essayer. Merci.

Merci, au reste de ma famille et à mes amis proches qui avec leurs taquineries sur mon amour de l'école m'ont poussé à me dépasser, car l'amour de l'école c'est aussi l'amour du savoir et du partage de la connaissance.

Évidemment, merci à mon autre famille, sans qui je n'aurais pas passé quatre aussi belles années au doctorat...ça aurait pu être les sept pires. Merci, en particulier, à notre père au laboratoire, Clément, qui sait nous faire sentir plus que bienvenus à son bureau et qui, avec son calme et son optimisme (et bien-sûr son savoir quasi-infini), nous redonne toujours la foi en nos capacités de chercheur. Avec vous, on a le sentiment que chacune de nos petites avancées est un grand pas pour l'humanité. Merci pour les acquis sur le savoir-faire, mais surtout, sur le savoir-être, car on se rappelle rarement les gestes ou les paroles, mais on se souvient toujours de comment on s'est senti avec quelqu'un. Merci aussi à Thierry et Simon, sans qui, je n'aurais jamais pu avoir accès à un aussi beau terrain de jeux pour mes expérimentations. Mention spéciale à Simon pour avoir accepté de redémarrer avec moi les after-lunch gaming sessions. À Dinh aussi, le VP Activités Sociales, qui était toujours prêt pour une discussion de robotique à l'appartement.

Merci à André Desbiens, qui m'a apporté une compréhension pratique de ce monde à part qu'est la théorie de la commande et qui n'a jamais hésité à me donner des conseils. Acquis important : Tant qu'un système n'a pas été poussé à ses limites, tu ne peux pas connaître son plein potentiel.

Thanks to Muhammad Abdallah who made, with his great involvement and his valuable input, this industrial collaboration project an enriching experience.

Finalement, merci à ma compagne de vie, Myriam, qui est toujours là pour moi, même lorsque je décide de partir plusieurs années faire un doctorat dans une autre ville. Love you.

Avant-propos

La thèse présentée ici est sous la forme d'une thèse par articles. Il est donc nécessaire de donner le statut des articles en date de la soumission de la thèse ainsi que ma contribution à chacun d'eux. Il est important de noter que certains articles ont aussi été modifiés afin de diminuer les répétitions ou afin de donner plus de détail sur les travaux de recherche. Pour une lecture plus efficace, les informations relatives à chaque chapitre, c.-à-d., chaque article, sont données en points de forme.

• **Chapitre 1** :
Titre : *Robotic Force Amplification with Free Space Motion Capability*
Type d'article : Article de conférence, ICRA 2014.
Statut : Publié, 29 septembre 2014.
Contribution : Auteur principal. Écriture, conception et expérimentation faites par l'auteur principal.
Coauteurs : Prof. Clément Gosselin a supervisé activement la réalisation et la finalité de cet article.
Modifications : Quelques références d'article ont été ajoutées dans l'introduction.

• **Chapitre 2** :
Titre : *Performance Optimization of a Multi-DOF Bilateral Robot Force Amplification using Complementary Stability*
Type d'article : Article de conférence, MSC 2015.
Statut : Publié, 05 novembre 2015.
Contribution : Auteur principal. Écriture, conception et expérimentation faites par l'auteur principal.
Coauteurs : Prof. Clément Gosselin a supervisé activement la réalisation et la finalité de cet article.
Modifications : Plusieurs ajouts ont été faits dans la thèse afin de permettre une compréhension plus approfondie de l'algorithme proposé dans l'article de conférence. Les ajouts sont les suivants,

— une section présentant la structure générale du processus d'optimisation

— une structure de régulateur additionnelle à titre comparatif lors de l'optimisation (régulateur lead-lag)

— un environnement additionnel pour les tests d'impact (ressort)

— un exemple d'effet potentiel d'adhésion lors du passage bilatéral à unilatéral

— les développements mathématiques détaillés pour l'évaluation du système contrôlé

— quelques considérations importantes pour l'utilisation d'une analyse de stabilité robuste.

• **Chapitre 3** :

Titre : *Variable Admittance for pHRI : from Intuitive Unilateral Interaction to Optimal Bilateral Force Amplification*

Type d'article : Article de journal, Robotics and Computer-Integrated Manufacturing.

Statut : Soumis, 17 octobre 2016.

Contribution : Auteur principal. Écriture, conception et expérimentation faites par l'auteur principal.

Coauteurs : Prof. Clément Gosselin a supervisé activement la réalisation et la finalité de cet article.

Modifications : Afin de ne pas répéter la revue de littérature de l'article du Chapitre 1 qui était semblable, l'introduction a été réduite.

• **Chapitre 4** :

Titre : *uMan : A Low-Impedance Manipulator for Human-Robot Cooperation Based on Underactuated Redundancy*

Type d'article : Article de journal, IEEE-ASME Transactions on Mechatronics.

Statut : Publié, 16 janvier 2017.

Contribution : Auteur principal. Écriture (en majeure partie) et expérimentation faites par l'auteur principal.

Coauteurs : La conception des articulations horizontales du mini manipulateur ainsi qu'une partie de la section expliquant ce mécanisme ont été faites par Thierry Laliberté (mécanisme de Chebyshev modifié). La conception de l'articulation verticale du mini manipulateur ainsi qu'une partie de la section expliquant ce mécanisme ont été faites par Simon Foucault (mécanisme de Sarrus modifié). Muhammad Abdallah de chez General Motors et Prof. Clément Gosselin ont supervisé activement la réalisation et la finalité de cet article, ainsi que tout le processus de conception.

Modifications : L'article initial a dû être raccourci afin d'être conforme aux exigences du journal. Pour ce qui est de la thèse, toutes les sections et images ont été gardées. Ceci inclut

— une image montrant l'effet du paramètre non linéaire $K_{NL}f_{NL}$

— une section présentant l'algorithme de planification de trajectoire

— une section présentant une tâche de manipulation supplémentaire, c.-à-d., une simulation d'insertion de batteries dans une voiture

— une section expliquant les vidéos complémentaires.

D'autres éléments ont aussi été insérés afin de bien présenter l'intégralité du projet de recherche.

— une image montrant la machine d'état (State Machine, SM) utilisée pour les tâches d'assemblage

— une image montrant l'interface graphique utilisée avec le uMan

— une description des résultats des tests de réduction de l'impédance ressentie à l'effecteur avec le premier prototype. Les éléments de cette section, ajoutée en annexe de ce chapitre, viennent de Labrecque et al. [2016].

Introduction

Contexte et problématique générale

L'assemblage représente une portion significative dans la fabrication de produits complexes comme les automobiles. Étant donné la dextérité et l'adaptabilité requises pour les tâches d'assemblage, celles-ci sont le plus souvent effectuées par des opérateurs humains. Cela implique la manipulation de plusieurs pièces de taille et de poids importants engendrant des postures non-ergonomiques. Pour palier à ces contraintes, supporter les charges importantes et assurer une certaine normalisation des forces d'assemblage requises, des dispositifs d'assistance passifs sont utilisés depuis des décennies dans l'industrie.

FIGURE 0.1 – Exemple de tâche non-ergonomique en assemblage automobile

Depuis quelques temps, des dispositifs d'assistance actifs commencent à faire leur apparition en industrie [Akella et al., 1999, Colgate et al., 2003, Lecours et al., 2012]. En plus de supporter le poids des pièces à manipuler, ces nouveaux dispositifs fournissent aux opérateurs une assistance mécanique pour le déplacement et la manipulation des charges. Également, certains de ces dispositifs proposent un mode de déplacement autonome, par exemple, pour amener et présenter des pièces à l'opérateur.

Cependant, ces modes autonomes sont, en réalité, inutilisables dans l'espace de travail de l'opé-

rateur, car les risques de collisions dommageables sont trop élevés. Les dispositifs d'assistance actifs demeurent donc confinés essentiellement à deux tâches spécifiques, à savoir, supporter le poids d'une charge et assister un opérateur pour la déplacer. L'opérateur reste alors encore seul à réaliser toutes les tâches d'assemblage.

Malheureusement, les opérations d'assemblage ont tendance à introduire des contraintes ergonomiques qui exposent les travailleurs à des situations posant des risques pour leur santé et leur sécurité. Il est donc fort désirable de développer des solutions impliquant directement la robotique dans les tâches complexes d'assemblage. Ce désir a donc mené à l'élaboration d'un projet qui a pour but de développer une assistance robotique sécuritaire et fiable capable d'interagir directement avec des opérateurs. Plus spécifiquement, cette recherche vise à concevoir et fabriquer un manipulateur redondant qui devra avoir les capacités physiques (amplitude de mouvements et forces) comparables à celles d'un humain. Il devra aussi avoir une adaptabilité et une répétabilité lui permettant d'être utilisé pour une multitude de tâches. Le manipulateur devra pouvoir participer à toutes les étapes des différents procédés tel que la collecte des pièces, l'approche des pièces au montage avec ou sans l'aide directe de l'opérateur et l'insertion des pièces avec l'opérateur. Cette coopération entre l'opérateur et le robot lors des assemblages amènera une nouvelle normalisation des procédés, autant au niveau du temps d'opération (efficacité) qu'au niveau de la qualité du montage.

Problématique spécifique à la commande

La commande pour les robots sur les chaînes de production industrielle est bien connue et ce depuis plusieurs dizaines d'années. En effet, les techniques de commande ont été peaufinées au fil des ans afin d'effectuer des tâches tel que les positionnements cartésien et articulaire, la planification et le suivi de trajectoire, la prise d'objets et l'application de forces constantes à l'effecteur. Cependant, la problématique générale du projet de recherche fait intervenir plusieurs aspects novateurs de la commande en robotique industrielle dû à l'interaction physique de l'humain.

En effet, afin d'implanter un manipulateur redondant interagissant dans l'espace de travail d'un humain, la sécurité, la robustesse, l'adaptabilité et le contrôle intuitif doivent être vus sous un nouvel angle. Le côté coopératif entre humains et robots émerge tranquillement dans l'industrie et n'en est donc encore qu'à ses débuts, surtout pour ce qui a trait au rendement. La commande par contact direct ou par contact avec l'objet manipulé est un des aspects prédominants des recherches contemporaines en robotique coopérative, mais les différentes interactions potentielles (unilatérales et bilatérales) apportent des changements de dynamique drastiques qui n'ont pas encore été résolus efficacement. Il est donc important, dans le contexte industriel actuel, de développer un algorithme de commande en lien avec les forces d'interaction (environnement, robot, opérateur) et avec le positionnement fin de la pièce manipulée.

Objectifs de recherche

Deux objectifs principaux reliés à la commande sont posés initialement pour la réalisation de ce projet de recherche. Ces objectifs sont divisés en sous-objectifs de la façon suivante :

1. Développer des algorithmes de commande afin de permettre au robot d'interagir simultanément avec l'opérateur humain et l'environnement, et ce, afin d'effectuer des tâches d'assemblage réelles :
    - Comparer de façons quantitative et qualitative les performances de plusieurs algorithmes de commande.
    - Définir la commande adéquate pour un manipulateur à sept degrés de liberté à l'aide des résultats de performance.
2. Développer une interface sensible et des techniques de programmation intuitives qui permettront aux utilisateurs une interaction et une collaboration aisées et versatiles :
    - Comparer de façons quantitative et qualitative les performances dues aux emplacements, aux nombres et aux types de capteurs utilisés.
    - Définir l'interface sensible adéquate à l'aide des résultats de performance.
    - Développer une technique de programmation par contact direct (guidage et apprentissage par l'opérateur).

Méthodologie et plan de la thèse

Afin d'atteindre les objectifs de recherche, il est nécessaire d'élaborer une méthodologie couvrant la conception, le développement et l'expérimentation. Les chapitres de la thèse suivent en grande partie la méthodologie posée initialement. Évidemment, et heureusement, les résultats de chaque étape ont permis d'orienter la recherche pour en arriver au robot collaboratif idéal pour le contexte industriel désiré. Ici, le contexte général de départ était une manipulation d'assemblage demandant des contacts soutenus entre les pièces à assembler et des actions d'insertion. Cela inclut donc

- des interactions physiques entre l'humain et le robot dans l'espace libre afin de déplacer les pièces (interactions unilatérales),
- des interactions conjointes de l'humain et du robot sur un environnement stationnaire afin d'appliquer des forces d'insertion ou de serrage (mouvements contraints, interactions bilatérales),
- des contacts avec des environnements rigides,

- des manipulations fines et précises et
- une amplification de force ou un blocage des articulations afin de réduire les efforts soutenus par l'opérateur.

Ainsi, suivant les objectifs et les éléments du contexte général, la méthodologie peut être définie de façon systématique.

Tout d'abord, il est nécessaire de concevoir un prototype d'interaction physique humain-robot (pHRI) à un degré de liberté (ddl) afin de tester différents algorithmes de commande permettant des interactions unilatérales et bilatérales (amplification de force), tel que, la commande en force, en admittance ou en impédance. Cette étape est couverte par l'article de conférence présenté au Chapitre 1.

Par la suite, il est désiré d'optimiser la performance de la commande pour les interactions bilatérales, et ce, pour un robot manipulateur à plusieurs degrés de liberté. Les interactions unilatérales ne nécessitent pas une optimisation du même genre, car le haut niveau de performance a déjà été établi pour le type de commande choisi au final, et car le sentiment de confort d'interactions est subjectif à chaque individu. Cette étape est couverte par l'article de conférence allongé présenté au Chapitre 2.

Puis, il faut adapter et tester la solution optimale précédemment trouvée à un robot manipulateur à sept ddls (Kuka LWR 4) afin d'obtenir une architecture de commande couvrant tous les aspects reliés au contexte d'assemblage. L'article de journal du Chapitre 3 présente les démarches et résultats de cette étape.

Ensuite, différents types d'interaction (ex : emplacements et types de capteurs, types de commande, insertions, pick-and-place, suivis de trajectoire) doivent être testés avec l'architecture du robot conçu en parallèle par d'autres membres du projet de recherche et qui cible des tâches d'assemblage spécifiques. Durant cette étape, il est aussi nécessaire de comparer l'architecture de commande élaborée précédemment avec des commandes typiques relatives à l'architecture particulière du robot final. Pour la thèse, seul les comparatifs entre la commande développée initialement et la commande finale (partielle et complète) sont présentés au Chapitre 4.

Par après, il est essentiel de définir la loi de commande la mieux adaptée pour le type d'architecture du robot collaboratif final incluant des modes coopératif et autonome, des techniques de programmation conviviales et une détection de collision. Cette étape est couverte par l'article de journal allongé du Chapitre 4.

Finalement, le robot collaboratif proposé et sa commande doivent être validés avec des expérimentations standards et avec des simulations de tâches d'assemblage réelles définies en cours de projet. Cette étape est aussi couverte par l'article de journal allongé du Chapitre 4.

Chapitre 1

Robotic Force Amplification with Free Space Motion Capability

Résumé

Une architecture de commande basée sur l'admittance variable est proposée pour une amplification de force en coopération humain-robot. Cette commande est efficace pour les interactions physiques autant dans l'espace libre que lorsque les mouvements du manipulateur sont contraints. Ceci est possible grâce à une transition active entre les deux modes. La loi de commande variable permet aussi d'annuler les oscillations à hautes fréquences qui peuvent apparaître lors de contacts avec des surfaces rigides. Une analyse mathématique de l'architecture de commande est présentée et une validation expérimental préliminaire pour un banc d'essai à 1 degré de liberté est effectuée.

1.1 Introduction

In recent years, human-robot interaction (HRI) has attracted a great deal of attention in the robotics community, mainly because of the significant potential benefits of an active collaboration between humans and robots (Haddadin et al. [2011], Tsarouchi et al. [2016]). The help of a robotic assistant is indeed highly desirable for precision tasks, heavy load manipulation, rehabilitation and many other tasks. Moreover, the quality and the accessibility of the different interactive sensors allow researchers to develop more effective and intuitive interfaces. The most direct interaction between humans and robots is through physical contact ([De Santis et al., 2008]). In such a situation, the communication is therefore mainly accomplished via the interaction forces.

In industry, this approach has been applied to the assisted manipulation of heavy loads (Akella et al. [1999]). Moreover, some of the assistive devices recently developed can actively interpret the operator's intention to move the payload and make use of static balancing to reduce the required power (Lecours et al. [2012], Mörtl et al. [2012]). This kind of physical human-robot

interaction (pHRI) is also used in exoskeletons, sometimes called body extenders. In this context, the actions are completely commanded by the human operator inside the robotic suit (Kazerooni [1990], Montagner et al. [2007]). A typical solution for unilateral pHRI is to make use of an admittance regulator (Lecours et al. [2012], Ficuciello et al. [2014]). However, if a contact with the environment is required, the dynamics of the system changes and becomes more complex (Eppinger and Seering [1987]). Furthermore, in order to obtain a real assistance from the robot, the force applied by the operator should be augmented at the end-effector. It is therefore desirable to implement a controller that can take into account both free space and constrained situations. An early solution to this problem was formulated in Kosuge et al. [1993] using the concept of Virtual Tool Dynamics. More recently, Lamy et al. [2010] presented a force amplification controller for industrial applications, but emphasized the constrained case.

Currently, the most common application of pHRI is for assistive surgical systems. The interaction can take place through telerobotics (Pitakwatchara et al. [2006]) with a force feedback to a haptic device manipulated by the operator, or through direct contact with the surgical robot (Roy and Whitcomb [2002], Cagneau et al. [2008], Yen and Hung [2013]). An interesting approach is presented in Pitakwatchara et al. [2006] where the master PI controller switches to a simple P controller when the force sensed between the slave and the environment exceeds a certain threshold in order to keep the system stable. Similarly, Yen and Hung [2013] uses adaptive fuzzy logic for the inner position control loop to handle the varying resistive forces of the parallel robot mechanism. The major differences between the medical and the industrial fields are the range of the working space and the force enhancement sensed on the operator side. Indeed, the displacement and the force applied by the surgeon are decreased at the tool for more precision whereas force amplification and large workspaces are required in industrial applications. These differences lead to quite similar control architectures but to different physical issues to be addressed. For instance, if the operator force input is amplified at the end-effector, there is a higher risk of exciting the system into an unstable mode, especially when a high velocity contact occurs with a rigid surface. Industrial cooperation robots must deal with larger workspaces, higher velocities and larger forces, but they still need precision for complex tasks.

In this chapter, an effective force amplification controller based on the admittance model presented in Lecours et al. [2012] is proposed for pHRI industrial applications. The first section of the chapter describes the proposed control architecture. The second section investigates the impact of the different parameters on the dynamics of the system, briefly recalls the free space motion control law (Lecours et al. [2012]), and presents a continuous control law used for mode transition. The third section presents a discontinuous control law that allows the system to cancel undesirable behaviours. The last section provides an experimental demonstration of the controller's effectiveness. Here, the term free space motion refers to the mode in which the robot end-effector is able to move in its free space with the help of a physical interaction, also

known as, unilateral interaction. By contrast, in the constrained mode, the human interaction helps the robot end-effector to rest against a rigid environment and apply a force, also known as, bilateral interaction.

1.2 Control architecture

Cooperative force amplification implies a direct contact between the robot and the human operator, and thus force sensors are required to measure the operator input and the environment output. For simplification purposes, the analysis and the experiments presented in this chapter are developed for a one-degree-of-freedom (dof) robot. Therefore, the system includes only two force sensors, one for the input and one for the output. However, the proposed approach is easily extended to a multi-dof robot using the Jacobian matrix. If the robot is in contact with its environment and no motion is possible, it is easy to implement a direct force control with a certain amplification factor included in the loop (Cagneau et al. [2008]). However, when the system is not constrained by its environment and is required to move freely in its working space, the direct force control becomes inefficient for a precise positioning or for velocity control. Force control alone is thus not an adequate option for a system that must be able to operate in both constrained and free spaces. A possible approach to address the latter issue is admittance control, which allows the transformation of a force into a motion, namely position or velocity (Lecours et al. [2012], Lamy et al. [2010], Yen and Hung [2013]). The admittance is derived from the impedance that captures the relationship between motion and force. These two terms have been loosely used in the literature in the past years, but for the purposes of this thesis impedance represents the transformation of a motion into a force while admittance represents the opposite, as stated previously.

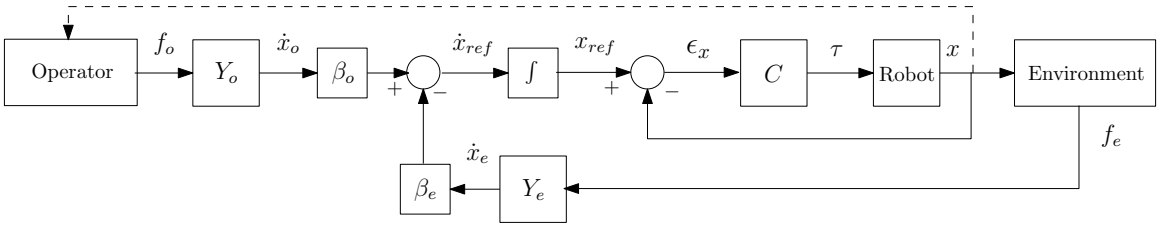

FIGURE 1.1 – Architecture of the enhanced admittance controller for a pHRI force amplification.

Fig. 1.1 presents the architecture proposed for the cooperative force controller. Variables f_o, Y_o, $\dot{x}_o$, and β_o represent respectively the force applied by the operator, the operator admittance relationship, the resulting operator velocity, and the operator amplification factor while f_e, Y_e, $\dot{x}_e$, and β_e are defined similarly for the environment. Variables x_{ref}, x, and ϵ_x are the desired position, the actual position, and the error between these two positions while τ is the torque command to the robot. The controller includes two loops, namely, an inner loop for the precise positioning and an outer loop for the transformation of the different forces interacting with

the robot into desired motions. The components of the controller are explained in more detail in the following subsections.

1.2.1 Inner position control loop

The first basic principle when using admittance control is to include an inner motion control. This controller, represented by C in Fig. 1.1, is used to follow a desired velocity or position. In the context of force amplification, a position control is more intuitive considering the strong relationship between a displacement and a force acting on an object having a certain stiffness (Hooke's law). Furthermore, the possibility to use the same controller for autonomous free space motion is an advantage. Due to the position control, an integral term appears in the closed loop which introduces an additional pole in the system dynamics. Implementing a PID regulator would thereby potentially compromise the stability of the system with a second additional integral, it is therefore wise to choose a PD regulator for the inner controller. Indeed, the derivative action introduces a zero that provides phase lead, and thus tends to stabilize the closed-loop system. The PD control law is written as

$$\tau = k_p(x_{ref} - x) + k_d(\dot{x}_{ref} - \dot{x}) \tag{1.1}$$

where k_p and k_d are respectively the proportional and the derivative gains.

1.2.2 Outer force control loop

The second basic component of an admittance control architecture is the transformation of the input force into a motion command. Typically, the relationship is of the form

$$f = m(\ddot{x} - \ddot{x}_t) + c(\dot{x} - \dot{x}_t) + k(x - x_t) \tag{1.2}$$

where f is the external force, m, c, and k are respectively the virtual inertia, damping and stiffness, $\ddot{x}$, $\dot{x}$, and x are the acceleration, the velocity, and the position, and finally, $\ddot{x}_t$, $\dot{x}_t$, and x_t represent the desired trajectory to be followed. Since the input is coming from a physical interaction, the latter three variables should be set to zero. The virtual stiffness, k, should also be equal to zero in order to obtain a free motion. The relationship is then rewritten as follows

$$f = m\ddot{x} + c\dot{x}. \tag{1.3}$$

It is then easy to solve the above equation for the velocity in the Laplace domain, yielding

$$\dot{X}(s) = \frac{1}{ms + c}F(s) = \frac{\frac{1}{c}}{\frac{m}{c}s + 1}F(s) = Y(s)F(s) \tag{1.4}$$

where $\dot{X}(s)$ and $F(s)$ are respectively the Laplace transforms of $\dot{x}$ and f, $Y(s)$ is the admittance, and s is the Laplace variable.

Since there is a force amplification situation, a feedback from the sensed environment force is necessary. Therefore, an admittance regulator is used for each sensed force, namely, the operator force and the environment force. The outer force control law is then based on the following relationships

$$x_{ref} = \int (\beta_o \dot{x}_o - \beta_e \dot{x}_e) dt, \tag{1.5}$$

$$f_o = m_o \ddot{x}_o + c_o \dot{x}_o \tag{1.6}$$

$$f_e = m_e \ddot{x}_e + c_e \dot{x}_e. \tag{1.7}$$

Equations (1.6) and (1.7) can be rewritten as

$$\dot{x}_o = \frac{f_o - m_o \ddot{x}_o}{c_o}, \tag{1.8}$$

$$\dot{x}_e = \frac{f_e - m_e \ddot{x}_e}{c_e}. \tag{1.9}$$

Moreover, when x_{ref} reaches a steady state, the expression inside the integral of (1.5) is then equal to zero, i.e.,

$$\beta_o \dot{x}_o - \beta_e \dot{x}_e = 0. \tag{1.10}$$

Substituting (1.8) and (1.9) into (1.10), assuming very small (negligible) virtual inertia, and assuming both virtual damping coefficients to be equal to $c_o = c_e = c$ then leads to

$$\frac{\beta_o f_o - \beta_e f_e}{c} = 0 \tag{1.11}$$

which finally yields

$$f_e = \frac{\beta_o}{\beta_e} f_o = \beta f_o. \tag{1.12}$$

Hence, a force amplification factor β is obtained based on the amplification factors β_o and β_e, that are respectively applied to the operator and the environment admittances.

1.3 Controller parameters

1.3.1 Stability limits

Stability is of paramount importance in pHRI. Assessing stability is a difficult problem that generally requires more than simple simulations, mainly because of the difficulty to accurately model human input. Also, a limit cycle, characterized by a constant oscillation around a steady state, is also an unwanted situation that is more difficult to predict than clear divergence. Limit cycles produce vibrations and are mostly encountered in the constrained mode because of the particular system dynamics (Eppinger and Seering [1987]). Indeed, in this situation, the environment stiffness, sensor dynamics, and low-pass filtering alter the stability bandwidth, and the controller becomes thus less tolerant to high frequency inputs. This is a common

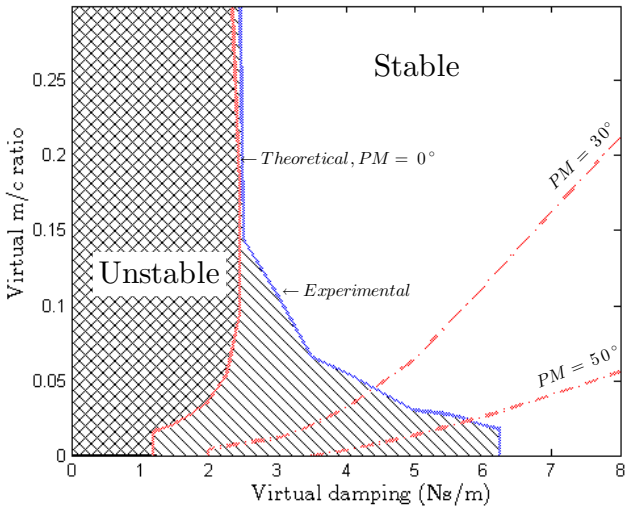

FIGURE 1.2 – Stability limits for the theoretical model and for the experimental setup including the 30° and 50° phase margin limits for the theoretical model.

issue in force control, and it is one major reason to pay a special attention to stability in the constrained mode.

Dynamic linear models of the prototype and the environment described in subsection 1.5.1 have been determined experimentally in order to simulate the robot behaviour. With the constrained system model, the stability limit in terms of the admittance parameters has been estimated and is shown in Fig. 1.2. In this case, Y_o and Y_e are identical, $\beta_o = 1$, and $\beta_e = 1/3$. In simulation, the gain and phase margins on the external open loop have been used to assess the system's stability boundary. The inner loop is already considered as stable, thereby the closed system is defined as stable if the external open loop gain margin is greater than 0dB and the phase margin is greater than 0°. Experimentally, when the system was entering a limit cycle it was not considered stable. The region of instability determined experimentally is larger than the region determined by simulation. This can be explained by two factors. The first one is the imperfect model used in the simulation which also includes model simplifications such as the nonlinearities of the system which were not considered. The second one is the discontinuous contact with the environment when large oscillations occur. It should also be noticed, when looking at the phase margin trend, that, in order to obtain a more robust system, a small m/c ratio is needed. Another parameter that affects the response stability is the amplification factor β_e. In simulation, the system becomes unstable when $\beta_e > 1.7$ while experimentally it becomes unstable when $\beta_e > 0.45$.

In summary, in order to obtain the best performance, the admittance parameters should be as small as possible without crossing the stability limit while β_e, on the other hand, should be as large as possible also without crossing its own stability limit.

1.3.2 Amplification for Low and High Admittances

Continuous control law during free space motion

The first order system defined in (1.4) has a well-known behaviour in the time domain. It is therefore easy to infer the effect of the parameters on the system response for a free space motion situation, namely, the virtual damping defines the response's steady state magnitude while the ratio of the virtual inertia over the virtual damping defines the time required to reach this steady state. The resulting dynamics, when applying an external force, can be considered as that of a mass, m, moving in a viscous environment of damping coefficient, c. Therefore, if the admittance parameters are high then the robot will be less reactive to the sensed force. On the other hand, if they are low it will be easier to move the robot, but more difficult to control it for precise motion. In fact, it has been shown that the most intuitive pHRI can be obtained by varying the admittance parameters online according to the operator's intentions (Lecours et al. [2012], Duchaine and Gosselin [2007], Tsumugiwa et al. [2001]). The approach proposed in (Lecours et al. [2012]) is used here and is now briefly recalled. In this approach, the effective damping coefficient, noted c_{ov}, is calculated based on the nominal (default) damping coefficient, c_o, and the desired acceleration, $\ddot{x}_d$, using

$$c_{ov} = \begin{cases} c_o - \alpha|\ddot{x}_d| & \text{for acceleration} \quad (1.13) \\ c_o + \alpha|\ddot{x}_d| & \text{for deceleration} \quad (1.14) \end{cases}$$

where parameter α is used to adjust the influence of the acceleration, or deceleration, on the variation of c_{ov}. When it is desired to accelerate, the virtual damping decreases and the effective virtual inertia, noted m_{ov}, is also adjusted in order to keep a constant ratio of damping over inertia, which preserves the transient dynamics and makes it easier to move the robot for larger accelerations. However, when it is desired to decelerate, the virtual damping increases, and the virtual inertia partially decreases using an exponential relationship in order to maintain a continuous parameter variation. The following relations are used to adjust the virtual inertia

$$m_{ov} = \begin{cases} \dfrac{m_o c_{ov}}{c_o} & \text{for acceleration} \quad (1.15) \\ \dfrac{m_o c_{ov}}{c_o}(1 - \eta(1 - e^{\gamma(c_o - c_{ov})})) & \text{for deceleration} \quad (1.16) \end{cases}$$

where m_o is the nominal virtual inertia and η and γ are parameters that are used to respectively adjust the steady state inertia to damping ratio and the rate of the transition. In the above, the desired acceleration, $\ddot{x}_d$, is computed using a discrete form of (1.6).

Transition between free space motion and constrained force amplification

As explained in the preceding subsection, in a constrained situation the properties of the environment strongly affect the dynamics of the system. In fact, the stiffness and damping of the contact surface reduce the closed-loop stability bandwidth. On the control architecture side, the feedback admittance can also contribute to instability by acting like a low-pass filter.

The admittance parameters should therefore be chosen carefully. First, both virtual dynamic systems should be identical in order to behave similarly in the process while parameters β_o and β_e take care of the amplification. Moreover, considering Y_o and Y_e as low-pass filters, it becomes obvious that it is not desirable to have one force signal filtered more severely than the other before the subtraction operation is applied. Second, the operator and the environment admittance parameters should be as low as possible while remaining numerically stable. Indeed, lowering these parameters leads to better performances but also reduces the interaction bandwidth, i.e., the robustness. The virtual damping parameters are particularly important because if they are too high the response contains uncontrollable overshoots, due to numerical instability, while if they are too low the stability limit is reached.

A recurrent issue for hybrid position/force control algorithms is the *jittering effect* that appears when the controller is flickering between two states. In the context considered here, the robot should react to two different dynamics, namely, free space and constrained space. In order to obtain the best performances for each case, the controller should take into account these two different modes. The advantage of the admittance control approach proposed here over a hybrid approach is that the behaviour of the controller can be easily modified by a parameter variation without changing the controller architecture (no commutation). Using this feature, it is then possible to define a smooth transition between the free space and constrained motion controls. This transition should allow the robot end-effector to stay on the contact surface when no input force is applied. Moreover, this should not create a *sticking effect* when a rapid pull back from a contact surface is attempted. Hence, the transition control law consists simply in varying the effective damping and inertia parameters. This control law is applied when the external contact force between the robot and the environment, f_e, is comprised between two selected limits noted f_{emin} and f_{emax}. The virtual damping is adjusted according to

$$c_{ov} = c_o - \alpha_{amp}(f_e - f_{emax}) \tag{1.17}$$

where α_{amp} is defined as

$$\alpha_{amp} = \frac{c_o - c_{oamp}}{f_{emax} - f_{emin}} \tag{1.18}$$

in which c_{oamp} is the operator virtual damping for the constrained situation. The virtual inertia is adjusted using

$$m_{ov} = \frac{m_o c_{ov}}{c_o} e^{\gamma_{amp}(c_{ov} - c_o)} \tag{1.19}$$

where γ_{amp} is the smoothness parameter used to adjust the exponential transition. An example is shown in Fig. 1.3 with $f_{emin} = 0.1N$, $f_{emax} = 0.9N$, and $\gamma_{amp} = 3.1$. The virtual damping changes from 8 to $6.5Ns/m$, and the virtual inertia changes from 1 to $0.007kg$.

The dynamics of the force amplification situation can be viewed as two mass-damping systems pushing against one another. When no input force is applied by the operator, the whole system tends to return to its equilibrium, i.e., a zero environment force. If one of the two inertias is

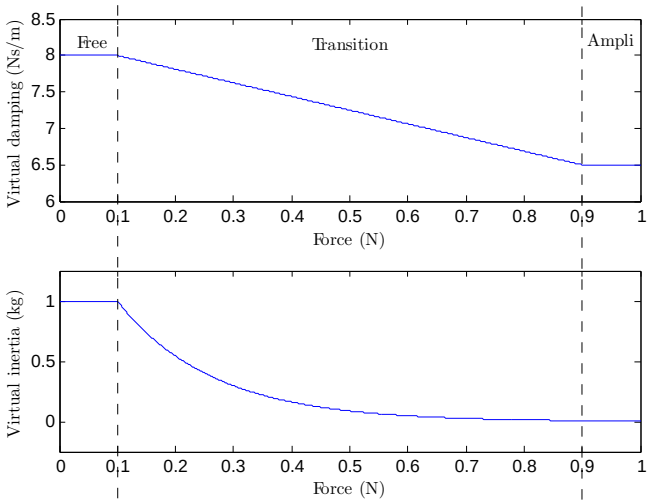

FIGURE 1.3 – Example of the effect of the transition law on the virtual damping and virtual inertia. The force on the x-axis is the contact force measured between the robot and the environment. The admittance parameters transit smoothly from the free space motion mode to the force amplification constrained mode.

larger, or if one of the two damping coefficients is smaller, then the system tends to overshoot on the other side. This explains the need for a smooth increase of the operator admittance parameters when the system approaches the critical zone of zero environment force. It is also understood that if an environment force is sensed, the transition law prevails over the continuous control law, but that if a fast pull back is attempted, the transition law is bypassed because of its small effective range of operation.

1.3.3 Amplification factors

As shown above, in a constrained situation in which Y_o and Y_e have the same admittance parameters as well as small inertias, the force amplification β is solely dependent on β_o and β_e. In this case, one should use both factors to generate the amplification, rather than only one. Indeed, each factor has a significant impact on the system response. Moreover, they represent different specifications due to their location in the force control loop. The first important feature is the change in the feedback steady state gain, given by the variation of β_e, that has a direct incidence on the stability of the system. An increase of this gain positively affects its performance but may also compromise its stability if too high. The second feature is the change in the command steady state gain, given by the variation of β_o, that controls directly the magnitude of the velocity command. Therefore, this parameter complements the first one in order to obtain the desired force amplification β. A variation of β_o has practically no impact on the stability of the system when β_e is chosen appropriately and remains constant. The effect of these factors on the control loop will be demonstrated in the upcoming sections.

1.4 Oscillation canceller

The effect of the different control parameters was established in the preceding section, which led to the development of a stable and fast amplification controller by proper adjustment of the force control loop. However, one issue remains to be addressed in order to make the controller fully reliable, namely the possible occurrence of oscillations for high frequency inputs when admittance parameters are low. A straightforward approach to resolve this issue would be to slightly increase the admittance parameters. Unfortunately, such an approach would slow down the response. Instead, it is proposed here to keep both admittance parameters as low as possible without instability and to actively modify the amplification factors. An appropriate discontinuous variation of the admittance steady state gains through β_o and β_e allows the system to be fast and precise for low to medium frequency inputs, and to cancel oscillations for high frequency inputs. The following algorithm is introduced in order to implement this approach.

$$\begin{aligned}
&\text{If} \quad (i) \quad f_e > f_{sw} \text{ and } \dot{f}_o > \dot{f}_{osw} \\
&\qquad\qquad \text{or} \\
&\qquad (ii) \qquad \dot{f}_e > \dot{f}_{esw} && (1.20)\\
&\text{then} \qquad \beta_e = \beta_c && (1.21)\\
&\qquad\qquad \beta_o = \beta\beta_e && (1.22)\\
&\text{for} \qquad t_i < t \leq t_i + t_c && (1.23)
\end{aligned}$$

where f_e, $\dot{f}_e$, and $\dot{f}_o$ are respectively the contact force between the robot and the environment, its time derivative, and the time derivative of the force applied by the operator on the input sensor. Also, f_{sw} is the minimum force between the robot and the environment representing a physical contact with an object (contact threshold of the sensor), $\dot{f}_{osw}$ and $\dot{f}_{esw}$ are the maximum time derivatives of the forces for which the system remains stable and has no oscillation and β_c is the minimum environment amplification that leads to a stable response for any input frequency. Finally, t_i is the current time and t_c is the minimum time required to cancel the initiation of an oscillation. Condition (i) limits the output response when the time derivative of the input command exceeds a certain maximum value. It allows the system to remain stable for high frequency command when it is in a constrained situation. Condition (ii) limits the output response when the time derivative of the output exceeds a certain maximum value. It is especially useful for a fast impact situation with a rigid object where f_o is already high and $\dot{f}_o$ does not necessarily vary so much. Equation (1.22) preserves the general amplification relationship.

In other words, the Oscillation Canceller (OC) proposed above allows the process to respond slowly when the time derivative of the force input becomes too large, so as to remain passive with respect to the environment. The force control bandwidth is therefore temporarily

augmented. Furthermore, the OC can be seen as a safe switch that counters fast impulse perturbations or inputs.

1.5 Experimentation

1.5.1 Experimental setup

The novel admittance controller proposed above was validated experimentally using a simple one-dof robot. The experimental setup is shown in Fig. 1.4. It consists of a single revolute joint, a 130mm arm, two single-axis force sensors, and an actuator. One of the force sensors receives the operator input while the other one measures the force generated by the actuator and the operator on the environment. The operator sensor is limited to 5kg and the environment sensor is limited to 20kg. Both sensors are Phidgets Micro Load Cells. The actuator is a Pittman DC Servo Gearmotor with a gearbox ratio of 65.5 :1 and an encoder of 500CPR. The maximum theoretical force that can be generated by the actuator at the end-effector is 26N. The control algorithm is developed with Simulink and RT-LAB. It is then implemented on a real-time QNX computer with a sampling period of 2ms.

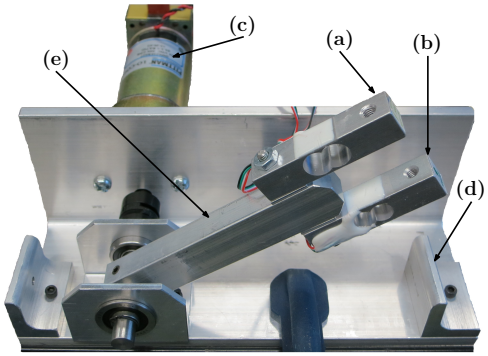

FIGURE 1.4 – One-dof experimental test bench. Components : (a)operator force sensor, (b)environment force sensor, (c)motor, (d)stiff environment, and (e)robot link

Since the effectiveness of the free space motion control law was demonstrated in (Lecours et al. [2012]), the experimental section of this chapter focuses on the constrained situation and the mode transition. Three important properties should be verified in a human-robot force amplification context in order to ensure a natural cooperation, namely : (*i*) the amplification itself, which should be reached at steady-state, (*ii*) the tracking performance so as to achieve the most natural interaction, and (*iii*) the occurrence of vibrations that should be cancelled for efficiency and safety reasons. The performance of the controller proposed in this chapter is demonstrated with the experiments described in the following subsections.

1.5.2 Force amplification for low and high admittances, and high virtual inertia

The first experiment consists in the pursuit of an approximately sinusoidal signal manually generated by an operator with an amplitude of 7.5N, a mean value of 12.5N, and a frequency of approximately 0.4Hz. Three tests were conducted with different sets of parameters in order to assess the tracking performance. The results for a duration of 7.2 seconds are shown in Fig. 1.5. Figure 1.5(a) shows the response with low admittance parameters ($m = 0.007kg$ and $c = 6.5Ns/m$) and an amplification of 4 times the operator input ($\beta_o = 1.6$ and $\beta_e = 0.4$). These admittance parameters are the default ones for a regular operation, and Y_o and Y_e are always similar in constrained mode. Figure 1.5(b) represents a high admittance situation with the same virtual inertia to virtual damping ratio used for the low admittance experiment. As an alternative to directly changing the admittance parameters the amplification factors are reduced while keeping $\beta = 4$ ($\beta_o = 0.8$ and $\beta_e = 0.2$). Reducing the admittance steady-state gains leads to a phase shift of the response. Figure 1.5(c) shows the response obtained with larger virtual inertia values ($m = 0.7kg$ and $c = 6.5Ns/m$) and the default amplification factors. In fact, when the virtual inertia to virtual damping ratio is larger, the response is slower and more overshoots arise.

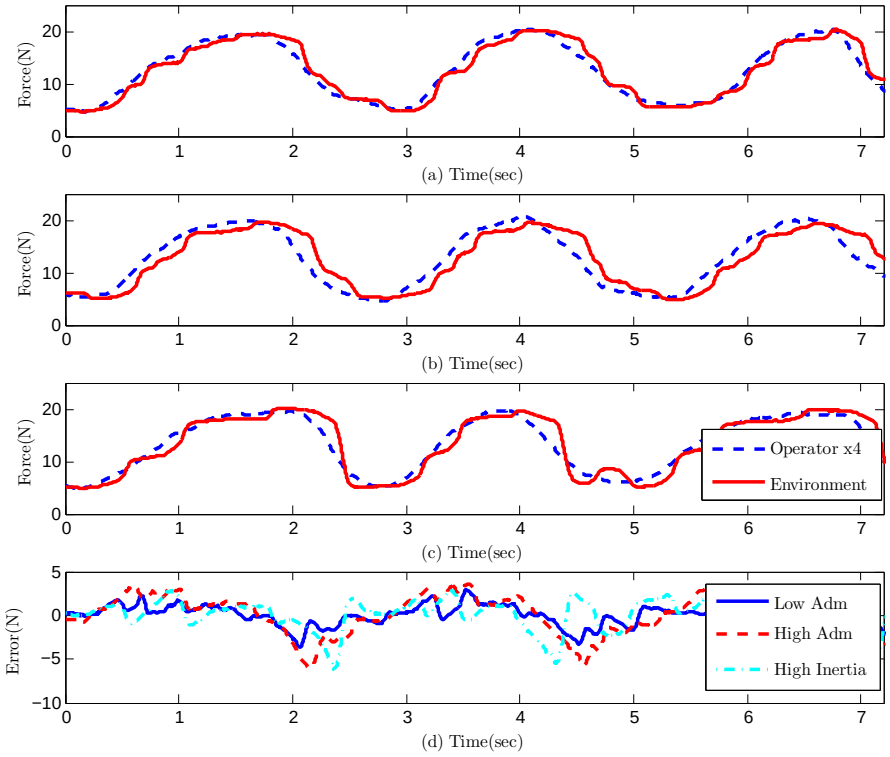

FIGURE 1.5 – (a)Low admittance pursuit, (b)high admittance pursuit, and (c)high virtual inertia pursuit. (d)Error for low and high admittances, and high virtual inertia in the pursuit experiments. The operator force is amplified 4 times on the graphs for comparison purposes.

Figure 1.5(d) shows the error between the operator input and the environment output for each case. The low admittance case seems to give better results than the other two. This is confirmed by the residual sum of squares (RSS), given in Table 1.1, for the 7.2 seconds time period of evaluation. In the experiment reported here, the high virtual inertia performs relatively well, but with the combination of human interaction and overshoots it can become unpredictable, and hence damaging for the response.

TABLE 1.1 – Residual Sum of Squares ($\times 10^4 N^2$)

Low admittance	High admittance	High virtual inertia
0.609	2.038	1.135

1.5.3 Continuous interaction - unconstrained to constrained environment

The second experiment demonstrates how the system behaves for a continuous interaction between the free and the constrained spaces. The interaction consists of a displacement induced by the operator force input, followed by a contact with a stiff environment where the amplification is initiated, then followed by a fast pull back to finally return to a displacement in free space. Figure 1.6 depicts this particular situation with the default admittance parameters. The input (reference) and the response (encoder) velocities of the inner position control loop are shown in Fig. 1.6(a). Velocity plots are shown instead of position plots because they are thought to be more relevant when a physical human interaction feedback is involved. Moreover, the operator force input and the environment force response are represented in Fig. 1.6(b). As expected, it can be observed that an accurate tracking of the reference velocity (resulting of the operator force input) and a zero environment force are obtained in the free space motion mode. On the contrary, and also as expected, an accurate tracking between the operator and the environment forces, and a zero encoder velocity are observed in the constrained mode. In the latter mode, the reference velocity becomes the error between the two amplified admittance outputs, as seen in Fig. 1.1. This error will then reach zero for a steady-state. An interesting behaviour of the controller is shown during the fast pull back (at the end of the force amplification stage). In fact, even if there is no *sticking effect*, as it is observable for the second transition of Fig. 1.6(b), there is a slight phase shift of the encoder velocity due to the high value of the reference velocity when the robot initiates its motion. For a reference velocity below the saturation limits of $\pm 3 rad/s$ the operator should not feel any constraint or inconvenience. The impact of the gearbox backlash is also noticeable on the velocity response when changing directions.

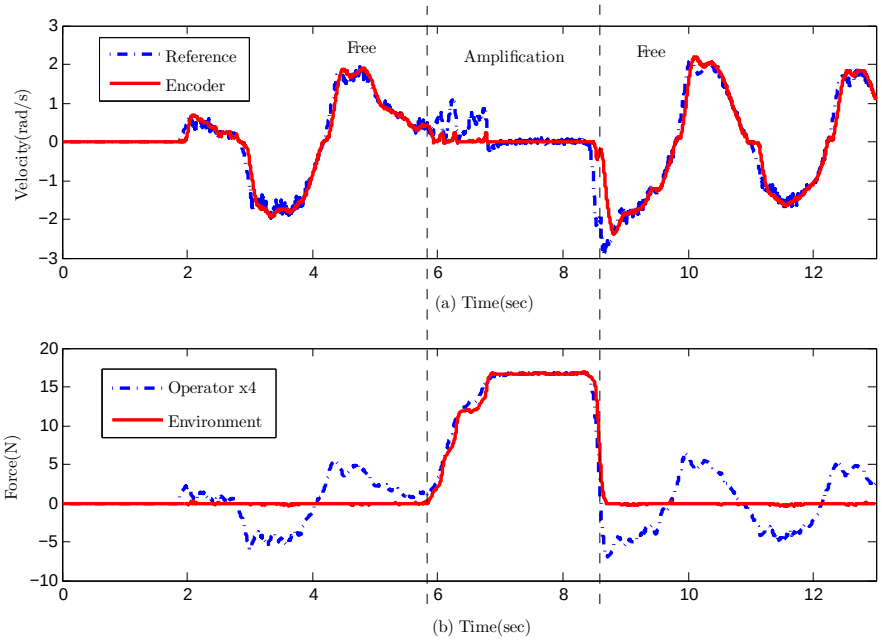

FIGURE 1.6 – Continuous interaction between the free and constrained spaces. (a)Reference and encoder velocities of the robot link, and (b)force sensors signals. The operator force is amplified 4 times for comparison purposes.

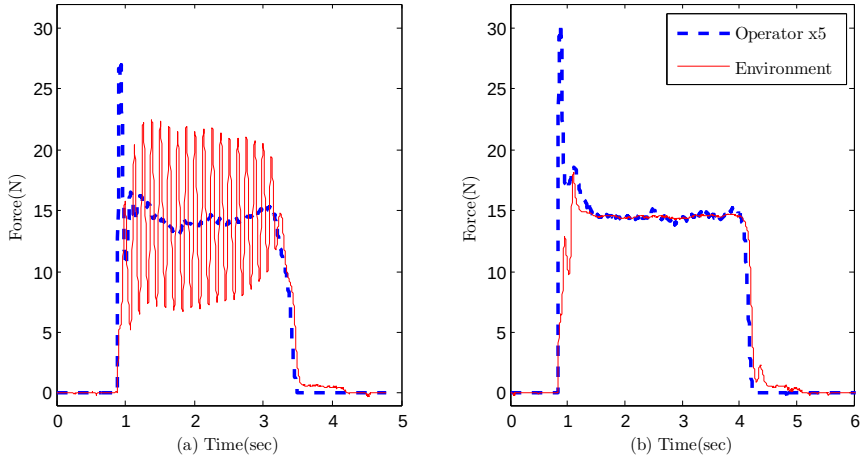

FIGURE 1.7 – Impulse response (a)without the oscillation canceller and (b) with the oscillation canceller. The operator force is amplified 5 times for comparison purposes.

1.5.4 Impulse response - unconstrained to constrained environment

The third experiment reported here is a fast impulse from the unconstrained ($f_e = 0$) to the constrained environment, followed by a constant force input of 3N. In this case, the amplification is 5 times the operator input ($\beta_o = 2$ and $\beta_e = 0.4$). Fig. 1.7 shows two tests, one without the oscillation canceller (a), and one with the oscillation canceller (b). The OC parameters are set to $\beta_c = 0.08$, $t_c = 0.16sec$, $f_{sw} = 0.4N$, $\dot{f}_{osw} = 45Ns/m$ and $\dot{f}_{esw} = 120Ns/m$. With the

OC, all major vibrations or fast impulses are eliminated and the system is therefore able to follow the amplified input. The impact of the transition law is also noticeable in Fig. 1.7. Indeed, when the operator force is released, there is a smooth return to zero of the environment force below $f_{emax} = 0.9N$. As a result, the robot end-effector stays on the contact surface without applying any force.

1.5.5 Video demonstration

The accompanying video demonstrates all situations to be addressed by the controller, namely, free space motion, constrained force amplification and transition between the two (*Chap1_ Force_ Amp_ 1dof.mp4*). The video also illustrates the stability and effectiveness of the controller for fast pull back and sharp contacts (impulses) with a stiff environment. It can be observed that the controller is always stable and that it leads to a very intuitive behaviour. The amplification of the force is also illustrated visually using two identical deformable objects. The video is available at

http://robot.gmc.ulaval.ca/publications/these-de-doctorat

1.6 Conclusion

A novel force amplification controller for pHRI was presented in this chapter. The controller uses the principle of variable admittance in order to optimize the free space and constrained motions. The effect of the different parameters in the force control loop was assessed and explained. Moreover, the experimental results demonstrate that the new approach leads to an intuitive and effective force amplification control, with the help of a smooth transition law and the oscillation canceller. Current work includes the application of the controller to a multi-dof robot.

Chapitre 2

Performance Optimization of a Multi-DoF Bilateral Robot Force Amplification

Résumé

Cet article présente une nouvelle approche afin de déterminer la commande optimale pour un manipulateur robotisé à plusieurs degrés de liberté (multi-ddl) dans un contexte d'amplification de force et d'interaction bilatérale. Le problème principal lors de l'utilisation d'un manipulateur multi-ddls est le lien direct entre sa configuration et sa dynamique. Cette variation de la dynamique du robot est donc prise en compte lors du processus d'optimisation. Ceci permet d'obtenir un contrôleur stable et des performances exceptionnellement élevées. De plus, la stabilité couplée du manipulateur est évaluée en utilisant une version étendue de la stabilité complémentaire qui permet d'éviter les conditions de passivité. Même si l'optimisation proposée ici est basée sur trois indices de performance spécifiques aux amplifications bilatérales, elle peut être aisément adaptée à n'importe quel type d'interactions bilatérales. La stabilité et la performance résultante de la commande optimale sont démontrées pour un manipulateur sériel à sept degrés de liberté avec des tests d'impact sur différentes surfaces de contact.

2.1 Introduction

In recent decades, bilateral robot interaction has been widely covered in the literature. The emergence of teleoperation in the medical field for assistance in treatment or surgery has greatly contributed to this research effort. Indeed, safety and performance are more than crucial for medical applications. Unfortunately, the control strategy used in most robotic systems is often designed for a single degree of freedom (dof) which is far from the current reality in teleoperation where the interaction usually occurs at the end-effector of a multi-dof manipulator. Moreover, during the design phase, the performance is limited by the constraints

on the prevalent stability analysis, which therefore ends up being evaluated solely online, resulting in suboptimal controllers.

This common coupled stability analysis is known as Llewellyn's absolute stability criterion (Llewellyn [1952]) and involves the notion of passivity (Wyatt et al. [1981]). It has been proven that a passive controlled manipulator interacting with passive environments results in a stable interaction (Colgate [1994], Lawrence [1993]). This notion is convenient due to its simplicity but it is rather conservative. Through the years, different methods to relax this conservative condition have emerged. For instance, Hashtrudi-Zaad and Salcudean [2001] and Lamy et al. [2010] proposed to limit the impedance of the operator or the environment to a maximum value which may then be absorbed in the port network for a more accurate stability analysis. Another interesting approach, presented in Haddadi and Hashtrudi-Zaad [2010], makes use of the scattering parameters and wave variables to transform the system impedances into reflection coefficients, and then studies the coupled stability boundaries in the scattering domain. However, the resulting graphical representation provides a visual aid rather than a design tool. Similarly, Jazayeri and Tavakoli [2012] proposed to use the Möbius transformation on Llewellyn's conditions in order to visualize and interpret the boundaries on the interacting impedances allowing at the same time non-passive environment or operator.

To avoid the passivity conditions, robust stability theory has been explored. Early studies were presented in Yan and Salcudean [1996] using the infinity-norm $\mathcal{H}_\infty$ approach, and in Colgate [1993] using the structured singular value analysis for bilateral systems. Recently, the parameter-space approach with environment uncertainties has been proposed in Peer and Buss [2008]. However, the structured singular value analysis remains the state of the art in robust stability analysis. It has been used with modern tools by Buerger for unilateral interactions in Buerger and Hogan [2007] where it has been renamed complementary stability. All the above contributions have been developed for single-dof models. However, Llewellyn's criterion has been extended to multi-dof and multi-lateral systems in Li et al. [2014].

It is important to mention that typical compensator structures for unilateral interactions are often simple and still achieve great performances. It would therefore be interesting to study the possibility to keep these same structures as well for amplification interactions and be able to reach this high level of performance.

In this chapter, complementary stability is extended to a multi-dof bilateral system. An algorithm that computes the optimal parameter values for pre-defined controller structures for all possible manipulator configurations is presented. Section 2.2 presents an overview of the optimization process. Section 2.3 recalls the notion of port-interaction. Then, robust stability analysis for a multi-dof bilateral device is presented in Section 2.4, followed, in Section 2.5, by the details on the three performance indices selected for the optimization algorithm as well as a controller comparison. Section 2.6 then introduces the manipulator configuration-related

variable that allows to obtain the optimal control law, and discusses some impact test results that assess the performance of the optimization. Finally, a conclusion is drawn in the last section.

2.2 Optimization Process Overview

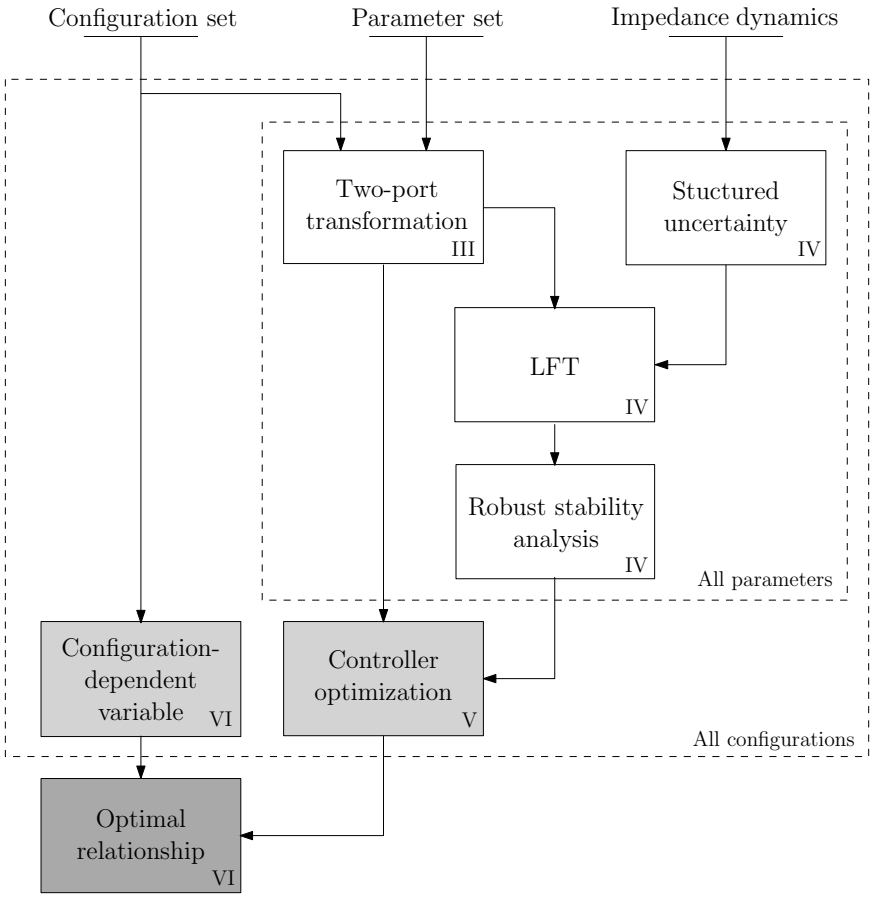

FIGURE 2.1 – General framework of the controller optimization process. The section number associated with each step of this process in the chapter is also given.

The optimization algorithm presented in this chapter includes various notions derived from control theory and from the mechanics of robotic manipulators. It is thus necessary to first introduce the general framework of the algorithm in order to clearly understand the purpose of each step of the optimization process. These steps are shown in Fig 2.1. In short, it is desired to find the optimal parameters for a pre-defined controller structure, a specific robot architecture, and known external interaction inputs. However, the dynamics of a robotic manipulator is usually configuration dependent. It is therefore necessary to determine the optimal control parameters of the *Parameter set* for each configuration from the *Configuration set* in order to keep this optimality at all times. The first step is to rearrange the system

into a two-port interaction in order to isolate the two external input dynamics, namely, the human and environment impedances. These two dynamics, *Impedance dynamics*, have a range of uncertainty and can thus be defined as a *Structured uncertainty* in order to easily recast the system into a linear fractional transformation (LFT). This transformation is convenient to assess the robust stability of the system (*Robust stability analysis*). Then, knowing which parameter values are stable and unstable, the optimization can be performed following certain criteria (*Controller optimization*) which use the dynamics of the controlled manipulator without the dynamics of the external inputs. Finally, each configuration is converted to a unique variable (*Configuration-dependent variable*) that is directly dependent on the manipulator's configuration and that is associated to the optimal control parameters previously found in order to establish the *Optimal relationship*.

2.3 Multi-DoF Two-Port Interaction

The notion of port network has proven through the years to be the most suitable way to analyse systems interactions. It is indeed widely used in motion-force interaction, especially when human beings are in the loop. This notion is briefly recalled here for a two-port interaction, as depicted in Fig. 2.2. Typically, the systems interacting with one another, and their dynamics, are connected through port variables, usually represented by force and velocity. This allows the multiple dynamics to be expressed in terms of mechanical impedances linking them together with the interaction variables. In the case of a bilateral robot interaction, the human and environment impedance matrices are thus described as follows

$$F_o = \mathbf{Z}_o V_o, \tag{2.1}$$

$$F_e = \mathbf{Z}_e V_e \tag{2.2}$$

where $\mathbf{Z}_o$, F_o, V_o, and $\mathbf{Z}_e$, F_e, and V_e are respectively, the human and environment impedance matrices, force vectors and velocity vectors. The rest of the systems is included in the two-port dynamics that usually contains the robot (or the two robots in the case of teleoperation), the communication channels, and the control loops (see Appendix 2.9.1 for details). The link between the forces and velocities is given here by a matrix of admittances and yields

$$\begin{bmatrix} V_o \\ V_e \end{bmatrix} = \begin{bmatrix} \mathbf{Y}_{oo} & \mathbf{Y}_{oe} \\ \mathbf{Y}_{eo} & \mathbf{Y}_{ee} \end{bmatrix} \begin{bmatrix} F_o \\ -F_e \end{bmatrix} = \mathbf{Y} \begin{bmatrix} F_o \\ -F_e \end{bmatrix} \tag{2.3}$$

where $\mathbf{Y}$ is a two-port matrix whose components relate the operator or environment velocities to both the operator and environment forces. The performance optimization presented in this chapter may be applied to any bilateral system. However, the analysis has been developed for a single seven-dof manipulator on which both external forces, namely the operator and the environment interactions, are directly exerted on the structure. The non-collocation of the sensors implies that different velocities must be considered for each external impedance,

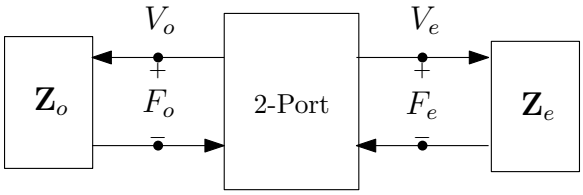

FIGURE 2.2 – Generalized two-port interaction.

which are however related to the same robot joint velocities output with different Jacobian matrices. The redundant nature of the seven-dof manipulator also introduces the need to have a proper redundancy resolution scheme to develop the analysis in the Cartesian space. Here, the Moore-Penrose pseudoinverse of the Jacobian has been used to resolve the redundancy at the centre of the spherical joint (intersection of the last three joint axes). This point is chosen in order to decouple the rotations between the end-effector and the human interaction handle on the fourth link (see Fig. 2.6). A simplified schematic of the system is shown in Fig. 2.3 where $\mathbf{R}$ refers to the redundancy resolution scheme which includes an integrator. $\mathbf{G}_o$ and $\mathbf{G}_e$ are, respectively, the operator and environment regulators while $\mathbf{J}_o$ and $\mathbf{J}_e$ are, respectively, the Jacobian matrices relating the robot joint velocities to the operator and environment velocities. This simplified architecture allows one to easily compute the two-port interaction matrix and then to use the many tools available for stability analysis (details in Appendix 2.9.1).

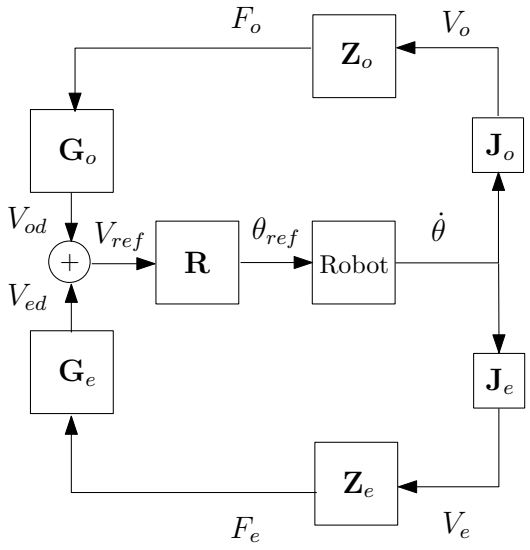

FIGURE 2.3 – Simplified block diagram of the bilateral interaction.

2.4 Stability Analysis

As previously mentioned, many issues still remain open with commonly used stability analyses for bilateral interaction, the most important being the conservative nature of these techniques that unnecessarily restrains performance. Indeed, coupled stability is often validated using the concept of passivity, which has already been extensively covered (Colgate [1994]). Although some techniques can be used to relax the passivity condition using the knowledge of certain components of the interacting dynamics (Hashtrudi-Zaad and Salcudean [2001], Lamy et al. [2010], Haddadi and Hashtrudi-Zaad [2010]), the notion of passivity still limits the manipulator design to a specific set of controllers.

2.4.1 Complementary Stability

The complementary stability proposed in Buerger and Hogan [2007] makes use of the robust analysis tools in order to overcome the requirements for passivity. More specifically, it involves a particular case of the small-gain theorem called structured singular value (Packard and Doyle [1993]) that has further matured into μ-analysis theory. Actually, μ-analysis may be seen as conservative from the point of view of servo design that generally implies well-known dynamics. However, for an interaction system where the operator and environment may be represented by a wide range of different dynamics, this stability analysis is more than relevant. Indeed, the human and environment impedances may be defined as uncertain while keeping them bounded for a known range of application. The analysis thus ensures the coupled stability of the system for specific dynamics (see Appendix 2.9.2 for solutions to robust stability computational issues).

Therefore, this promising technique, previously developed for a unilateral interaction, is extended here to a bilateral interaction. It is important to note that the multi-dof architecture of the manipulator is considered in the computation of each component of the two-port mapping function, $\mathbf{Y}$, using the Jacobian transformation. This two-port mapping function $\mathbf{Y}$ is therefore defined in the Cartesian space as a $[12 \times 12]$ matrix. However, for the robust stability analysis and for the performance optimization described in Section 2.5, only the Cartesian translations are studied and each of these components is evaluated individually. At this stage, the assumption that all Cartesian translational components are *pseudo*-decoupled is possible mainly because the study is on the control of Cartesian amplification, and that, for this reason no major Cartesian motion coupling arises. It also permits to reduce the μ-analysis computation time as well as to optimize the performance related to the different robot configurations as further demonstrated in Section 2.6. Thereby, the two-port mapping function becomes a $[2 \times 2]$ matrix and is denoted $\mathbf{Y}_x$ in the unstructured closed-loop perturbed system represented in Fig. 2.4. The uncertain human and environment dynamics may be defined with additive uncertainties as follows

$$\mathbf{Z}_o(s) = \mathbf{Z}_{on}(s) + \mathbf{W}_o(s)\mathbf{\Delta}_o(s), \tag{2.4}$$

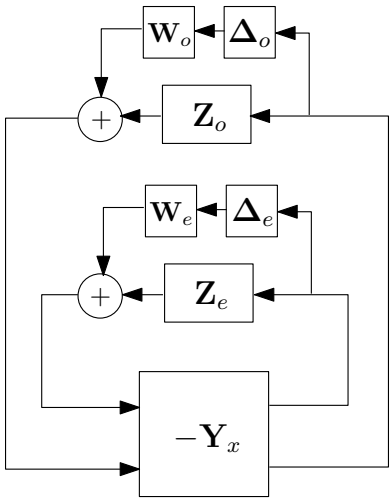

FIGURE 2.4 – Interconnection of one of the robot's Cartesian dof with the operator and environment impedances including additive uncertainties.

$$\mathbf{Z}_e(s) = \mathbf{Z}_{en}(s) + \mathbf{W}_e(s)\mathbf{\Delta}_e(s) \tag{2.5}$$

where $\mathbf{Z}_{on}(s)$ and $\mathbf{Z}_{en}(s)$ are the nominal impedances dynamics, $\mathbf{W}_o(s)$ and $\mathbf{W}_e(s)$ are stable rational weighting functions that define the uncertainty bounds on the operator and environment impedances, $\mathbf{\Delta}_o(s)$ and $\mathbf{\Delta}_e(s)$ are the normalized perturbations, and s is the Laplace variable. The feedback system of Fig. 2.4 is then recast into the convenient linear fractional transformation (LFT) framework with structured uncertainty presented on the left-hand side of Fig. 2.5. Any kind of uncertainty can be represented in this interconnection form and would always generate the same robust stability conditions. Considering the operator and environ-

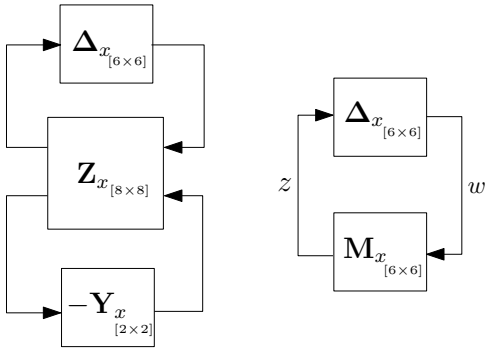

FIGURE 2.5 – LFT form of a single cartesian-dof with the structured uncertainty and its equivalent standard feedback interconnection $\mathbf{M}_x - \mathbf{\Delta}_x$.

ment mechanical impedances as two second-order models, the general impedance form can be described as

$$Z(s) = ms^2 + cs + k \tag{2.6}$$

where m, c, and k are, respectively, the equivalent inertia, damping, and stiffness of the external interactions. To evaluate the coupled stability of the desired dynamics range, uncertainties are added to each impedance parameter, which yields

$$\begin{aligned} m_o &= m_{on} + m_{od}\Delta_{m_o}, \\ c_o &= c_{on} + c_{od}\Delta_{c_o}, \\ k_o &= k_{on} + k_{od}\Delta_{k_o}, \end{aligned} \tag{2.7}$$

$$\begin{aligned} m_e &= m_{en} + m_{ed}\Delta_{m_e}, \\ c_e &= c_{en} + c_{ed}\Delta_{c_e}, \\ k_e &= k_{en} + k_{ed}\Delta_{k_e} \end{aligned} \tag{2.8}$$

where the index n refers to the nominal value of each particular parameter, and the index d refers to the maximum scalar deviation from that value. As previously stated, each Δ represents the normalized uncertainty of each impedance parameter. These six normalized uncertainties may be rewritten as the structured perturbation $\mathbf{\Delta}_x$ of Fig. 2.5, such that

$$\mathbf{\Delta}_x = diag\{\Delta_{m_o}, \Delta_{c_o}, \Delta_{k_o}, \Delta_{m_e}, \Delta_{c_e}, \Delta_{k_e}\} \tag{2.9}$$

and where the uncertainty block structure is defined as follows

$$\mathbf{\Gamma} := \{\mathbf{\Delta}_x : \Delta_i \in \mathbb{R}\} \ , \ i = \{m_o, c_o, k_o, m_e, c_e, k_e\}. \tag{2.10}$$

With this formulation, it is now easy to define the necessary and sufficient condition for robust stability, which is that the inverse of the structured singular value upper bound of the lower LFT, $\mathcal{F}_L[\mathbf{Z}_x, \mathbf{Y}_x]$, noted $\mathbf{M}_x$, is larger than or equal to 1, i.e,

$$[\sup_{\omega\in\mathbb{R}} \mu_{\mathbf{\Gamma}}(\mathbf{M}_x)]^{-1} = [\sup_{\omega\in\mathbb{R}} \mu_{\mathbf{\Gamma}}\{\mathcal{F}_L[\mathbf{Z}_x, \mathbf{Y}_x]\}]^{-1} \ \geq \ 1, \tag{2.11}$$

under the assumption that

$$\|\mathbf{\Delta}_x\|_\infty < 1. \tag{2.12}$$

The definition of complementary stability follows directly from the robust stability condition which in this thesis makes use of the structured singular value, more precisely the mixed-μ theorem. The definition thus states that a robot interacting with any port impedances Z_o and Z_e within the dynamics sets defined by (2.4) and (2.5) is complementary stable for $\|\mathbf{\Delta}_x\|_\infty \ < \ 1$ *iff* $\sup_{\omega\in\mathbb{R}} \mu_{\mathbf{\Gamma}}(\mathbf{M}_x) \ \leq \ 1$.

This analysis leads to a wider range of controllers, including passive and nonpassive ones, and allows to further improve the performance of bilateral systems.

2.5 Optimization Criteria

Now that the bilateral stability condition is established, a performance index is needed. In Buerger and Hogan [2007], a cost function that corresponds to the difference between the robot impedance and a desired impedance is proposed. This choice is adequate for a unilateral interaction, but for a bilateral interaction where two impedances are present, this performance index is ineffective. It is therefore interesting to consider different options.

2.5.1 Performance Indices

For bilateral systems, the first performance criterion to consider is undoubtedly the transparency (Lawrence [1993]). This criterion evaluates the correspondence between the environment impedance and the impedance transmitted to the operator, such that a perfect transparency would result into

$$Z_t = Z_e \tag{2.13}$$

where the transmitted impedance Z_t is defined as $F_o = Z_t V_o$. It is important to recall here that the optimization is performed on each Cartesian motion individually, such that each variable in this section and the next one represents a single component and is taken from the matrix diagonal. Using (2.2) and (2.3), one may find the relationship with the manipulator port admittances that follows

$$Z_t = \frac{F_o}{V_o} = \frac{1}{Y_{oo} + \frac{Y_{oe}Y_{eo}}{\frac{1}{Z_e}+Y_{ee}}}. \tag{2.14}$$

Also, if a steady-state is assumed, such that $V_o = V_e$, the amplification factor, β, can be obtained with the port function (2.3) as follows

$$\frac{F_e}{F_o} = \frac{Y_{oo} - Y_{eo}}{Y_{oe} - Y_{ee}} = \beta. \tag{2.15}$$

Therefore, using equations (2.14) and (2.15) it is possible to find the conditions that lead to equation (2.13), i.e., perfect transparency, which yields

$$Y_{oo} = \beta Y_{oe}, \tag{2.16}$$

$$Y_{eo} = \beta Y_{ee}, \tag{2.17}$$

$$\frac{1}{Y_{oo}} = \frac{1}{Y_{ee}} = 0. \tag{2.18}$$

These conditions also lead to a first optimization criterion related to the amplification capability of the system in steady-state, also known as kinematic correspondence (Hashtrudi-Zaad and Salcudean [2002], Chang and Kim [2012]). Equation (2.15) may be numerically unstable knowing that a transparent system would require that $Y_{ee} = Y_{oe}$. It is thus preferable to use equation (2.16) or (2.17) to assess the amplification performance. This assumption provides a very close estimate of equation (2.15) along with more stable computations.

The measure of the amplification turns out to be a relevant criterion for the optimization process, but it still excludes the environment impedance. A transparency index is therefore necessary to evaluate the transmission capability. The Z-width principle proposed in Colgate and Brown [1994] provides a certain estimation of the dynamic range of the transmitted impedance and bears the following equations :

$$Z_{tmin} = Z_t|_{Z_e=0} = \frac{1}{Y_{oo}}, \tag{2.19}$$

$$Z_{tmax} = Z_t|_{Z_e\to\infty} = \frac{1}{Y_{oo} - \frac{Y_{oe}Y_{eo}}{Y_{ee}}}, \tag{2.20}$$

$$Z_{twidth} = Z_{tmin} - Z_{tmax}. \tag{2.21}$$

A perfectly transparent system would obviously lead to $|Z_{twidth}| \to \infty$. The Z-width holding the two extreme cases of impedance, namely free motion and clamped interactions, respectively depicted by equations (2.19) and (2.20), attempts to include the whole impedance spectrum. However, depending on the situation, including both extreme conditions might not be necessary. Here, the interaction of interest implies a contact with a high impedance environment. Equation (2.20) should thus be sufficient to assess the transparency performance and is thereby proposed as a second optimization criterion.

Although the above two criteria cover major performance aspects of bilateral interactions, a third criterion focusing more on the transient response would greatly improve the optimization process. Therefore, the integral of the time-weighted absolute error (ITAE), commonly used in servo design (Martins [2005]), is also included. This performance index evaluates the system response to a unit step input and is defined as

$$ITAE = \int_0^\infty t|\epsilon|dt \tag{2.22}$$

where t is the time variable and ϵ is the error between the output and the set point. In other words, this index provides a cost related to the settling time and the overshoot of a transient response. The ITAE cost is thus computed on the manipulator admittance Y_{eo} which relates the operator input force and the output environment velocity. However, it could also be used on any manipulator function and would still hold the same comparative meaning.

To summarize, all three optimization criteria are presented here with their related cost :

1. Amplifcation index, noted C_β

$$C_\beta = \frac{\sum_{i=1}^{n} |\beta - \frac{|Y_{eo}(j\omega_i),|}{|Y_{ee}(j\omega_i)|}|}{n}, \tag{2.23}$$

2. Transparency index, noted C_T

$$C_T = \frac{\sum_{i=1}^{n} ||Y_{oo}(j\omega_i)| - \frac{|Y_{oe}(j\omega_i)||Y_{eo}(j\omega_i)|}{|Y_{ee}(j\omega_i)|}|}{n}, \tag{2.24}$$

3. ITAE index, noted C_I

$$C_I = \int_0^\tau t|\epsilon|dt \tag{2.25}$$

where n is the total number of frequencies, ω_i, evaluated in the desired frequency range, τ is the upper bound on the desired time range, and j is the imaginary unit ($j = \sqrt{-1}$). Here, τ is equal to 1 second in order to ensures that the steady state can be reached, and the frequency range $\omega_i \in [10^{-2}, 10^2]$ rad/s (or [0.0016, 16] Hz) is used in order to include the typical human interaction frequencies. Indeed, a human physical input has a typical responsiveness of about 5 Hz, and can reach in some cases a maximum responsiveness around $10 - 12$ Hz, as demonstrated in Brooks [1990] and Jones [2000]. A frequency range upper bound three times the typical human responsiveness is thus considered as sufficient for the optimization.

2.5.2 Controller Comparison

The next step to evaluate the optimal parameter values for typical unilateral controller structures is to devise an optimization strategy involving the aforementioned performance indices and thereby, achieving an optimal controller. Different controllers and different parameter sets should be tested in order to obtain a more complete cluster of potential outcomes. A simple way to optimize the set of parameters of a pre-defined controller structure is to minimize the sum of the normalized performance costs that are complementary stable, i.e.,

$$C = \mathbf{w}^T \, [\, \bar{C}_\beta, \bar{C}_T, \bar{C}_I \,]^T \tag{2.26}$$

where C is the global cost associated with a given set of parameters and $\mathbf{w}^T = [w_\beta, w_T, w_I]$ is the weighting vector used to reflect the priority level of each normalized cost $\bar{C}_\beta$, $\bar{C}_T$, and $\bar{C}_I$. The unity-based normalization is calculated over all the sets of parameters evaluated, with the minimum and maximum costs of each index computed as follows

$$C_{xmin} = min|\mathbf{C}_x| \tag{2.27}$$

$$C_{xmax} = max|\mathbf{C}_x| \tag{2.28}$$

where $\mathbf{C}_x$ represents a matrix including all computed costs for each performance index with the index x referring to the different indices, namely $x \in \{\beta, T, I\}$.

An example is provided for an admittance control, also known as lowpass control, and is defined by the following general transfer function :

$$G_{adm} = \frac{\beta_x}{m_v s + c_v} = \frac{\frac{\beta_x}{c_v}}{\frac{m_v}{c_v} s + 1} \tag{2.29}$$

where G_{adm} is related to the diagonal elements of $\mathbf{G}_o$ and $\mathbf{G}_e$ of Fig. 2.3, m_v and c_v are respectively the virtual inertia and virtual damping, and β_x is a parameter that defines the desired force amplification between the operator (β_o for $\mathbf{G}_o$) and the environment (β_e for $\mathbf{G}_e$).

Here, the human force is amplified by a factor of 5, thereby, $\beta_o = 1$ and $\beta_e = 1/5$. The robot manipulator dynamics used for the optimization example of the bilateral interaction is that of a seven-dof Kuka LWR (Albu-Schäffer et al. [2007]) with two six-axis force/torque sensors, one at the end-effector for the environment input and another one on the fourth link, just upstream from the spherical wrist, for the operator input. The experimental set-up is shown in Fig. 2.6.

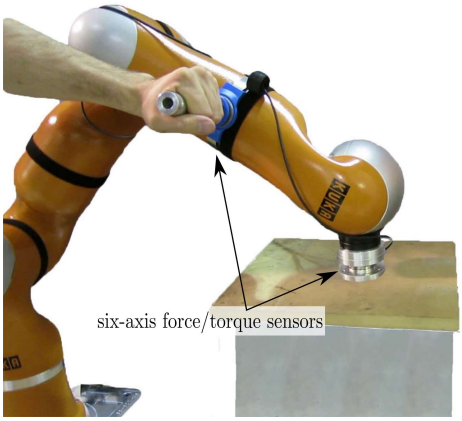

FIGURE 2.6 – The seven-dof Kuka LWR with two six-dof force/torque sensors used for the experimentation and optimization.

The next step, after establishing the control loop and robot dynamics, is to define the human and environment uncertain dynamics for the computation of the complementary stability. An appropriate choice for the human uncertain impedance parameters is given in Buerger and Hogan [2007], namely $m_o \in [0.1, 4.1]$ kg, $c_o \in [0.01, 41]$ Ns/m, and $k_o \in [1, 401]$ N/m. The environment uncertain impedance is slightly more complex to estimate. Based on the experiments performed by the authors, it is believed that the range of parameters used in Peer and Buss [2008] is in fact too soft. The minimum and maximum stiffness have thus been increased to represent a stiffer environment and exclude free motion and soft interactions. In other words, only bilateral interactions with stiff environments are considered for the force amplification control optimization. The damping has also been increased. Therefore, the environment uncertain impedance parameters are given by $m_e \in [0.1, 1]$ kg, $c_e \in [50, 300]$ Ns/m, and $k_e \in [4 \times 10^4, 2.6 \times 10^5]$ N/m. Thereafter, a certain robot configuration is assumed which is the static position depicted in Fig. 2.13. Then, the complementary stability is verified for a range of potential controller parameters $(\beta_o/c_v, m_v/c_v)$, and can be visualized in Fig. 2.7 for the z-direction, where a robust stability margin below one is considered unstable (represented in white). With the stable parameters confirmed, the costs can be computed. The results for the three intermediate performance costs are shown in Fig. 2.8, 2.9 and 2.10.

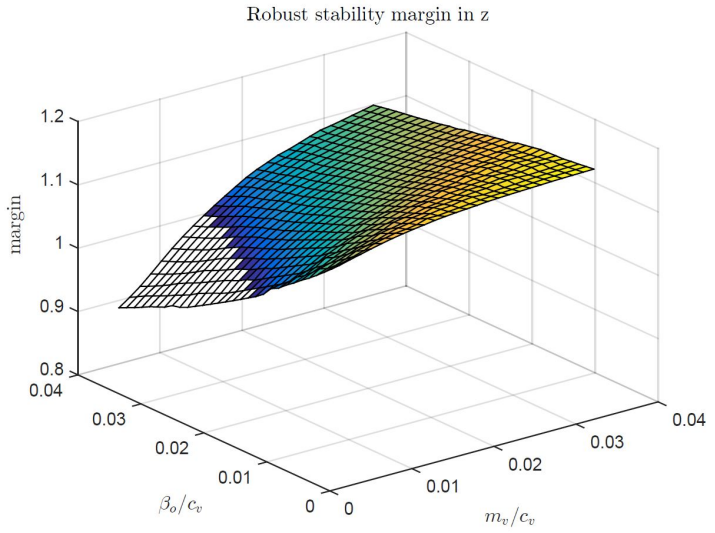

FIGURE 2.7 – Robust stability margin which establishes whether the system is complementary stable for the z-direction. A margin ≥ 1 leads to a robustly stable interaction.

It is reassuring to see that classical servo design behaviours are observed. Indeed, the amplification index, which assesses the tracking performance, tends to give better results mostly for high DC gain, β_o/c_v. On the other hand, the ITAE index, assessing the time response, tends to be much more influenced by a low time constant, m_v/c_v. Meanwhile, the transparency index yields a lower cost for lower DC gains as the infinite environment impedance is transmitted on a larger bandwidth. The global performance cost is also depicted in Fig. 2.11 and reveals that the lowest possible time constant, limited by the robot hardware, leads to the optimal performance.

However, in order to compare different controller dynamics, including distinct sets of parameters, the approach has to be slightly modified. Indeed, each normalized performance index in (2.26) must be computed in terms of the minimum and maximum values of all the different controllers. This way, they are set on the same baseline and their summation results in a meaningful global cost C. For instance, if n different controllers are to be studied, the minimum and maximum costs for the computation of each unity-based normalized index becomes

$$C_{xmin} = min(|\mathbf{C}_{x1}|, |\mathbf{C}_{x2}|, ..., |\mathbf{C}_{xn}|) \tag{2.30}$$

$$C_{xmax} = max(|\mathbf{C}_{x1}|, |\mathbf{C}_{x2}|, ..., |\mathbf{C}_{xn}|) \tag{2.31}$$

where the index x is, again, referring to the different indices (β, T, or I).

Using this approach, a PI controller, an admittance controller and a lead/lag controller have been compared. The PI controller is known to yield good results for bilateral systems and is

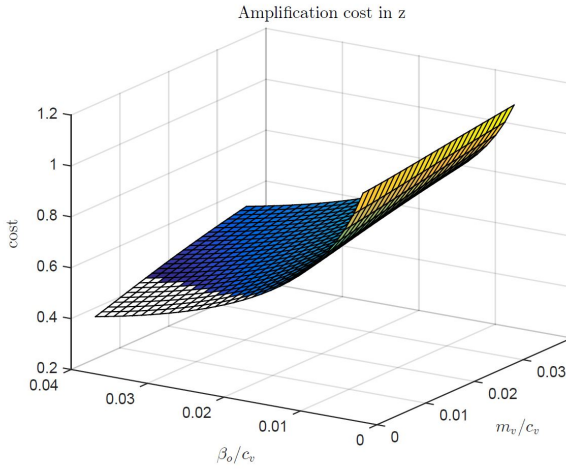

FIGURE 2.8 – Cost related to the amplification index in the z-direction. A low amplification cost leads to better tracking performance.

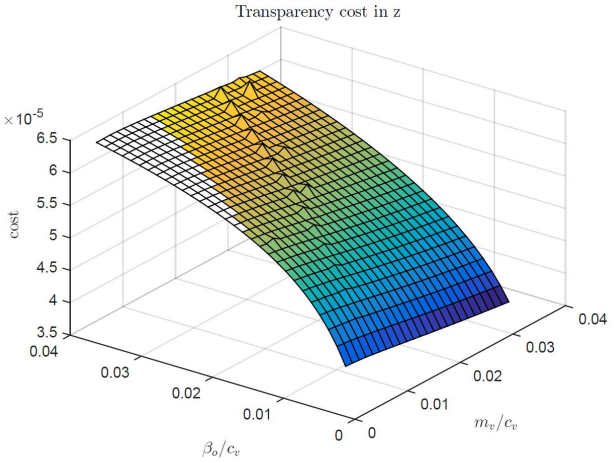

FIGURE 2.9 – Cost related to the transparency index for the z-direction. A low transparency cost leads to better environment impedance transmission.

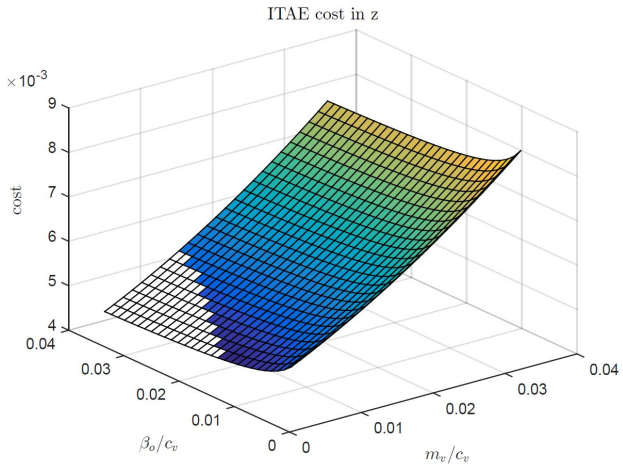

FIGURE 2.10 – Cost related to the ITAE index for the z-direction. A low ITAE cost leads to faster time response.

often used due to its simplicity. By contrast, the admittance controller is known for its effective haptic rendering that is highly appreciated for unilateral human-robot interaction, but is often forsaken for bilateral interaction due to its poor performance for stiff environments (Ott et al. [2010]). Lead and lag controllers are hardly used in this field of robotics but the positive results presented in Buerger and Hogan [2007] make them interesting controllers to evaluate, even if a qualitative study would be necessary to assess the intuitiveness of the resulting unilateral interaction. The following lead/lag controller form has been used to assess the optimal lead

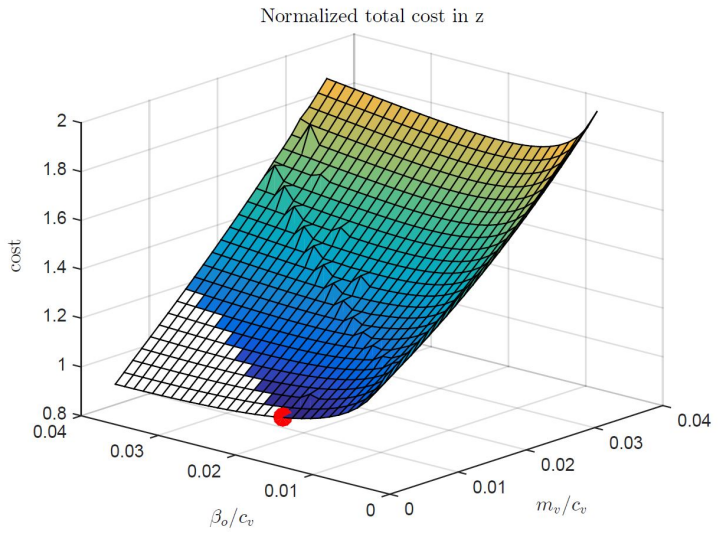

FIGURE 2.11 – Global cost of the normalized performance indices in the z-direction with $\mathbf{w}^T = [1, 1, 1]$. The red dot represents the optimal set of parameters

or lag controller for a bilateral amplification task :

$$G_{ll} = K_{ll}\frac{s+z}{s+p}. \tag{2.32}$$

The gain K_{ll}, the zero frequency z and the pole frequency p are therefore the three parameters to optimize. The comparative results, presented in table 2.1, demonstrate overall that the admittance controller leads to better results than the PI, even if the latter yields a slightly better performance for the transparency index. The main difference comes from the ITAE index and is depicted in Fig. 2.12 for a 5 Hz operator force amplification. This pursuit example, performed on the experimental set-up shown in Fig. 2.6 with the optimal PI and admittance controllers, clearly demonstrates the faster transient response of the admittance. However, it is found that a lag compensator can analytically outperform the admittance. It thus reveals that the lead/lag controller form should also be viewed as a viable type of compensation for bilateral interactions. Although the lag compensator presents better performances it would be interesting, with the results at hand, to prove that an admittance control can be highly efficient in a stiff multi-dof bilateral interaction context. This could encourage the use of such a controller for all types of bilateral tasks, not only for soft contacts. Therefore, further optimizations related to the multi-dof nature of the Kuka-LWR have been carried out with the admittance controller.

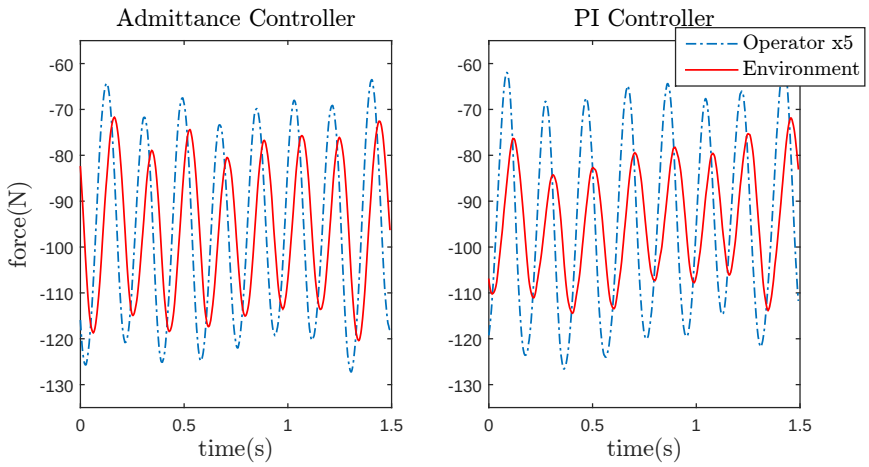

FIGURE 2.12 – High-frequency amplification pursuit for an admittance and a PI controller. The operator force is amplified 5 times for comparison purposes.

TABLE 2.1 – Best relative global costs of different control schemes and their corresponding criteria.

	ITAE	Transparency	Amplification	Global
PI	0.0451	5.636×10^{-5}	0.6338	0.3527
Admittance	0.0051	6.168×10^{-5}	0.4360	0.1606
Lead/lag	8.730×10^{-4}	6.452×10^{-5}	0.3147	0.0746

2.6 Multi-DoF Optimization

A major control issue with multi-dof robots is that their dynamics are configuration dependent. In order to assess the optimal controller for a multi-dof robot amplification, it is thus necessary to find a variable that describes the changes in dynamics related to the different joint configurations. Identifying the optimal controller parameters related to such a variable would lead to a regulator that is optimal for all configurations of the manipulator. An interesting approach to this problem is the joint stiffness matrix mapping the joint torques, $\boldsymbol{\tau}$, to the joint displacements, $\delta\theta$, (Salisbury [1980]), such that

$$\boldsymbol{\tau} = \mathbf{K}_\theta \delta\boldsymbol{\theta} \tag{2.33}$$

where $\mathbf{K}_\theta$ is the joint stiffness matrix. Considering that the control is computed in the Cartesian space, a joint-dependent variable that maps the relationship between the end-effector generalized displacements, $\delta\mathbf{x}$, and forces, $\mathbf{f}$, is thus more appropriate. Therefore, with the use of the manipulator Jacobian, enabling the following relationships :

$$\boldsymbol{\tau} = \mathbf{J}^T\mathbf{f}, \tag{2.34}$$

$$\mathbf{J}\delta\boldsymbol{\theta} = \delta\mathbf{x}, \tag{2.35}$$

it becomes straightforward with (2.33) to find the coveted relationship, such that

$$\delta \mathbf{x} = (\mathbf{J}\mathbf{K}_\theta{}^{-1}\mathbf{J}^T)\mathbf{f} \tag{2.36}$$

where $(\mathbf{J}\mathbf{K}_\theta{}^{-1}\mathbf{J}^T)$ is referred to as the Cartesian compliance matrix. Here, the joint stiffness matrix is diagonal and all joints are assumed to have the same stiffness, thus $\mathbf{K}_\theta = diag\{1, 1, 1, 1, 1, 1\}$ [1]. Equation (2.36) is a direct relationship between the Cartesian forces and the Cartesian displacements at the end-effector using only the Jacobian transformation — which is an index of the joint configuration. In other words, the Cartesian compliance matrix introduces a measurement of the variation of the end-effector dynamics related to the manipulator configuration, and may be used to find the optimal controller parameters.

2.6.1 Continuous Gain Scheduling

The next step is to perform the optimization on a set of different configurations generating different compliance values. Therefore, the seven-dof Kuka LWR showed in Fig. 2.6 has been used to conduct the current analysis and the corresponding experimentation. The chosen configuration set includes 20 consecutive end-effector positions that produce a horizontal displacement along the robot's Cartesian x-axis, as depicted in Fig. 2.13.

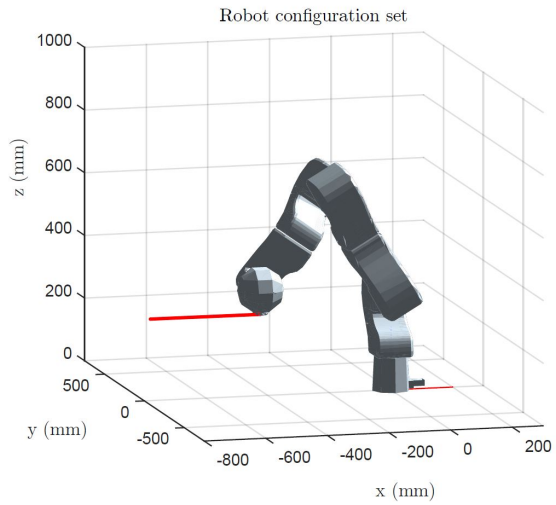

FIGURE 2.13 – End-effector horizontal displacement that generates the manipulator configuration set used for the optimization analysis.

The complementary stability as well as the optimization are then evaluated for each configuration. Afterwards, the different gains, β_o/c_v, and time constants, m_v/c_v, obtained with the algorithm are plotted with their related compliance in Fig. 2.14.

1. The joint stiffness may be set arbitrarily and will affect all indices equally

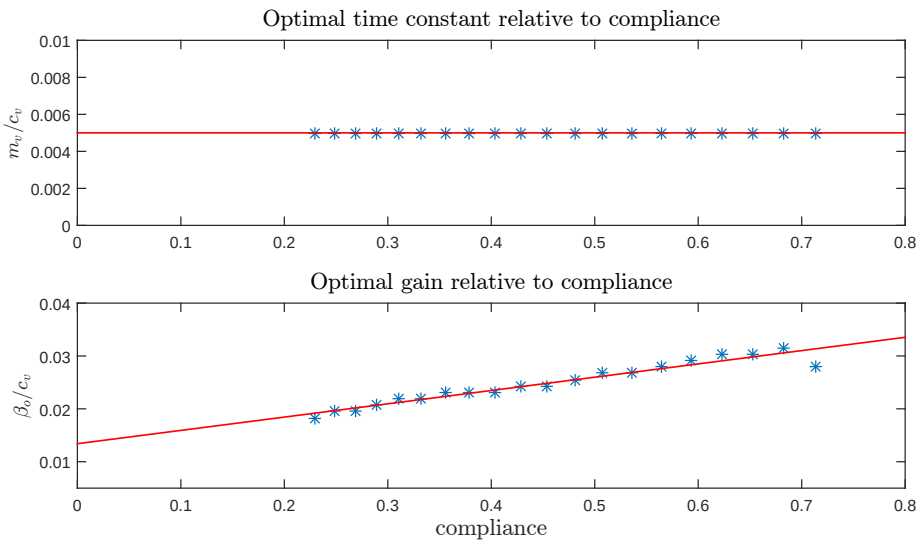

FIGURE 2.14 – Optimal m_v/c_v and β_o/c_v values relative to the manipulator compliance along the z-axis, and therefore the robot configuration.

Here, only the relationship with the axis including the wider range of compliance values along the evaluated trajectory is shown, i.e., the z-axis. As expected, regardless of the configuration, the optimal m_v/c_v parameter value is the lowest frequency limit that the hardware can support. On the other hand, the optimal β_o/c_v parameter value appears to change linearly with the manipulator compliance.

In other words, the stiffer the configuration becomes, the more the gain needs to be scaled down. This result is rather intuitive and goes along with the typical effect of a DC gain variation for servo design. This interesting result leads to a simple gain scheduling law that solves the dynamics issue with multi-dof manipulators, and thereby yields an optimal bilateral amplification for all configurations. It is important to note that this relationship is optimal for the specific range of impedance dynamics (impedance of the human operator and of the stiff environment) evaluated with the robust stability analysis. For instance, using a lower bound on the environment stiffness would shift down the relationship between the gain and the compliance.

2.6.2 Impact Tests

The coupled stability and the performance were tested with manually generated impact motions on three different surfaces that were respectively below, inside, and above the range of stiff environment k_e evaluated in the algorithm. The objective is to verify whether the parameters found can work outside of the optimization set. These surfaces are : a stiff spring

(stiffness = 5.12×10^3 N/m), a rubber stopper (stiffness = 9.15×10^4 N/m), and a 100×100 mm aluminum square tube (stiffness >> $k_{e\,max}$). The operator produced a 20 N impact that was amplified five times to generate an output of 100 N on the environment. During this amplification, unilateral motions in the other Cartesian directions were controlled using an admittance controller but with different parameter values than the one used for bilateral interactions. The results for a *stiff* manipulator configuration with a compliance around 0.2 m/N are shown in Fig. 2.15 for three distinct sets of controller parameters.

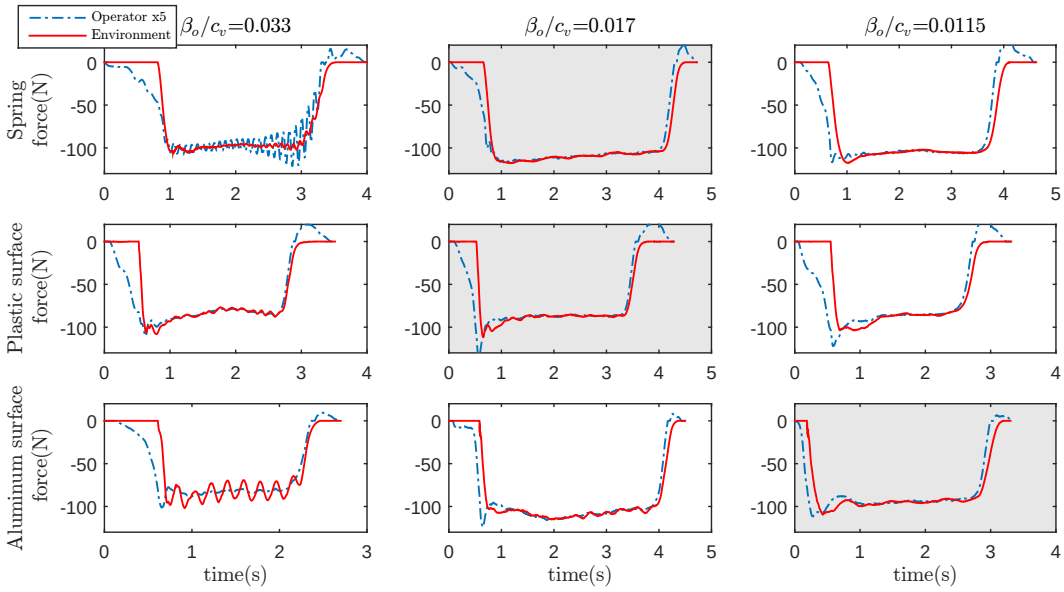

FIGURE 2.15 – Impact tests on three different environments, namely a spring, a plastic surface, and an aluminum surface, for three distinct values of parameter β_o/c_v of the admittance controller. The operator force is amplified 5 times for comparison purposes. The best response for each surface is identified by a shaded background.

From the linear gain scheduling presented in Fig. 2.14, the optimal β_o/c_v parameter value should be between 0.015 and 0.02 for an environment stiffness between 4×10^4 and 2.6×10^5 N/m. Thereby, gains of 0.0115, 0.017, and 0.033 have been chosen to study the optimization outputs. Parameter m_c/c_v is kept constant at 0.005 for all tests.

Any oscillation or vibration felt by the operator was sorted out by the performance criteria. Indeed, undesirable oscillations appear when admittance regulator gains are too high for a specific manipulator configuration as it is depicted in Fig. 2.15 for $\beta_o/c_v = 0.033$. Both the rubber and the aluminum surfaces induce instability but the aluminum surface, being stiffer, generates larger oscillations. The interaction with the spring is also clearly unstable for this gain value, but in that case the system could not keep up with the amplified force on the

environment without creating a divergent force on the operator. For the optimal gain value $\beta_o/c_v = 0.017$, the impact on the aluminum surface does not produce a perfectly stable interaction, unlike the impacts on the rubber surface and the spring that lead to fast and precise responses. The smallest gain value $\beta_o/c_v = 0.0115$ suits better the harder surface but it is slightly slower, as it can easily be seen for the transition phases of the spring and rubber amplifications. Indeed, a gain lower than the optimal value slows down the response and in extreme cases could lead to a stiction effect when quick pull-offs are performed. This effect is depicted in Fig. 2.16 for a 0.15 second stiction which required an additional 4 N to rapidly move the end-effector. However, that necessary additional force remained unfelt by the operator.

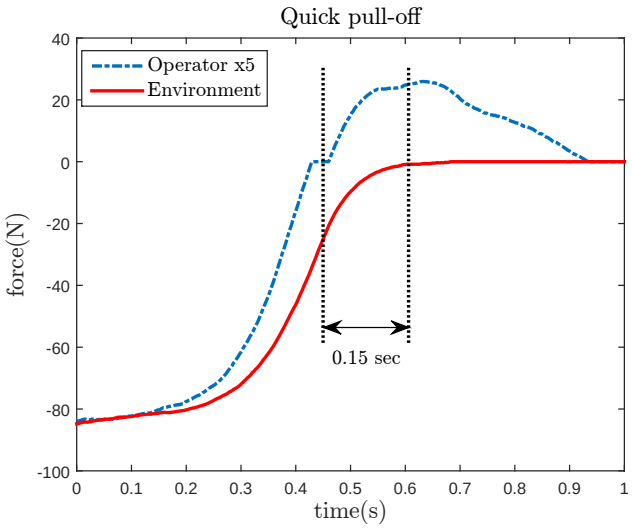

FIGURE 2.16 – Demonstration of an unfelt small stiction effect for a quick pull-off.

These experiments reveal that the optimization technique is thus effective for the environment (rubber stopper) that is contained within the range of uncertainties previously evaluated. It also demonstrates that it can accommodate different environments that are outside of this range (softer or stiffer) while providing reasonably good results. In summary, the optimization algorithm developed here allows to find a controller that yields extremely high performance while remaining robustly stable for pre-defined interaction environments for a mutli-dof robotic manipulator whose dynamics vary greatly with the configuration.

2.7 Video Demonstration

The accompanying video, featuring the seven-dof Kuka LWR, demonstrates the effectiveness of the control gain scheduling resulting from the optimization (*Chap2_Control_Opt.mp4*).

The first part consists of a horizontal amplification combined with a vertical displacement. This human-robot interaction shows the variation of the gain β_o/c_v as a function of the manipulator's Cartesian compliance in the direction normal to the interaction surface. The second part presents the impact test performed in order to evaluate the optimal controller previously found with the optimization algorithm. Unstable and stable behaviour, using respectively a high gain and a gain scheduling, are demonstrated with a spring and an aluminum surface. The video is available at

http://robot.gmc.ulaval.ca/publications/these-de-doctorat

2.8 Conclusion

In this chapter, a procedure to assess the complementary stability of a bilateral system was presented. The specific case of force amplification with a multi-dof manipulator was studied in order to optimize the parameter values of well-known controller structures used for unilateral interactions. The optimization technique is based on three distinct performance indices, namely the amplification, the transparency, and the ITAE. This approach allows to compare different control architectures. This method is also a powerful tool to address control issues with varying dynamics. However, it is required to have a configuration-related variable, which is defined here as the Cartesian manipulator compliance matrix. A relationship between the compliance and the different control parameters can then be obtained. The impact tests carried out with a seven-dof Kuka LWR demonstrated the high performance and robust stability achieved with the optimal control parameters.

The main focus of the chapter was on force amplification, but a interesting future study with this optimization approach would be to assess the optimal position of the operator's handle on the manipulator in order to obtain the best transparency. The optimal amplification parameters for the Cartesian torques could also be evaluated since only the forces have been studied up to now. Moreover, it would be interesting to test different configuration-related variables such as the Conservative Congruence Transformation (CCT) (Li and Kao [2003]). Although it has been demonstrated that the controller optimization algorithm developed here is an adequate tool for a single robot multi-dof bilateral amplification, it is important to note that the general framework presented can be extended to various unilateral or bilateral interactions, as well as haptics. Since little work as been done on the optimal performance related to the robot configuration, it is also interesting to investigate whether the gain scheduling resulting from the optimization could provide a means of obtaining the best multi-dof performance regardless of the robot varying dynamics, for all kinds of manipulators.

2.9 Appendix

2.9.1 Compliant Manipulator and Controller Dynamics

Remark : All variables used in the appendix are defined in the following figure captions. The values of the model parameters used for the Kuka LWR are determined from the information given in Albu-Schäffer et al. [2007] and are listed online at

robot.gmc.ulaval.ca/fileadmin/share/kuka_parameters.pdf

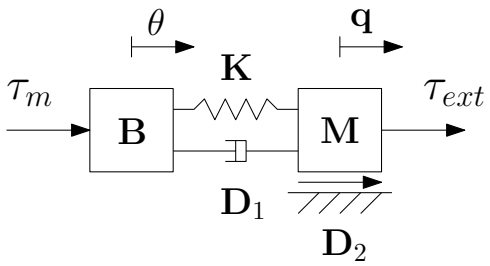

FIGURE 2.17 – Schematic representation of a compliant robotic manipulator. The actuators inertia matrix $\mathbf{B}$ and the links inertia matrix $\mathbf{M}$ are connected by the stiffness matrix $\mathbf{K}$ and the damping matrix $\mathbf{D}_1$. The centripetal and Coriolis force matrix $\mathbf{D}_2$ is acting on the links. The actuators torque vector and the external torque vector are respectively represented by $\boldsymbol{\tau}_m$ and $\boldsymbol{\tau}_{ext}$, while $\boldsymbol{\theta}$ and $\mathbf{q}$ are the vectors of joint coordinates associated with the actuators and the links.

The dynamic model of the Kuka LWR is based on the elastic joint model defined in Spong [1987] and can be derived from the schematic representation given in Fig. 2.17, as follows

$$\mathbf{M}(\mathbf{q})\ddot{\mathbf{q}} + \mathbf{D}_2(\mathbf{q},\dot{\mathbf{q}})\dot{\mathbf{q}} = \mathbf{K}(\boldsymbol{\theta} - \mathbf{q}) + \mathbf{D}_1(\dot{\boldsymbol{\theta}} - \dot{\mathbf{q}}) - \boldsymbol{\tau}_{ext}, \tag{2.37}$$

$$\mathbf{B}\ddot{\boldsymbol{\theta}} + \mathbf{K}(\boldsymbol{\theta} - \mathbf{q}) + \mathbf{D}_1(\dot{\boldsymbol{\theta}} - \dot{\mathbf{q}}) = \boldsymbol{\tau}_m \tag{2.38}$$

where the external torque vector $\boldsymbol{\tau}_{ext}$ includes the operator and the environment forces and yields

$$\boldsymbol{\tau}_{ext} = \mathbf{J}_o^T\mathbf{F}_o - \mathbf{J}_e^T\mathbf{F}_e. \tag{2.39}$$

The friction torques are neglected in the dynamics equations and the gravity torques can be removed thanks to the gravity compensation included in the Kuka's joint state feedback controller given in Albu-Schäffer et al. [2007]. Therefore, the position control law without the gravity vector yields

$$\boldsymbol{\tau}_m = -\mathbf{K}_P(\boldsymbol{\theta} - \boldsymbol{\theta}_d) - \mathbf{K}_D\dot{\boldsymbol{\theta}} - \mathbf{K}_T\boldsymbol{\tau} - \mathbf{K}_S\dot{\boldsymbol{\tau}} \tag{2.40}$$

where the spring torque vector $\boldsymbol{\tau}$ is defined by

$$\boldsymbol{\tau} = \mathbf{K}(\boldsymbol{\theta} - \mathbf{q}), \tag{2.41}$$

but where the desired motor position vector is defined with the gravity vector $\mathbf{g}(\mathbf{q}_d)$ and yields

$$\boldsymbol{\theta}_d = \mathbf{q}_d + \mathbf{K}^{-1}\mathbf{g}(\mathbf{q}_d). \tag{2.42}$$

However, considering that the gravity vector remains nearly constant for an amplification task it is possible to say, for the desired motor velocity vector, that $\dot{\boldsymbol{\theta}}_d \approx \dot{\boldsymbol{q}}_d$. Note that this assumption is taken because the outer control of the manipulator relates the external forces to desired velocities.

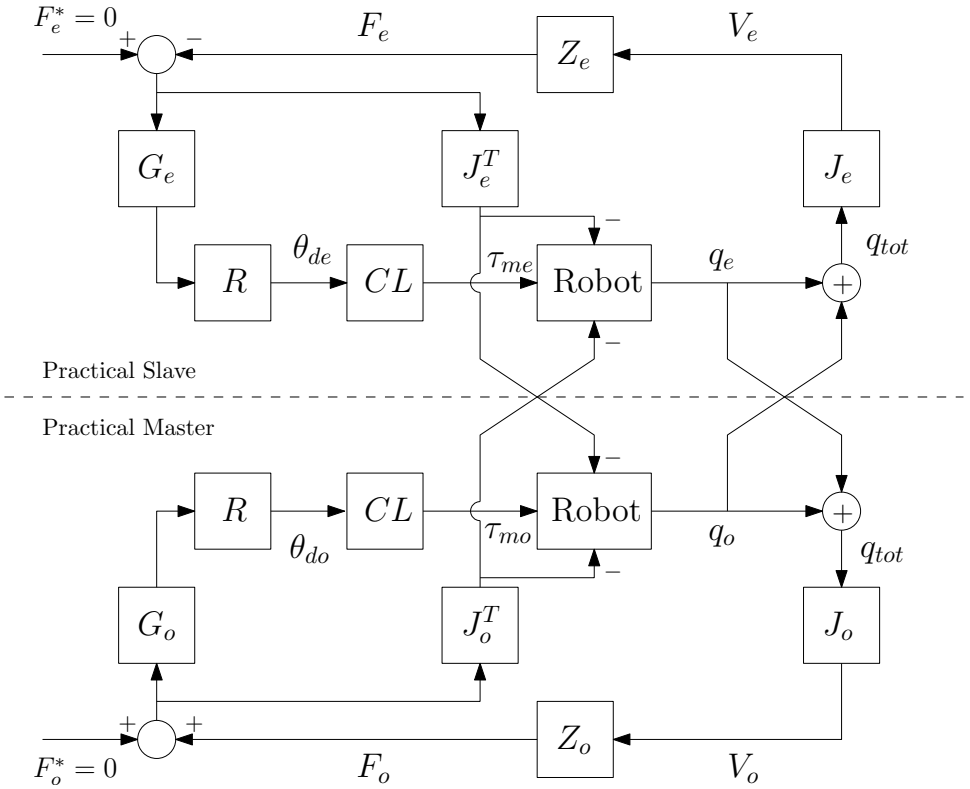

FIGURE 2.18 – Extended block diagram of the bilateral interaction for a practical slave and a practical master. In reality there is only one manipulator, thereby both practical manipulators have the same redundancy resolution $\mathbf{R}$, control model CL, robot model *Robot*, and the same total joint position output vector $\mathbf{q}_{tot}$. However, $\mathbf{Z}_o$, $\mathbf{V}_o$, $\mathbf{F}_o$, $\mathbf{F}_o^*$, $\mathbf{G}_o$, $\mathbf{J}_o$, $\boldsymbol{\theta}_{do}$, $\boldsymbol{\tau}_{mo}$, and $\mathbf{q}_o$ are respectively, the human operator impedance matrix and velocity vector, the operator force vector that is applied on the practical master, the exogenous operator force input vector, the operator regulator matrix, the operator Jacobian matrix, the operator desired motor position vector, the operator motor torque command vector, and the operator joint position vector while $\mathbf{Z}_e$, $\mathbf{V}_e$, $\mathbf{F}_e$, $\mathbf{F}_e^*$, $\mathbf{G}_e$, $\mathbf{J}_e$, $\boldsymbol{\theta}_{de}$, $\boldsymbol{\tau}_{me}$, and $\mathbf{q}_e$ are defined similarly but for the environment.

In order to use the teleoperation analysis tools, the control architecture is divided in two virtually different manipulators, namely the practical master interacting with the human operator and the practical slave interacting with the environment. Each practical manipulator has its own torque command, which is $\boldsymbol{\tau}_{mo}$ for the practical master and $\boldsymbol{\tau}_{me}$ for the practical slave. The corresponding extended control architecture is shown in Fig. 2.18 and the following mathematical development evaluates the output position of each practical manipulator, namely $\mathbf{q}_o$ and $\mathbf{q}_e$. According to the block diagram, the desired motor position vector is thus

given by

$$\boldsymbol{\theta}_{dx} = \mathbf{R}\mathbf{G}_x\mathbf{F}_x \tag{2.43}$$

where $\boldsymbol{\theta}_{dx}$, $\mathbf{G}_x$, and $\mathbf{F}_x$ can be $\boldsymbol{\theta}_{do}$, $\mathbf{G}_o$, and $\mathbf{F}_o$, or $\boldsymbol{\theta}_{de}$, $\mathbf{G}_e$, and $\mathbf{F}_e$. It is recalled that the redundancy resolution $\mathbf{R}$ includes an integrator.

Linearising equation (2.37) with $\mathbf{M}$ and $\mathbf{D}_2$ as constants allows to express the equations of dynamics in the Laplace domain as follows

$$(\mathbf{M}s^2 + \mathbf{D}_2 s + \mathbf{D}_1 s + \mathbf{K})\mathbf{q}_x = (\mathbf{D}_1 s + \mathbf{K})\boldsymbol{\theta}_x - \boldsymbol{\tau}_{ext}, \tag{2.44}$$

$$(\mathbf{B}s^2 + \mathbf{D}_1 s + \mathbf{K})\boldsymbol{\theta}_x = (\mathbf{D}_1 s + \mathbf{K})\mathbf{q}_x + \boldsymbol{\tau}_{mx} \tag{2.45}$$

and the control law (2.40) with equations (2.41) and (2.43) leads to

$$\boldsymbol{\tau}_{mx} = \mathbf{G}_1\boldsymbol{\theta}_x + \mathbf{G}_2\mathbf{q}_x + \mathbf{G}_{fx}\mathbf{F}_x \tag{2.46}$$

where

$$G_1 = -(\mathbf{K}_D + \mathbf{K}_S\mathbf{K})s - \mathbf{K}_P - \mathbf{K}_T\mathbf{K}, \tag{2.47}$$

$$G_2 = (\mathbf{K}_S\mathbf{K})s + \mathbf{K}_T\mathbf{K}, \tag{2.48}$$

$$G_{fx} = \mathbf{K}_P\mathbf{R}\mathbf{G}_x, \tag{2.49}$$

and $\boldsymbol{\tau}_{mx}$, $\boldsymbol{\theta}_x$, and $\mathbf{q}_x$ can be $\boldsymbol{\tau}_{mo}$, $\boldsymbol{\theta}_o$, and $\mathbf{q}_o$ or $\boldsymbol{\tau}_{me}$, $\boldsymbol{\theta}_e$, and $\mathbf{q}_e$. Then, in order to close the loop on one practical manipulator, equation (2.46) is substituted into equation (2.45) as follows

$$\mathbf{A}_1\boldsymbol{\theta}_x = \mathbf{A}_4\mathbf{q}_x + \mathbf{G}_{fx}\mathbf{F}_x \tag{2.50}$$

where

$$\mathbf{A}_1 = \mathbf{B}s^2 + \mathbf{D}_1 s + \mathbf{K} - \mathbf{G}_1, \tag{2.51}$$

$$\mathbf{A}_4 = \mathbf{D}_1 s + \mathbf{K} + \mathbf{G}_2, \tag{2.52}$$

and equation (2.50) can be solved for $\boldsymbol{\theta}$ such that

$$\boldsymbol{\theta}_x = \mathbf{A}_1^{-1}[\mathbf{A}_4\mathbf{q}_x + \mathbf{G}_{fx}\mathbf{F}_x]. \tag{2.53}$$

Afterwards, equations (2.53) and (2.39) are substituted into (2.44), which yields

$$\mathbf{A}_2\mathbf{q}_x + \mathbf{J}_o^T\mathbf{F}_o - \mathbf{J}_e^T\mathbf{F}_e = \mathbf{A}_3\mathbf{A}_1^{-1}[\mathbf{A}_4\mathbf{q}_x + \mathbf{G}_{fx}\mathbf{F}_x] \tag{2.54}$$

where

$$\mathbf{A}_2 = \mathbf{M}s^2 + (\mathbf{D}_1 + \mathbf{D}_2)s + \mathbf{K}, \tag{2.55}$$

$$\mathbf{A}_3 = \mathbf{D}_1 s + \mathbf{K}. \tag{2.56}$$

Equation (2.54) can then be solved for $\mathbf{q}_x$, yielding

$$\mathbf{q}_x = [\mathbf{A}_1\mathbf{A}_3^{-1}\mathbf{A}_2 - \mathbf{A}_4]^{-1}[\mathbf{G}_{fx}\mathbf{F}_x - \mathbf{A}_1\mathbf{A}_3^{-1}\mathbf{J}_o^T\mathbf{F}_o + \mathbf{A}_1\mathbf{A}_3^{-1}\mathbf{J}_e^T\mathbf{F}_e]. \tag{2.57}$$

For each practical manipulator, the output position is thus defined as follows

$$\mathbf{q}_o = [\mathbf{A}_1\mathbf{A}_3^{-1}\mathbf{A}_2 - \mathbf{A}_4]^{-1}[(\mathbf{G}_o - \mathbf{A}_1\mathbf{A}_3^{-1}\mathbf{J}_o^T)\mathbf{F}_o + \mathbf{A}_1\mathbf{A}_3^{-1}\mathbf{J}_e^T\mathbf{F}_e] \tag{2.58}$$

and

$$\mathbf{q}_e = [\mathbf{A}_1\mathbf{A}_3^{-1}\mathbf{A}_2 - \mathbf{A}_4]^{-1}[-(\mathbf{G}_e - \mathbf{A}_1\mathbf{A}_3^{-1}\mathbf{J}_e^T)\mathbf{F}_e - \mathbf{A}_1\mathbf{A}_3^{-1}\mathbf{J}_o^T\mathbf{F}_o], \tag{2.59}$$

but considering that the master and slave are represented by the same robot, the real manipulator displacement is rather $\mathbf{q}_{tot} = \mathbf{q}_o + \mathbf{q}_e$ and yields

$$\mathbf{q}_{tot} = [\mathbf{A}_1\mathbf{A}_3^{-1}\mathbf{A}_2 - \mathbf{A}_4]^{-1}[(\mathbf{G}_o - 2\mathbf{A}_1\mathbf{A}_3^{-1}\mathbf{J}_o^T)\mathbf{F}_o - (\mathbf{G}_e - 2\mathbf{A}_1\mathbf{A}_3^{-1}\mathbf{J}_e^T)\mathbf{F}_e]. \tag{2.60}$$

Lastly, in order to obtain the components of the two-port matrix in equation (2.3), equation (2.60) is rewritten such that $\mathbf{q}_{tot} = \mathbf{T}_o\mathbf{F}_o + \mathbf{T}_e(-\mathbf{F}_e)$ where

$$\mathbf{T}_o = [\mathbf{A}_1\mathbf{A}_3^{-1}\mathbf{A}_2 - \mathbf{A}_4]^{-1}(\mathbf{G}_o - 2\mathbf{A}_1\mathbf{A}_3^{-1}\mathbf{J}_o^T), \tag{2.61}$$

$$\mathbf{T}_e = [\mathbf{A}_1\mathbf{A}_3^{-1}\mathbf{A}_2 - \mathbf{A}_4]^{-1}(\mathbf{G}_e - 2\mathbf{A}_1\mathbf{A}_3^{-1}\mathbf{J}_e^T) \tag{2.62}$$

and then, the velocity vectors are expressed as follows

$$\mathbf{V}_o = \mathbf{J}_o\mathbf{T}_o\mathbf{F}_o + \mathbf{J}_o\mathbf{T}_e(-\mathbf{F}_e), \tag{2.63}$$

$$\mathbf{V}_e = \mathbf{J}_e\mathbf{T}_o\mathbf{F}_o + \mathbf{J}_e\mathbf{T}_e(-\mathbf{F}_e) \tag{2.64}$$

which leads to the following two-port matrix

$$\begin{bmatrix} \mathbf{Y}_{oo} & \mathbf{Y}_{oe} \\ \mathbf{Y}_{eo} & \mathbf{Y}_{ee} \end{bmatrix} = \begin{bmatrix} \mathbf{J}_o\mathbf{T}_o & \mathbf{J}_o\mathbf{T}_e \\ \mathbf{J}_e\mathbf{T}_o & \mathbf{J}_e\mathbf{T}_e \end{bmatrix}. \tag{2.65}$$

2.9.2 Considerations and Issues for Robust Stability Analysis

- For this optimization algorithm, μ-analysis is favoured as the robust stability analysis tool, mainly, because of the presence of multiple sources of uncertainty, which can thereby be rearranged into the less conservative structured uncertainty.

- The range of parameter values evaluated is firstly wide and sparse in order to find the boundaries of robust stability and the optimal region to analyze. It is then narrowed around the region of interest so that the precision and computation time are improved.

- The mathematical manipulation performed to obtain the two-port matrix (2.65) can generate state-space systems that contain a large number of state variables. It is therefore required to reduce the systems' order to avoid computation instability and limit the computation time. A balanced realization of $\mathbf{Y}_x$ is thus computed using *Matlab* in order to find the state variables having Hankel singular values smaller than 10^{-7}, which are considered as negligible for the model dynamics. These states can therefore be removed using the function *modred* with the DC gain matching approach. It is critical to check the validity and stability of the reduction before carrying on with the optimization process.

- Another well-known issue with the μ-analysis is the presence of discontinuities in the evaluated set of frequencies. Indeed, the robust stability margin can be erroneous if the destabilizing frequencies are missing in the evaluation range. There are two approaches to alleviate this problem. The first one is to add a complex parametric uncertainty to each real perturbation. This added dynamics improves the conditioning of the robust stability computation (*robuststab* function) but introduces some conservatism in the resulting margin. It is thus important to only add a small amount of complex dynamics. In this chapter, a 5 % conservatism is added with the *complexify* function. The second approach is to densify the frequency range of evaluation in order to obtain more reliable results. In fact, a combination of both approaches yields the best results. Here, uncertain frequency response data model (*ufrd* function) of every feedback interconnection $\mathbf{M}_x - \mathbf{\Delta}_x$ contains 200 frequencies $\in [10^{-2}, 10^{2}]$ rad/s which covers the human interaction range of frequency.

Chapitre 3

Variable Admittance for pHRI : from Intuitive Unilateral Interaction to Optimal Bilateral Force Amplification

Résumé

Dans cet article, une nouvelle architecture de commande pour les manipulateurs robotisés à plusieurs degrés de liberté (multi-ddls) utilisés dans un contexte d'interaction physique humain-robot (pHRI) est présentée. Un régulateur en admittance est utilisé comme structure de commande unique pour les différents modes d'interaction. Cette approche est reconnue pour la manipulation intuitive qui en résulte lors d'interactions unilatérales. Cependant, l'efficacité de ce type de commande pour les amplifications bilatérales sur des environnements rigides est souvent questionnée. Ici, des paramètres d'admittance variables sont utilisés afin d'adapter et d'optimiser la réponse du système pour toutes les dynamiques potentielles du manipulateur. Trois lois de commande variables interdépendantes sont alors présentées, à savoir, une commande unilatérale par admittance variable standard, une commande bilatérale par admittance à séquencement de gain et une commande transitionnelle continue. Un manipulateur Kuka LWR 4 à sept degrés de liberté est utilisé pour l'expérimentation et pour la démonstration de l'efficacité des algorithmes de commande. Une vidéo montrant différentes tâches de pHRI utilisant l'architecture de commande proposée est aussi fournie.

3.1 Introduction

In a previous work (Labrecque and Gosselin [2014]), the authors demonstrated the performance and the stability of a single-dof force amplification controller based on the admittance model presented in Lecours et al. [2012]. The key feature of this simple architecture is its ability to vary its parameters, which leads to a more intuitive interaction, higher performances, and

a smooth transition between the unilateral free space motion and the bilateral constrained mode.

In this chapter, an optimal multi-dof version of the pHRI controller presented in Labrecque and Gosselin [2014] using variable admittance regulators is proposed. Human dynamics, multiple modes of interaction and varying robot configurations introduce significant control challenges in terms of the performance and stability of the system. Such challenges are typically addressed using a single static controller which can be tuned to ensure stability but at the expense of performance. Alternatively, different controller structures can be used for each interaction mode in order to increase the performance. However, this approach increases complexity and can make it difficult to guarantee that the transitions between controller structures are always stable. In this chapter, it is demonstrated that a single control structure with varying parameters can result in an intuitive and optimal response for all types of interactions. Section 3.2 discusses the interaction interface and presents the general inner and outer control loops of the proposed controller structure. Then, Section 3.3 describes the variable admittance control law and its stability for unilateral interactions, followed by the optimal gain scheduling control law in Section 3.4 for bilateral interactions. The continuous transition control law is then presented in Section 3.5 for the smooth mode switching. Section 3.6 demonstrates the effectiveness of the control algorithms using three experiments. A complementary video is provided and described in Section 3.7. Finally, conclusions are presented in the last section. For the rest of the thesis, the term unilateral interaction refers to the mode in which the robot end-effector is able to move in free space with the help of one or many physical human interactions. By contrast, for a bilateral interaction, the human interaction guides the robot end-effector to apply a force to an external environment.

3.2 General control architecture

3.2.1 Interaction Interface

Cooperative force amplification implies a direct contact between the robot and the human operator and between the robot and the environment, and thus force sensors are required to measure the operator input and the environment output. For a single-dof manipulator, since there is only one moving link, both sensors are mounted at the effector (the moving link). Although having both sensors at the end-effector of a multi-dof robot has numerous advantages, this arrangement becomes less relevant for the present study. Indeed, one of the many goals of introducing human-robot cooperation in industry is to alleviate musculoskeletal problems by reducing the effort of repetitive and uncomfortable tasks. Positioning both sensors at the end-effector of the robot would allow perfect task-motion transparency, but it would also regrettably preserve the resulting arduous postures of the human operator. It is therefore desirable to mount the operator input sensor on a different manipulator link. In this work, a

7-dof redundant serial manipulator is used. A way to achieve an intuitive physical interaction for a 7-dof serial robot including a spherical wrist, is to locate the operator sensor on the fourth link. If the inverse kinematics resolution — redundancy resolution in this case — is resolved at the centre of the spherical wrist a rotational motion of the end-effector would not affect the operator sensor. This choice of location leads to theoretically pure translational motions and thereby eliminates the discomfort induced by rotational motions. It should be pointed out that the control architecture proposed in this work does not require the use of a redundant robot and that this discussion on the location of the force sensors also applies to 6-dof robots. Another option that renders an intuitive interaction is using the operator physical input directly on the manipulator's links. This is possible if torque sensors are available at each of the robot joints. In this chapter, an external six-axis force/torque sensor mounted on the fourth link of the robot and seven joint torque sensors are combined. This combination leads to the best interaction without compromising the amplification, as further explained in subsection 3.2.3 and section 3.4.

As stated in the introduction, admittance control is widely used for unilateral pHRI because of the direct relationship between its parameters and the dynamics felt by the operator as well as the resulting intuitive and stable interaction. However, admittance control is often disregarded for bilateral interactions (or for contacts with rigid environments) and is quickly replaced by impedance control (Ott et al. [2010]) or even direct force control (Lamy et al. [2009]). This decision is mainly driven by the fact that the relationship with a desired virtual dynamics is lost. A regulator with a force output would thus seem more appropriate. However, a unilateral or bilateral interaction with a human operator or a rigid surface leads to a wide range of different dynamics to regulate. A single static controller is thus rarely adequate. Moreover, when two different controllers are used, an efficient switching law has to be implemented (Shaikh and Caines [2007]) in order to avoid the flickering effect. On the other hand, a single controller with variable parameters can adapt to different interaction modes as demonstrated in Pitakwatchara et al. [2006] using a discrete control law for teleoperation and in Labrecque and Gosselin [2014] using a continuous control law for a single-dof force amplification system.

The potential benefits of using a variable admittance for bilateral interactions with different environments have been demonstrated in Labrecque and Gosselin [2015] for a multi-dof manipulator, namely, the Kuka LWR. Therefore, in this chapter, the continuous control law presented in Labrecque and Gosselin [2014] and the optimal force amplification scheme from Labrecque and Gosselin [2015] are unified in order to obtain an intuitive and versatile pHRI for a multi-dof manipulator that uses a single controller. The proposed architecture is shown in Fig. 3.1.

The control architecture includes two main loops, namely, an inner loop for the precise positioning and an outer loop for the transformation of the different interaction forces into desired motions. The components of the controller are detailed in the following subsections.

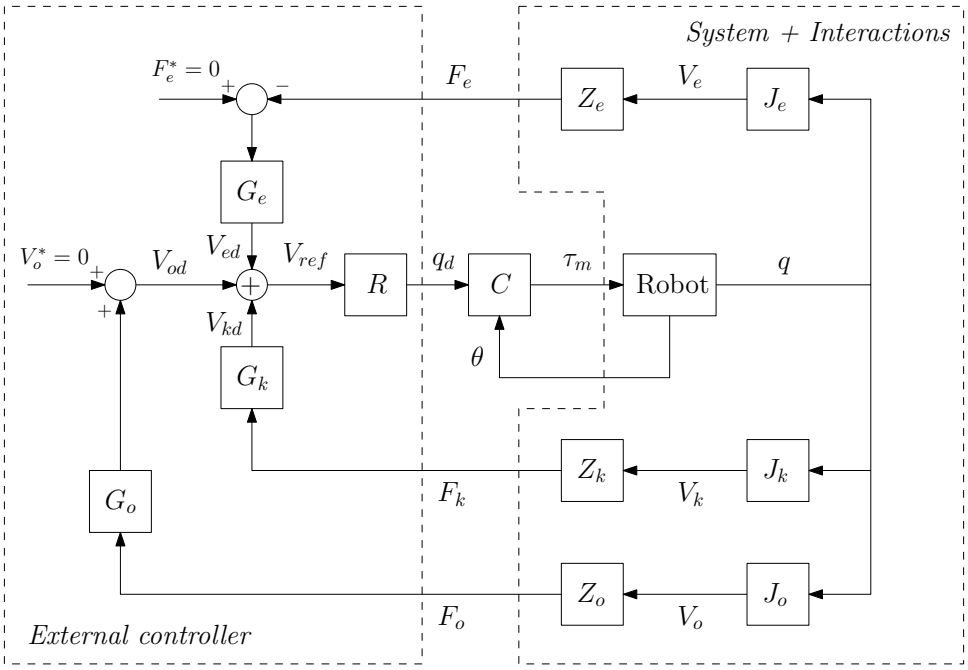

FIGURE 3.1 – General admittance control architecture proposed for a pHRI using a multi-dof manipulator. In order to not surcharged the schematic, torques generated by the external forces are excluded.

3.2.2 Inner position control

The inner controller of the proposed architecture, noted C in Fig. 3.1, of the proposed architecture can be a simple PD controller on the position command. However, since the manipulator used for the experimentation in this work is a Kuka LWR 4, the internal position control of the Kuka was selected.

The Kuka LWR is defined as a flexible manipulator and has, therefore, a particular controller in order to take into consideration the elasticity of its joints. The controller is described in Albu-Schäffer et al. [2007] and Ott et al. [2008], and hence, it is only briefly summarized in this section.

A robot with rigid links and flexible joints can be assumed to have the following dynamic model :

$$\mathbf{M}(\mathbf{q})\ddot{\mathbf{q}} + \mathbf{C}(\mathbf{q}, \dot{\mathbf{q}})\dot{\mathbf{q}} + \mathbf{g}(\mathbf{q}) = \mathbf{K}(\boldsymbol{\theta} - \mathbf{q}) - \boldsymbol{\tau}_{ext}, \tag{3.1}$$

$$\mathbf{B}\ddot{\boldsymbol{\theta}} + \mathbf{K}(\boldsymbol{\theta} - \mathbf{q}) = \boldsymbol{\tau}_m \tag{3.2}$$

where $\mathbf{M}(\mathbf{q})$, $\mathbf{C}(\mathbf{q}, \dot{\mathbf{q}})$, and $\mathbf{g}(\mathbf{q})$ are respectively the link inertia matrix, the centripetal and Coriolis vector, and the gravity vector. $\mathbf{B}$ is the diagonal actuator inertia matrix and $\mathbf{K}$ is the diagonal joint stiffness matrix. Vectors $\boldsymbol{\theta}$ and $\mathbf{q}$ are respectively the joint position vector associated with the actuators and the joint position vector associated with the links. $\boldsymbol{\tau}_{ext}$ is the external torque vector and includes the two force inputs from the operator and the

environment force input. In order to avoid overloading the schematic, the components of $\boldsymbol{\tau}_{ext}$ are not shown in Fig. 3.1. Finally, $\boldsymbol{\tau}_m$ is the actuator torque vector.

It is thus possible to define the following position control law

$$\boldsymbol{\tau}_m = -\mathbf{K}_P(\boldsymbol{\theta} - \boldsymbol{\theta}_d) - \mathbf{K}_D\dot{\boldsymbol{\theta}} + \mathbf{K}_T(\mathbf{g}(\mathbf{q}) - \boldsymbol{\tau}) + \mathbf{g}(\mathbf{q}) \tag{3.3}$$

where $\mathbf{K}_P$, $\mathbf{K}_D$, and $\mathbf{K}_T$ are the gain matrices which are defined as positive definite diagonal matrices, where the joint torque vector $\boldsymbol{\tau}$ is defined by

$$\boldsymbol{\tau} = \mathbf{K}(\boldsymbol{\theta} - \mathbf{q}), \tag{3.4}$$

and where the desired actuator position vector $\boldsymbol{\theta}_d$ is defined with the gravity vector $\mathbf{g}(\mathbf{q}_d)$ and the desired link position vector $\mathbf{q}_d$, and yields

$$\boldsymbol{\theta}_d = \mathbf{q}_d + \mathbf{K}^{-1}\mathbf{g}(\mathbf{q}_d). \tag{3.5}$$

3.2.3 Outer force to velocity control : admittance

The external controller is a summation of the different Cartesian interaction forces which are beforehand processed by admittance regulators. An admittance regulator transforms an input force into a motion command. Hence the external controller is a summation of the different Cartesian velocity commands generated by the input forces. Typically, for a single Cartesian dof, the relationship is of the form

$$f = m(\ddot{x} - \ddot{x}_t) + c(\dot{x} - \dot{x}_t) + k(x - x_t) \tag{3.6}$$

where f is the external force, m, c, and k are respectively the virtual inertia, damping and stiffness, $\ddot{x}$, $\dot{x}$, and x are the Cartesian acceleration, velocity, and position, and finally, $\ddot{x}_t$, $\dot{x}_t$, and x_t represent the desired trajectory to be followed. Since the input is coming from a physical interaction, $\ddot{x}_t$, $\dot{x}_t$, and x_t should be set to zero. The virtual stiffness, k, should also be equal to zero in order to obtain a free motion. The relationship is then rewritten as follows

$$f = m\ddot{x} + c\dot{x}. \tag{3.7}$$

It is then easy to solve the above equation for the velocity in the Laplace domain, yielding

$$\dot{X}(s) = \frac{1}{ms + c}F(s) = \frac{\frac{1}{c}}{\frac{m}{c}s + 1}F(s) = Y(s)F(s) \tag{3.8}$$

where $\dot{X}(s)$ and $F(s)$ are respectively the Laplace transforms of $\dot{x}$ and f, $Y(s)$ is the admittance, and s is the Laplace variable.

Each admittance regulator is combined with an amplification factor in order to yield priorities to a specific interface during unilateral interactions or to adjust the amplification ratio during bilateral interactions. The general external regulator matrix thus yields

$$\mathbf{G}_x = \boldsymbol{\beta}_x\mathbf{Y}_x \tag{3.9}$$

where $\boldsymbol{\beta}_x$ is the diagonal amplification factor matrix and $\mathbf{Y}_x$ is the diagonal admittance matrix.

In the control architecture of Fig. 3.1, three interaction dynamics matrices are involved. From Fig. 2.6, these potential input dynamics are the Cartesian operator impedances acting on the six-axis force/torque sensor located at the fourth manipulator link, noted $\mathbf{Z}_o$, the Cartesian operator impedances acting on the internal torque sensors, noted $\mathbf{Z}_k$, and the Cartesian environment impedances acting on the six-axis force/torque sensor located at the end-effector, noted $\mathbf{Z}_e$. These dynamics can produce three input force vectors which are, respectively, $\mathbf{F}_o$, $\mathbf{F}_k$, and $\mathbf{F}_e$. Each input force vector is passed through an external regulator matrix, $\mathbf{G}_o$, $\mathbf{G}_k$, or $\mathbf{G}_e$ which includes an amplification factor matrix, $\boldsymbol{\beta}_o$, $\boldsymbol{\beta}_k$, or $\boldsymbol{\beta}_e$, and an admittance regulator matrix, $\mathbf{Y}_o$, $\mathbf{Y}_k$, or $\mathbf{Y}_e$.

The desired velocity vectors, $\mathbf{V}_{od}$, $\mathbf{V}_{kd}$, and $\mathbf{V}_{ed}$, which are computed from the input force vectors, are added up to give the reference velocity vector $\mathbf{V}_{ref}$. For a single degree of freedom, the resulting reference velocity is expressed as follows :

$$v_{ref} = \beta_o y_o f_o + \beta_k y_k f_k + \beta_e y_e f_e. \tag{3.10}$$

In order to avoid a misinterpretation of the measured forces, when an environment force f_e is sensed at the end-effector, the amplification factor β_k associated with the internal joint force sensors is set to zero[1]. Moreover, if the controlled manipulator is in steady state during a bilateral interaction, then the desired joint position q_d should be constant and the reference velocity v_{ref} should thus be equal to zero. Equation (3.10) then yields

$$0 = \beta_o y_o f_o + \beta_e y_e f_e \tag{3.11}$$

with similar admittance parameters in y_o and y_e, which therefore leads to

$$f_o = -\frac{\beta_e}{\beta_o} f_e. \tag{3.12}$$

The operator and environment forces are thus, logically, in opposite directions and proportional with an amplification ratio of β_e/β_o, which is the desired controller behaviour.

Finally, the redundancy resolution, R in Fig. 3.1, which tranforms the Cartesian reference velocities into seven joint positions, is carefully chosen in order to render the most intuitive interaction possible. Indeed, a 7-dof manipulator can react non-intuitively to a physical human interaction. It can be caused by a singularity or by a specific resolution chosen. The typical resolution uses the Moore-Penrose generalized inverse matrix which yields the minimum norm solution. Unfortunately, a human operator can easily push the robot into a singular configuration which may yield an uncontrollable situation. A common method to avoid this issue is to add a damping factor in the resolution, as proposed by Wampler [1986] based on the Levenberg-Marquardt method (Marquardt [1963]). This technique prevents the robot from

1. The forces and torques applied at the end-effector have a direct impact in the joint torques

reaching a singular configuration but can also lead to a counter-intuitive slow-down when approaching a singularity. In order to eliminate these numerical singularities, Sugihara proposed a simple solution by using the squared norm of the residual for the damping factor (Chan and Lawrence [1988]), but with a small added bias (Sugihara [2011]). The corresponding equation to resolve the redundancy with a velocity input, $\mathbf{v}_{ref}$, and a position output, $\mathbf{q}_d$, is written as follows

$$\mathbf{q}_{d[i+1]} = \mathbf{q}_{d[i]} + \mathbf{W}_J \mathbf{J}^T (\mathbf{J}\mathbf{W}_J\mathbf{J}^T + \mathbf{W}_N)^{-1}\mathbf{e} \tag{3.13}$$

where $\mathbf{J}$ is the Jacobian matrix, $\mathbf{W}_J$ is a $[7 \times 7]$ weighting matrix, $\mathbf{W}_N$ is the damping factor and yields

$$\mathbf{W}_N = E\ \mathbf{I}_{[6\times6]} + w_N \mathbf{I}_{[6\times6]} \tag{3.14}$$

with w_N being the added small bias — in this work $w_N = 0.01$ — and with E being the squared norm

$$E = \frac{1}{2}\mathbf{e}^T \mathbf{W}_E \mathbf{e} \tag{3.15}$$

of the residual

$$\mathbf{e} = \mathbf{v}_{ref} T_s. \tag{3.16}$$

The residual is simply the reference velocity multiplied with the sampling time T_s which gives the distance between the actual position and the desired position for a single time step. The matrix $\mathbf{W}_E$ is a $[6 \times 6]$ weighting matrix. This method ensures the numerical convergence of the resolution for any input motion and is therefore used in the control architecture proposed in this chapter.

The control architecture presented is the general framework of the controlled manipulator. Indeed, in order to accommodate the different interactions it is necessary to define specific control laws for each mode. These control laws involve varying parameters and are described in the next section.

3.3 Unilateral mode

The use of the term unilateral interaction might be perceived as slightly inadequate in this chapter because of the two different means to sense the operator force input, namely, the six-axis force/torque sensor on one of the robot links and the internal joint force sensors. However, even if the operator can simultaneously use his two hands in two different locations on the manipulator, it is important to make a distinction between the interactions intended for a free motion of the end-effector (unilateral interactions) and the interactions intended for a contact of the end-effector with a rigid surface (bilateral interactions). In this section the control and stability of the unilateral mode is thus detailed.

3.3.1 Control law

When the end-effector is free to move, only the force sensor mounted on the fourth link and the joint torque sensors are active. In this mode, the controller yields a typical first order admittance dynamics. This system, based on equation (3.8), has a well-known behaviour in the time domain. It is therefore easy to infer the effect of the two parameters on the system response, namely, the inverse of the virtual damping which acts as a DC gain and the ratio of the virtual inertia over the virtual damping which acts as a time constant. The resulting dynamics, when applying an external force, can also be considered as that of a mass, m, moving in a viscous environment of damping coefficient, c. Therefore, if the admittance parameters are high then the robot will be less reactive to the sensed force. On the other hand, if they are low it will be easier to move the robot, but more difficult to control it for precise motion. In fact, it has been shown that the most intuitive pHRI can be obtained by varying the admittance parameters online according to the operator's intentions (Lecours et al. [2012], Duchaine and Gosselin [2007], Tsumugiwa et al. [2001]). The approach proposed in Lecours et al. [2012] is used here for the diagonal components of the human admittance regulator matrices, $\mathbf{Y}_o$ and $\mathbf{Y}_k$. It is briefly recalled in the following for a single dof system.

In this approach, the effective damping coefficient, noted c_{ov}, is calculated based on the nominal (default) damping coefficient, c_o, and the desired acceleration, $\ddot{x}_d$, using

$$c_{ov} = \begin{cases} c_o - \alpha|\ddot{x}_d| & \text{for acceleration} \quad (3.17) \\ c_o + \alpha|\ddot{x}_d| & \text{for deceleration} \quad (3.18) \end{cases}$$

where parameter α is used to adjust the influence of the acceleration, or deceleration, on the variation of c_{ov}.

When it is desired to accelerate, the virtual damping decreases and the effective virtual inertia, noted m_{ov}, is adjusted in order to keep a constant ratio of damping over inertia. This variation leads to a more reactive interaction for larger accelerations. However, when it is desired to decelerate, the virtual damping increases, and the virtual inertia partially decreases, which leads to a more precise positioning. The following relations are used to adjust the virtual inertia

$$m_{ov} = \begin{cases} \dfrac{m_o c_{ov}}{c_o} & \text{for accel} \quad (3.19) \\ \dfrac{m_o c_{ov}}{c_o}(1 - \eta(1 - e^{\gamma(c_o - c_{ov})})) & \text{for decel} \quad (3.20) \end{cases}$$

where m_o is the nominal virtual inertia and η and γ are parameters that are used to respectively adjust the steady state inertia over damping ratio and the rate of the transition. In the above, the desired acceleration, $\ddot{x}_d$, is computed using a discrete form of (3.7).

It is important to mention that the admittance parameters are similar for $\mathbf{Y}_o$ and $\mathbf{Y}_k$, but that the components of the amplification factor matrices, $\boldsymbol{\beta}_o$ and $\boldsymbol{\beta}_k$, can take different values

in order to prioritize a certain interaction or certain Cartesian motions. In this work, it is expected that the operator will mostly interact with the handle mounted on the fourth link. Interactions sensed on the six-dof force/torque sensor of the handle are therefore given priority.

3.3.2 Stability and performance

For pHRI, preliminary stability assessment can be done before experimentation. However, because of the varying dynamics and notion of comfort specific to human beings, it is almost always necessary to reassess the stability boundaries based on a human feedback. A pHRI study using a Kuka LWR 4 with a similar varying admittance controller for unilateral interactions (Ficuciello et al. [2014]) has experimentally evaluated the boundaries of the virtual parameters, c_{ov} and m_{ov}. In order to obtain stable interactions, the boundaries proposed in Ficuciello et al. [2014] have thus been used in this chapter for the unilateral mode. The performance preferences differ from one operator to the other and can be adjusted individually or kept to a common average.

3.4 Bilateral mode

3.4.1 Control law

When the end-effector comes into contact with the environment, the force sensor at the end-effector becomes active and the bilateral mode is enabled. The control architecture is unchanged but the admittance parameters are modified in order to take into consideration the new interaction dynamics. Indeed, a rigid surface has a highly reactive dynamics and can easily compromise the coupled stability and performance of a bilateral system. In order to obtain a stable amplification, the regulator's DC gains and time constants have to be low, and equation (3.12) has to be satisfied. This means that the admittance parameters of $\mathbf{Y}_o$ and $\mathbf{Y}_e$ have to be similar and that the amplification factors of $\boldsymbol{\beta}_k$ have to be equal to zero. Indeed, if the interactions with the joint torque sensors are kept in the control loop, then the environment forces will be numerically cancelled because of the sensor redundancy. A stable amplification will therefore be impossible.

The smooth transition to go from a mode to another is detailed in the next section. However, another important control issue appears with the use of a multi-dof manipulator for bilateral amplification. Indeed, the dynamics of a multi-dof manipulator is configuration dependent. This means that in order to obtain an optimal amplification, the admittance parameters should be adjusted according to the actual robot configuration. In Labrecque and Gosselin [2015], a single variable that describes the manipulator's configuration for each Cartesian component is used to define a varying admittance control law. This variable is based on the Jacobian transformation, $\mathbf{J}$, in order to link the effect of Cartesian forces, $\delta\mathbf{f}$, on Cartesian

displacements, $\delta\mathbf{x}$, and yields

$$\delta\mathbf{x} = (\mathbf{J}\mathbf{K}_\theta{}^{-1}\mathbf{J}^T)\delta\mathbf{f}. \tag{3.21}$$

The matrix that includes all the Cartesian configuration-dependent variables is referred to as the Cartesian compliance matrix, noted $\mathbf{H}$, and is thus

$$\mathbf{H} = (\mathbf{J}\mathbf{K}_\theta{}^{-1}\mathbf{J}^T) \tag{3.22}$$

where $\mathbf{K}_\theta$ is the joint stiffness matrix. In this case, the joint stiffness matrix is diagonal and all joints are assumed to have the same stiffness, thus $\mathbf{K}_\theta = diag\{1,1,1,1,1,1\}$. Using the Cartesian compliance matrix as a configuration index, it thus becomes possible to optimize the controller parameters for all joint configurations, as explained in the following subsection.

3.4.2 Stability and performance

The stability of a bilateral amplification using admittance regulators for a Kuka LWR 4 has been demonstrated in Labrecque and Gosselin [2015] using a robust stability analysis. More specifically, the analysis makes use of the structured singular value (Packard and Doyle [1993]) with the human and environment dynamics as bounded uncertainties. This approach allows to define a stable parameter space for the pre-defined controllers used in the system — admittance controllers in this case — and a particular joint configuration.

Once this stability analysis is done, a cost function based on three performance indices is computed in the stable parameter space in order to assess the general performance of the controller. The three performance indices are :

1. the **amplification index**, also known as the kinematic correspondence index (Chang and Kim [2012]), which assesses the amplification capability of the system,
2. the **transparency index** based on the Z-width (Colgate and Brown [1994]), which evaluates the correspondence between the environment impedance and the impedance transmitted to the operator,
3. and the **integral of the time-weighted absolute error (ITAE) index**, which assesses the settling time and the overshoot of a transient response.

A performance cost is then associated to every set of controller variables contained in the stable parameter space. The set of variables with the smallest cost is thus selected as the optimal set for the joint configuration evaluated.

In the case of admittance controllers, three variables are included for each Cartesian regulator, namely, the virtual inertia m_v where $m_o = m_e = m_v$, the virtual damping c_v where $c_o = c_e = c_v$, and the amplification factor β_o or β_e. In order to ease the optimization process, it is possible to rearrange the three variables into only two parameters, for instance, the DC gain β_o/c_v and the time constant m_v/c_v.

With the Cartesian compliance variables of matrix (3.22), it thus becomes possible to define optimal control parameters for any manipulator configuration. Using this approach, a varying admittance control law is generated for the Kuka LWR 4 for bilateral amplification. An example of the resulting control law for 20 consecutive amplification configurations, i.e., compliances, for interactions with a stiff environment (stiffness between 4×10^5 and 2.6×10^5 N/m) is shown in Fig. 3.2. The time constant m_v/c_v is kept constant to its minimum value in order to respond as fast as possible, while the DC gain β_o/c_v varies proportionally with the compliance in order to ensure stable interactions. Indeed, the stiffer the environment, the more the gain is reduced. Most of the joint configuration compliances are found to be between 0.1 and 0.7, the varying gain is therefore bounded at these limit values. The environment DC gain β_e/c_v follows the same law but with a difference proportional to the amplification ratio.

During bilateral amplification, the Cartesian compliance matrix is thereby computed in real-time and preserves the optimal continuous gain scheduling law.

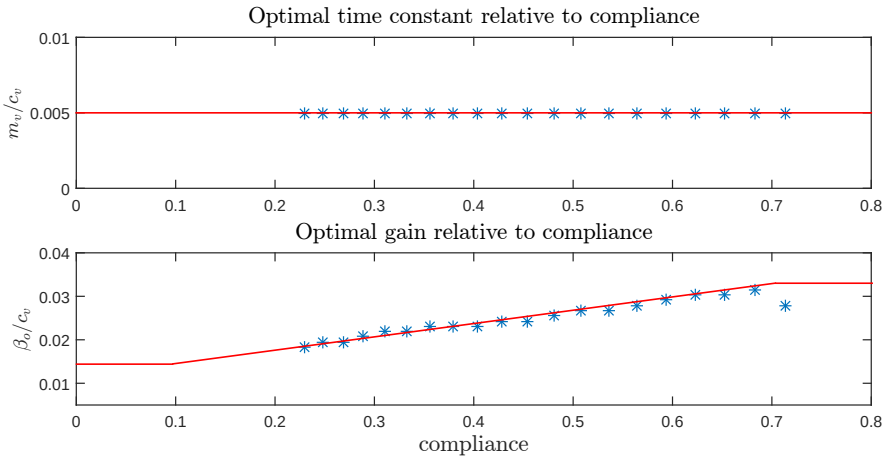

FIGURE 3.2 – Example of the gain scheduling law resulting from the optimization algorithm for bilateral amplification. The time constant m_v/c_v stays as low as possible and the DC gain β_o/c_v increases linearly with the compliance.

3.5 Transition

As explained in the previous sections, the admittance parameters have to be drastically different depending on the interaction mode. The main idea behind having the same control architecture for the two modes, namely, unilateral and bilateral, is to avoid the issues related to mode switching. Indeed, a recurrent issue for hybrid position/force control algorithms is the flickering effect that appears when the controller is switching between two states (Shaikh and Caines [2007]). Therefore, with a single adaptable controller, a smooth continuous transition can be implemented.

The transition control law consists simply in varying the current virtual inertia and damping

parameters to the desired virtual parameters. Therefore, in order to satisfy the unilateral and bilateral control laws, the admittance parameters are continuously computed for the two interaction modes depending on the manipulator's motion and configuration. Considering a single Cartesian degree of freedom, this transition law is applied when the external contact force between the robot and the environment, f_e, is contained between two selected limits noted f_{emin} and f_{emax}. The virtual damping is adjusted according to

$$c_{ov} = c_{uni} - \alpha_{amp}(|f_e| - f_{emax}) \tag{3.23}$$

where α_{amp} is defined as

$$\alpha_{amp} = \frac{c_{uni} - c_{bi}}{f_{emax} - f_{emin}} \tag{3.24}$$

in which c_{uni} and c_{bi} are the unilateral and bilateral virtual damping coefficients associated with the current manipulator motion and configuration. The virtual inertia is adjusted using

$$m_{ov} = \frac{m_o c_{ov}}{c_{uni}} e^{\gamma_{amp}(c_{ov} - c_{uni})} \tag{3.25}$$

where γ_{amp} is the smoothness parameter used to adjust the exponential transition, and yields

$$\gamma_{amp} = \frac{1}{c_{bi} - c_{uni}} \log(\frac{m_{bi} c_{uni}}{m_{uni} c_{bi}}) \tag{3.26}$$

where m_{uni} and m_{bi} are the current unilateral and bilateral virtual inertias associated with the current manipulator motion and configuration. An example is shown in Fig. 3.3 with $f_{emin} = 0$ N and $f_{emax} = 1$ N. The virtual damping changes from 20 to 50 Ns/m, and the virtual inertia changes from 4 to 0.19 kg.

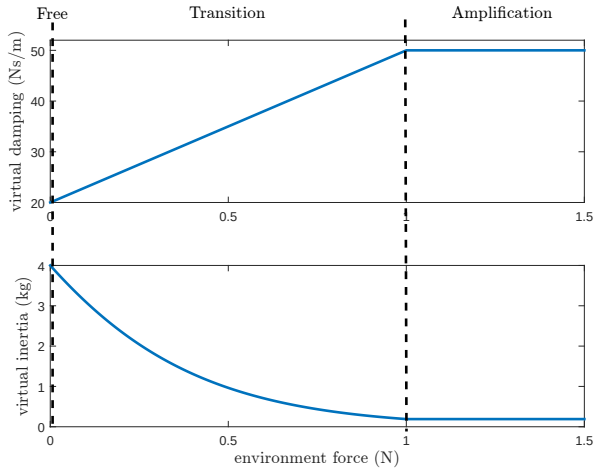

FIGURE 3.3 – Example of the effect of the transition law on the virtual damping and virtual inertia. The environment force is the contact force measured between the robot and the environment. The admittance parameters transit smoothly from the unilateral mode (free) to the bilateral mode (amplification).

This transition law generates an imperceptible switch between the two interaction modes without any flickering or sticking effect with the environment surface.

3.6 Experimentation

Three tests are presented here, which assess the stability and performance of the two control laws and their transition. The experimental setup includes a Kuka LWR 4, plus two six-axis ATI force/torque sensors, one mounted at the end-effector and the other one mounted on the fourth link of the manipulator with a handle, as shown in Fig. 3.4. The joint torque sensors were also used for the unilateral mode and an aluminium square tube was used as the rigid environment for the bilateral interaction. The parameter values for the different manipulator states are given in Table 3.1 and they satisfy the stability and performance requirements proposed in Sections 3.3, 3.4, and 3.5 for the specifications of the actual experimental setup.

TABLE 3.1 – Parameters for the experimentation.

parameter	value	parameter	value
β_o	1	β_k	0.5
c_o, c_k	20 Ns/m	β_e	0.2
m_o, m_k	4 kg	c_{bi}	30 to 70 Ns/m
α	2	m_{bi}	0.12 to 0.25 kg
η	0.1	compliance	0.1 to 0.7
γ	0.5	f_{emin}, f_{emax}	0 to 1 N

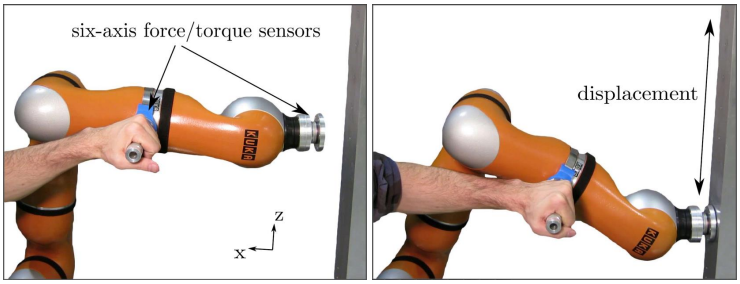

FIGURE 3.4 – Demonstration of the interaction interface with the Kuka LWR 4 (on the left) and of the horizontal amplification combined with a vertical displacement (on the right).

The first test aims at assessing the general stability and performance of the system. The task starts with a quick unilateral interaction, with the handle, in order to push the robot's end-effector against the rigid environment, which creates a strong impulse while the bilateral amplification mode is entered. The amplification is kept constant for a few seconds, and the end-effector is then pulled-off to go back to the unilateral mode. The interaction forces and the virtual damping measured while performing this task are shown in Fig. 3.5. It can be observed that the first unilateral interaction is an acceleration motion. The virtual damping is thus decreasing proportionally with the acceleration in order to ease the interaction — from 20 Ns/m down to 15.5 Ns/m — just before the end-effector hits the environment at around $t = 0.5$ second. Then, the system transits quickly to the bilateral mode with a virtual damping

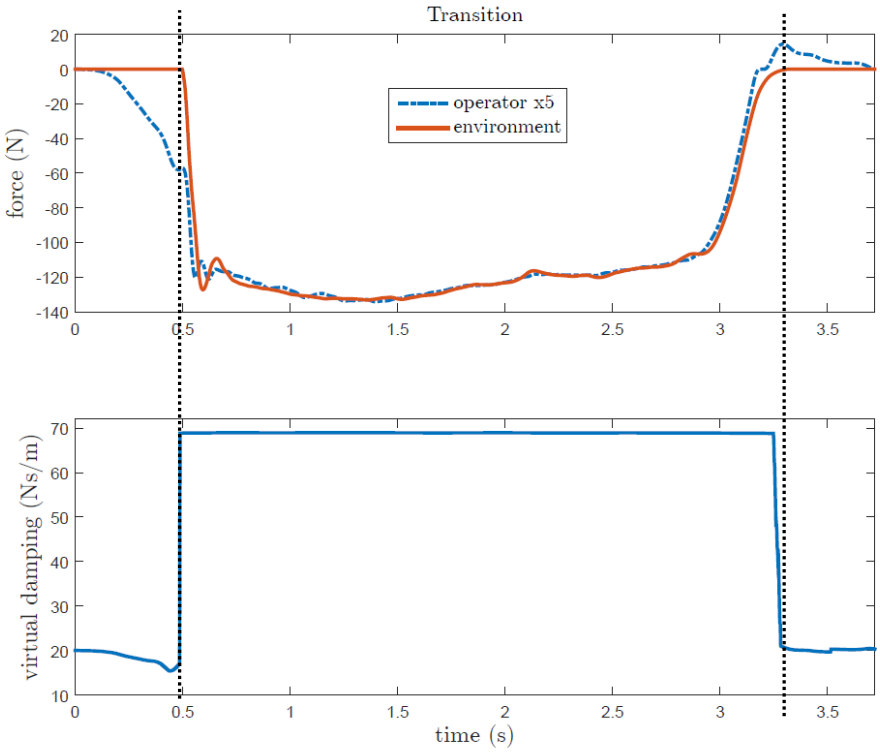

FIGURE 3.5 – Example of transition between the unilateral and bilateral interactions showing the general use of the system. The graphic of the virtual damping shows an example of the variation behaviour of the admittance parameters. The operator force is multiplied by 5 in order to provide a better visualization of the tracking quality.

around 69 Ns/m in order to reduce the overshoot and subsequently follow the commanded force — 5 times the operator force in this case. During the amplification, the end-effector is static and the operator attempts to keep a constant environment force of approximately 120 N. Small internal motions of the manipulator links slightly change the compliance, and thereby the virtual damping value — 0.1 Ns/m. However, this is imperceptible and not visible on the graph. The test ends with the pull-off at around $t = 3$ seconds where the action of the transition law is visible. Indeed, when the environment force reach -1 N at around $t = 3.25$ seconds the virtual damping is gradually decreased to the desired unilateral value. At the same time, this smooth mode transition generates the small operator force bump of 3 N. However, this force is too small and short in time to be felt by the operator and does not result into a sticking effect.

The second test aimed to evaluate the tracking performance for the velocity command. A test was conducted for each mode, namely, a vertical motion for the unilateral mode and a vertical displacement on the rigid aluminium surface for the bilateral mode, as depicted in Fig. 3.4. With these two tests, it was thus possible to compare the system's behaviour depending on the interaction. The tracking results are presented in Fig. 3.6. An interesting feature for the

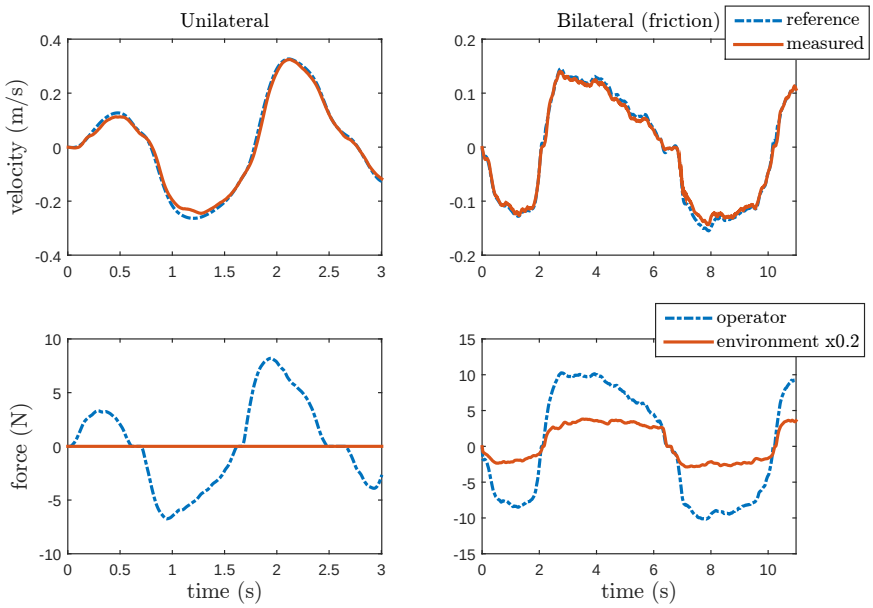

FIGURE 3.6 – Results of the velocity tracking test for the unilateral vertical motion (on the left) and for the bilateral vertical displacement on a rigid surface (on the right). The environment force is divided by 5 in order to obtain a visual comparison based on the applied operator force.

vertical displacement during the bilateral amplification — static 100 N environment force in the horizontal direction — is the presence of friction. Indeed, the friction force, which is proportional to the normal force applied on the environment, has to be overcome before generating an actual velocity command. In the test depicted in Fig. 3.6, the friction force is around 15 N. The operator thus needs to apply a force greater than 3 N to initiate the motion due to the amplification ratio of 5. Thereby, the resulting velocity command is based on the difference between the friction force and the operator force. The admittance parameters are therefore adjusted according to the bilateral control law (gain scheduling) and dictate the motion's dynamics. This approach leads to a highly responsive and stable interaction. In both cases, the unilateral and bilateral modes, the tracking performance between the measured and reference velocities are excellent. However, the unilateral motion is smoother, because of the high virtual inertia that has a greater impact on the filtering of the input force. The velocity command is also slightly delayed with the input force, while the bilateral velocity command rather coincides. This dynamics is desired for the unilateral mode and leads to the most intuitive interaction.

The last test aimed to assess the effect of the continuous gain scheduling law. A vertical displacement task with a horizontal bilateral amplification, as demonstrated in Fig. 3.4, was performed with and without the gain scheduling. The amplification factors are similar to those used in the previous experiments, i.e., the values reported in Table 3.1. The parameters for the gain scheduling case are also similar, but the admittance parameters for the constant case

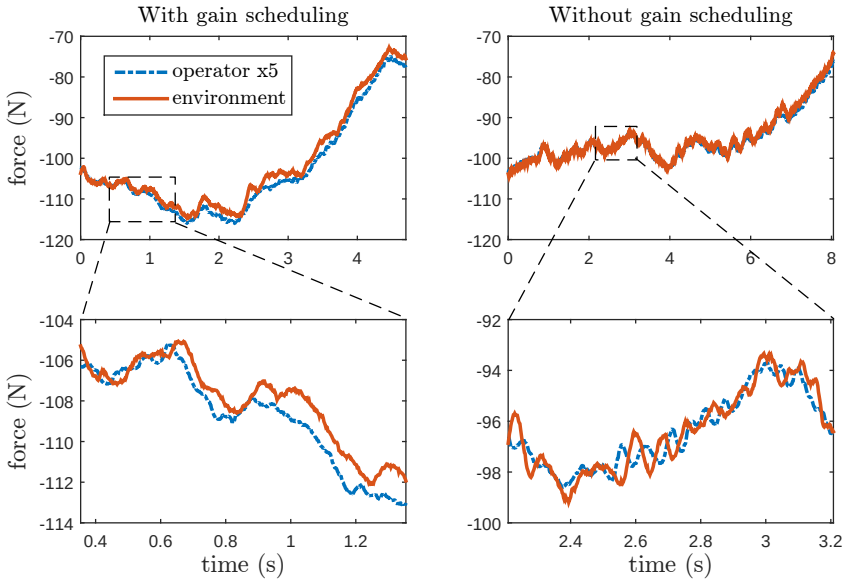

FIGURE 3.7 – Results of the force tracking for the horizontal amplification during the vertical displacement with gain scheduling (on the left) and with static parameter values (on the right). The operator force is multiplied by 5 in order to provide a better visualization of the tracking quality.

are set to $c_v = 0.12$ Ns/m and $m_v = 30$ kg. The results for a sample of the displacement are shown in Fig. 3.7. The amplification with constant parameters has in average a better tracking than the gain scheduling amplification. However, the gain scheduling interaction is definitively smoother than the one with constant parameters which, on the other hand, can be unstable for high impulses. It is also important to notice that the maximum error for the gain scheduling tracking in the cropped window of Fig. 3.7 is 1 N and reaches a maximum peak of 3 N for the full displacement. This peak error is small and demonstrates that the optimal gain scheduling law is not just leading to a high performance system but also to a robustly stable system.

In short, these three tests have demonstrated the potential to use admittance regulators for unilateral and bilateral interactions, even in the presence of a rigid environment.

3.7 Video Demonstration

The accompanying video demonstrates all situations to be addressed by the controller, namely, unilateral interaction, bilateral amplification and transition between both modes (*Chap3_Kuka_Uni_and_Bilateral.mp4*). The video also illustrates the stability and effectiveness of the gain scheduling control law using different configurations of the Kuka LWR 4 during bilateral interactions. Moreover, the force amplification is illustrated visually using the

displacement of a heavy payload. An example of a pHRI insertion task is also provided in the video. The video is available at

http://robot.gmc.ulaval.ca/publications/these-de-doctorat

3.8 Conclusion

In this chapter, a control architecture with variable admittance regulators for physical human-robot interaction was presented. The specific control laws detailed in this work adjust automatically to the interaction mode, namely, unilateral, transition, and bilateral, in order to provide the most intuitive and efficient interaction. Indeed, the unilateral variable control law aims at providing comfort and precision for the operator, while the bilateral gain scheduling is focused on stability and performance for the amplification, and whereas the transition control law ensures a smooth imperceptible transition from one mode to the other. The Kuka LWR 4 was used to demonstrate the effectiveness of the control architecture using three different experiments. A video extension of the chapter shows the intuitiveness of the resulting interaction. In conclusion, the use of a single controller structure such as the admittance controller is therefore viable for a highly effective and versatile pHRI. Future work includes the development of additional safety features since a human force enhancement device can be dangerous if not used properly.

Chapitre 4

uMan : A Low-Impedance Manipulator for Human-Robot Cooperation Based on Underactuated Redundancy

Résumé

Cet article revisite le concept de manipulateur sous-actionné afin d'améliorer significativement la coopération physique humain-robot (pHRI) pour l'industrie de l'assemblage. Le but principal, ici, est d'atteindre une manipulation fine qui soit intuitive et nécessitant un minimum d'effort peu importe le poids et la forme de la charge utile. Un manipulateur sous-actionné — dénommé uMan — basé sur une architecture macro-mini est donc conçu avec un nouveau mini mécanisme passif. Ce nouveau mini mécanisme passif a pour but de minimiser l'impédance effective, éliminer l'impédance non linéaire et découpler la dynamique de l'humain et la dynamique du robot. Une stratégie de commande est développée spécifiquement afin d'atteindre ces objectifs tout en considérant la nature sous-actionnée du robot pour la coopération et l'assistance autonome. Des validations expérimentales sont présentées et incluent une tâche d'insertion de goujon (peg-in-hole task) afin d'évaluer la facilité à produire des manipulations fines, une tâche de détection de collision afin de démontrer la sécurité du système et des tâches d'assemblage réelles afin d'établir la viabilité du concept en industrie.

4.1 Introduction

Humans are still essential to many industrial applications, because of their ability to intuitively adjust their interaction impedance depending on the task to be performed. However, certain tasks can be uncomfortable and exhausting while requiring human-fine manipulation capability.

This issue has motivated the emergence of different concepts of human-friendly robotic manipulators (Tadele et al. [2014]), notably, in the field of physical human-robot interactions (pHRI) (Krüger et al. [2009], Cherubini et al. [2016]). While these pHRI manipulators should alleviate the physical constraints on humans, they should as well increase fine manipulation performance.

In order to ensure effective fine manipulations, the main feature sought for intuitive pHRI manipulators is to perfectly match the human varying interaction impedance. This implies two specific criteria that a cooperative robot should follow, namely, *i*) minimizing the impedance and *ii*) eliminating the nonlinear impedance. Achieving these two fundamental objectives enables the human operator to deploy his/her own impedance, which naturally adapts to handling or assembly tasks. Due to the resulting low impedance, another important benefit of this fine manipulation objective is the increased safety during autonomous motion of the robot.

The prevalent approach to apparent impedance reduction in pHRI is the use of a force sensor in order to sense and regulate the operator's physical interaction. Using this force input, the actuated manipulator is thereby able to emulate different impedances. Such a technique is usually combined with an admittance controller (van der Linde and Lammertse [2003], Lecours et al. [2012]), a PI controller (Newman and Zhang [1994]), or even lead and lag compensators (Buerger and Hogan [2007]). However, it has been shown that the hardware dynamics limits the apparent impedance reduction (Hogan [1988]) and that any attempt to go below a certain fraction of the intrinsic inertia leads to unstable behaviours (Colgate and Hogan [1989]). Recent studies demonstrated that reduction ratios of 5 to 7 times the intrinsic inertia were feasible (van der Linde and Lammertse [2003], Buerger and Hogan [2007], Lecours et al. [2012]). Other approaches making use of force sensors include the appending of compliant material in order to mechanically filter the high-frequency interactions (Lamy et al. [2009]). Nevertheless, these large inertia reduction ratios are achievable only by overstepping the concept of passivity (Colgate and Hogan [1988], Colgate [1994]), which means that physical contacts are limited to specific ranges of environment dynamics.

In an industrial assembly context, where pHRI faces a broad range of environment dynamics, it is important to ensure passivity at all times as well as a fine and intuitive manipulation. Luckily, a common set of applications exist where the operational degrees of freedom (dof) can be permanently assigned to one of two spaces, namely the manipulative space and the constrained space. In the manipulative space, all the work — except for the gravity compensation forces — is performed by the human being, while in the constrained space, all the work is performed by the robot. Therefore, only the manipulative space needs to render the lowest possible impedance. Typical examples of such assembly applications are the ones involving lift assist devices. In fact, the most adequate solution is a collaborative manipulator using underactuated redundancy, which can passively provide a lower apparent impedance

than any actuated mechanism. Some mechanisms, such as cable-suspended intelligent assist devices (Wen et al. [2001], Campeau-Lecours et al. [2016]), already attempted to make use of this principle. Unfortunately, the handling of off-centred payloads and the ability to constrain rotational degrees of freedom are not possible with such cable-suspended devices.

It is thus proposed here to extend the principle of macro-mini manipulator using underactuated redundancy, presented in Labrecque et al. [2016], in order to provide intuitive and safe interaction yielding to very natural fine manipulation capabilities over a virtually unlimited workspace. This macro-mini concept includes high-impedance active (HIA) joints and low-impedance passive (LIP) joints, which have decoupled dynamics due to the mechanical redundancy. The HIA joints constitute the macro component — which is the portion attached to the fixed base — and are located outside of the human operator's workspace. The LIP joints constitute the mini component — which is the portion close to the end-effector — and are thus located in the manipulative space. Therefore, the HIA joints provide the payload handling capability by cancelling the forces applied by the human operator on the LIP joints, which leads to a low-impedance interaction.

The main contributions of this chapter to the field of pHRI are :
- A new design approach using a modified Chebyshev mechanism in order to increase the effective pendulum length for the horizontal LIP joints, while reducing their structural envelope size and weight as well as restraining all rotations.
- A two-mode statically balanced vertical motion using an extended compact version of the Sarrus mechanism.
- A unified control law that can transit between the autonomous and cooperative modes almost seamlessly due to the similar cooperative parameters for both modes.
- The introduction of a filtered parameter in the control law which improves the intuitiveness of the interaction.
- A novel collision detection that is specifically designed for this type of architecture and that considerably increases pHRI safety.

This chapter is structured as follows. Section 4.2 presents the mechanical architecture of the macro-mini underactuated manipulator (referred to as uMan) with an emphasis on the LIP joints and their advantages over other passive designs. Section 4.3 describes the control strategies and their implication for the cooperative mode and the autonomous mode as well as the highly efficient collision detection. Section 4.4 discusses the different experiments performed in order to validate the viability of the underactuacted manipulator in an industrial context. Finally, conclusions are drawn in the last section.

4.2 Active-Passive Mechanism

As mentioned above, an advanced assistive device using an active macro manipulator and a novel passive mini manipulator is presented in this chapter. From the previous work presented in Labrecque et al. [2016], it has been demonstrated that the passive mini manipulator must be capable of handling significant payloads, that the macro-mini mechanism should allow translations but constrain rotations, and that the end-effector should require minimal forces to be moved by the operator, i.e., low impedance, but should passively return to its central reference configuration when no external force is applied. These objectives have thus driven the design of the new mini mechanism in addition to the new objectives which are : the extension to a 3-dof mechanism and the reduction of its total weight and size. It is noted that the extension to a 3-dof mechanism is not trivial since the added dof corresponds to the vertical translation, which must support the weight of the payload. A number of concepts have thus been investigated for their suitability to act as passive mini mechanisms and the main results of this investigation are reported in this section.

4.2.1 Passive horizontal motion

A first possible strategy for the structure of the mini is the use of three linear rails orthogonally stacked in series, including vertical motion. Industrial rails can support large payloads and are relatively compact. Unlike the passive manipulator presented in Irino et al. [2013], here, springs are required in order to passively return the mechanism to its central position. Unfortunately, friction in the linear rails increases significantly with offset payloads. Because of this friction, the return force must be significant which yields a large deadband at the central position. As a result, the interaction is neither intuitive nor comfortable for the user.

A second strategy is to use parallelograms for the two horizontal degrees of freedom. The use of parallelograms considerably reduces friction — due to the use of revolute joints instead of rails — and makes it possible to use gravity to passively returning the mechanism to its central position due to the inherent pendulum motion. Parallelogram four-bar mechanisms also maintain the orientation of the end-effector and allow off-centred payloads. This approach is compared with the state-of-the-art admittance control in Labrecque et al. [2016] and is shown to lead to significant effective impedance reduction at the end-effector (for more details, see Section 4.7.2). However, parallelogram mechanisms also have drawbacks such as the vertical parasitic motion and the magnitude of the return force that increases with the weight of the payload. Indeed, when the coupler link of a parallelogram mounted in a vertical plane is moved horizontally, a vertical parasitic motion is induced, which means that the payload is moved up, thereby requiring a significant force — proportional to the weight of the payload — from the human user. One way to reduce this effect is to increase the length of the equivalent pendulum, but unfortunately this leads to an increase of the parallelogram's link lengths which then results in a bulky mechanism.

An alternative strategy, in order to increase the effective length of the pendulum motion and obtain a more compact mechanism with reduced weight and size, is to use straight-line mechanisms based on revolute joints. Straight-line mechanisms produce a straight-line (or an approximate straight-line) motion of a specific point on one of the links of their coupler over a given range of motion of the joints. By slightly modifying the geometry of such mechanisms, motion trajectories with a large radius of curvature can be obtained with relatively short links, thereby allowing gravity to return the mechanism to its central configuration, without requiring large forces from the human operator. Several straight-line mechanisms can be found in the literature (Chironis [1991]), but the four-bar Chebyshev mechanism (Chironis [1991]) is selected in this work due to its inherent structural robustness.

The Chebyshev mechanism is therefore modified in order to obtain a radius of curvature three times larger than the length of the crank links, as depicted in Fig. 4.1 which significantly reduces the vertical parasitic motion and thereby the effective impedance. Furthermore, in order to constrain the rotation around an axis normal to the plane of the mechanism, two four-bar mechanisms are mounted in parallel between the base and the end-effector. The resulting modified double Chebyshev mechanism, referred to as Large Radius Chebyshev Parallelogram (LRCP), is shown in Fig. 4.2. In practice two parallel mechanisms mounted in parallel planes are linked together by structural bars in order to withstand the moments along the other axes as illustrated in Fig. 4.3 for the two horizontal motions.

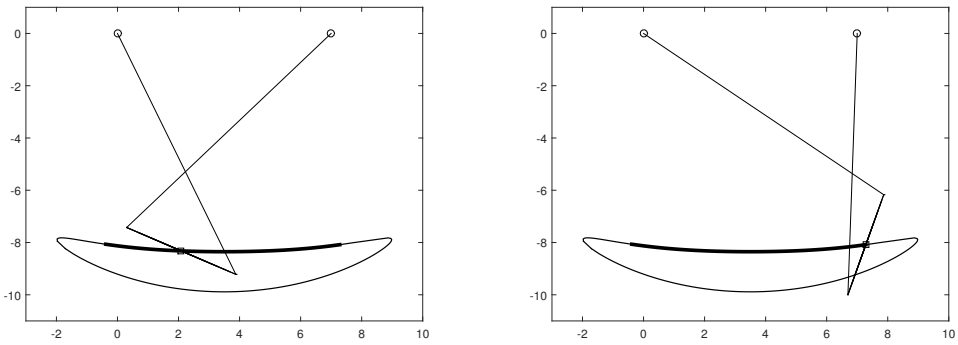

FIGURE 4.1 – Two configurations of a modified Chebyshev mechanism with the path traced by the centre of the coupler. The upper portion of the path approximately describes a circular arc with a large radius of curvature. The bold section of the coupler curve corresponds to the range of motion that can be used in practice.

4.2.2 Passive vertical motion

The concept used for the horizontal LIP joints, namely the LRCP, cannot be directly applied to a vertical motion since gravitational forces tend to pull the mechanism downwards, eliminating the possibility for the mini mechanism to have a bidirectional range of motion. A different concept is therefore developed for the vertical motion of the mini mechanism.

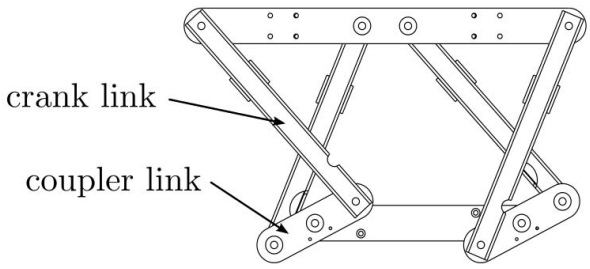

FIGURE 4.2 – Large Radius Chebyshev Parallelogram, comprising two modified straight-line Chebyshev mechanisms connected by a coupler link.

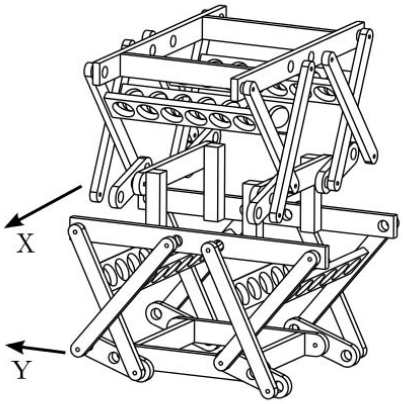

FIGURE 4.3 – CAD model of the LRCP mechanisms producing pendulum-type parallelogram motions in both horizontal directions, with a large radius of curvature.

In order to obtain a behaviour similar to that described above for the horizontal motion, it is required to have the minimum potential energy in the desired centre of the mechanism's range of motion. In other words, the dynamics of gravitational forces acting on a pendulum must be reproduced but for a vertical motion. With a careful design using the potential energy stored in a spring one can counterbalance the variation of gravitational potential energy while the system moves, thereby creating a virtual pendulum dynamics. In order to produce an effective human-robot interaction, such a design should be capable of performing a pure translation using only rotational joints and be capable of withstanding moments. The concept of the Sarrus linkage (Hunt [1967]), shown in Fig. 4.4, is therefore used for the design of the new vertical LIP joint.

An extension spring is attached from the base to the first link, as depicted in the complete mechanism shown in Fig. 4.5. The spring is selected in order to optimize the range of motion of a specific payload's weight, i.e., having the minimum potential energy in the centre of the proposed Sarrus mechanism's range of motion. However, in a practical application, the mechanism should be able to operate in two modes, namely loaded and unloaded, which

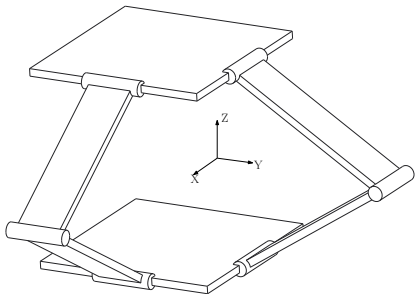

FIGURE 4.4 – Sarrus linkage : two orthogonal sets of three revolute joints with parallel axes are connecting two moving bodies, thereby producing a constraint equivalent to a prismatic joint between these bodies.

thereby requires two different static balancing systems. When the device is loaded (Fig. 4.2.2), the payload and the mechanism are balanced by the extension spring, with the equilibrium position in the centre of the vertical range of motion, thereby allowing intuitive manipulation of the payload by the human user. On the other hand, when no payload is attached to the mini mechanism (unloaded state, Fig. 4.2.2) the end-effector of the Sarrus linkage moves up — due to the effect of the extension spring — and presses against a mechanical stopper. This stopper is coupled with a compression spring (shown in Fig. 4.5) and allows the operator to interact with the end-effector of the unloaded device, within a small range of vertical motion. It is recalled that the main objective of the uMan robot is to assist the user with the payload manipulation, for which low impedance interaction is provided including in the vertical direction, based on the gravity compensation system described above. When the device is unloaded, the compression spring provides interaction capabilities, although with higher impedance and smaller range of motion. This is not critical for typical industrial applications because the unloaded state is mainly used to teach the robot where to pick-up and drop the payloads, which should be needed only sporadically. The compression spring also acts as a safety switch when the unloaded robot is moving autonomously.

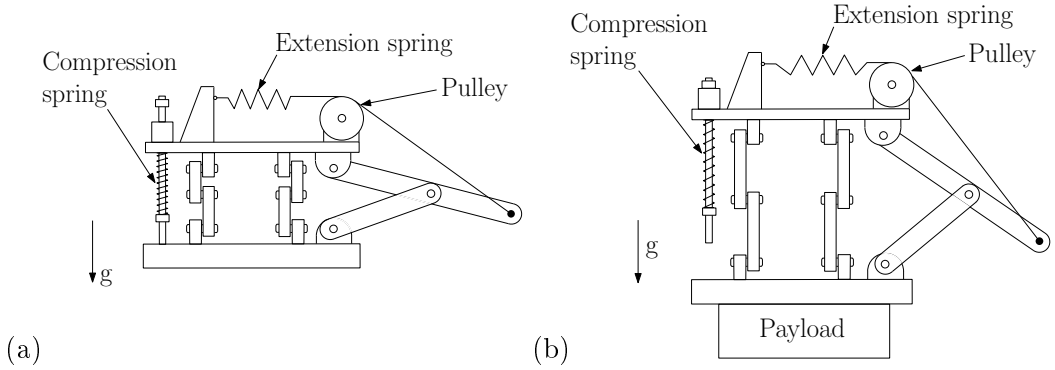

FIGURE 4.5 – The two states of the Sarrus mechanism. (a) Unloaded state (b) Loaded state.

4.2.3 Active macro manipulator

The active macro manipulator used in this work is a gantry robot that provides the three translational degrees of freedom over a large workspace. This component of the manipulator was designed for large payloads and has an equivalent moving mass of 500 kg in the x-direction and of 350 kg in the y-direction. Its architecture is described in detail in Gosselin et al. [2013]. Here, the suspended bridge architecture is also favoured because of its prevalence in the assembly industry. The prototype of the macro-mini uMan is shown in Fig. 4.6.

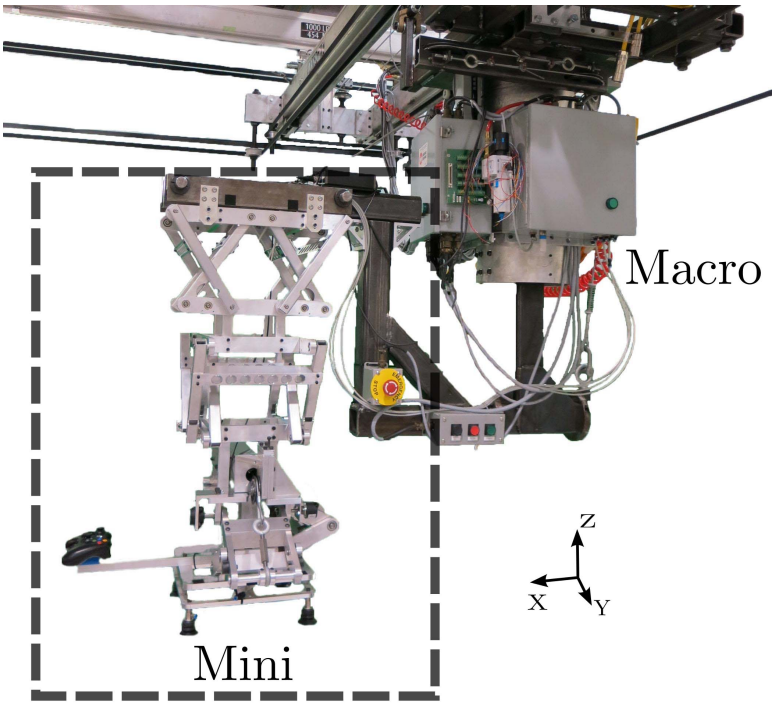

FIGURE 4.6 – Macro-mini uMan. Macro : 3-dof gantry manipulator. Mini : 3-dof passive mechanism.

4.3 Control of the active-passive mechanism

If the macro-mini manipulator described in Section 4.2 is designed properly following the system's requirements, then the necessary controller can be rather simple. Indeed, the resulting dynamics is equivalent to that of a moving cart with a suspended pendulum. However, the main objective of the uMan is to provide an intuitive and safe interaction between the operator and the robot. Therefore, besides the addition of a safe autonomous mode, the controller has to accommodate certain comfort aspects such as a reduction of the impedance felt by the operator, a reduction of the required force to maintain its velocity, and a quick and intuitive reaction to unexpected contacts. These specific physical human-robot interaction (pHRI) aspects are considered in the novel control law which thereby includes additional functionalities such as a unique control law for both modes, namely autonomous and cooperative, a new intui-

tive filtered parameter, and a highly efficient collision detection. The controller comprises two main control loops, namely the inner control loop for the motor input and the outer control loop for the external input. Both control loops are described in detail in the next subsections.

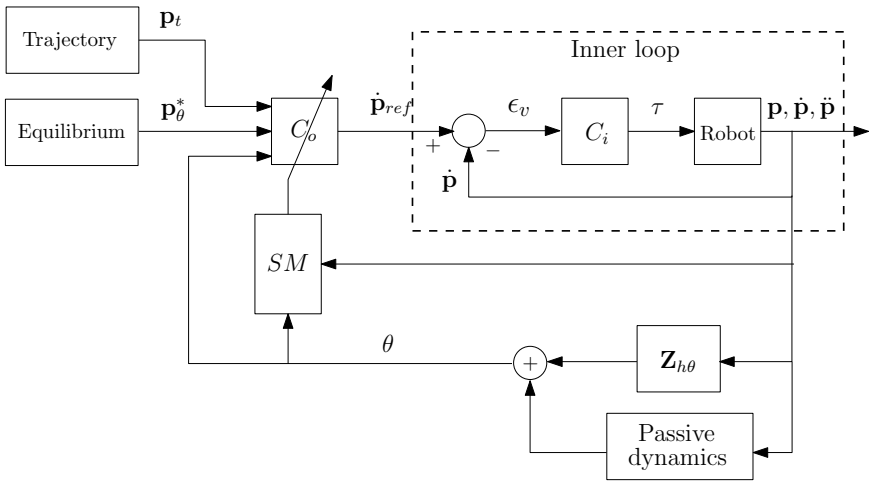

FIGURE 4.7 – Control architecture for the active-passive uMan.

4.3.1 Inner control loop

The internal control, C_i, is performed at the macro manipulator's joint level with a proportional velocity regulation. A compensation of the dry friction, $\boldsymbol{\tau}_f$, is also added at the torque level in order to reduce the mechanical delay, leading to

$$\boldsymbol{\tau} = \mathbf{K}_p \boldsymbol{\epsilon}_v + \boldsymbol{\tau}_f \tag{4.1}$$

where $\boldsymbol{\tau}$ is the array of input torque for the macro manipulator's actuators, $\mathbf{K}_p$ is the diagonal proportional gain matrix and $\boldsymbol{\epsilon}_v = (\dot{\mathbf{p}}_{ref} - \dot{\mathbf{p}})$ is the array of velocity error as depicted in Fig. 4.7.

The nature of the interaction, i.e., a human user and a passive compliance at the end-effector, allows the use of such a simple inner control loop. However, if a high positioning accuracy is required when the robot is operating in autonomous mode, an inverse dynamics control with a position regulation could be more appropriate.

4.3.2 Outer control loop

The global control is performed in the end-effector's Cartesian space and includes a general controller with specific parameters depending on the operation mode. As mentioned above, the two main modes of operation are the autonomous mode and the cooperative mode. For each of these modes, the cases with and without payload are included. A state machine, represented

by the *SM* block in Fig. 4.7, enables the mode switch according to the current and desired state of the manipulator. Moreover, a vector representing the position of a reference point on the end-effector of the mini manipulator with respect to a reference point on the end-effector of the macro manipulator is defined as $\mathbf{p}_\theta$, which is a function of the (passive) joint coordinates of the LIP joints of the mini manipulator. Also, the array of LIP joint coordinates is defined as

$$\boldsymbol{\theta} = \begin{bmatrix} \theta_x & \theta_y & \theta_z \end{bmatrix}^T$$

where θ_x, θ_y and θ_z are respectively associated with the X, Y and Z passive mechanisms described in the preceding section. It is important to mention that for both the autonomous and the cooperative mode, the joint coordinates of the LIP joints — and therefore the components of vector $\mathbf{p}_\theta$ —, include the LIP joint displacements resulting from the human interaction and the LIP joint displacements resulting from the motion of the macro manipulator, which are respectively depicted by the $\mathbf{Z}_{h\theta}$ and *Passive dynamics* blocks in Fig. 4.7.

The main contribution of the outer loop control developed in this work is that it takes into account all inputs (human, environment, and desired trajectory) at all times. Indeed, the architecture of the controller remains unchanged regardless of the operation mode. However, parameters such as the gains can be modified in order to obtain a better performance or to cancel a certain input. The equation of the general controller, C_o, is as follows :

$$\begin{aligned} \dot{\mathbf{p}}_{ref} = \quad & \mathbf{K}_{Pt}\mathbf{e}_t + \mathbf{K}_{P\theta}\mathbf{e}_\theta + \mathbf{K}_D\dot{\mathbf{e}}_\theta + \mathbf{K}_F\mathbf{e}_f \\ & + \mathbf{K}_{NL}\mathbf{f}_{NL} \end{aligned} \tag{4.2}$$

where $\dot{\mathbf{p}}_{ref}$ is the commanded position vector of the end-effector of the macro manipulator fed to the inner controller described above, as shown in Fig. 4.7. Each of the terms of equation (4.2) favours a certain behaviour of the uMan system. They are described as follows :

• $\mathbf{K}_{Pt}\mathbf{e}_t$:
The gain matrix $\mathbf{K}_{Pt}$ comprises the proportional gains that ensure that the desired trajectory is followed by the macro manipulator's end-effector (the macro-mini attachment point) whose position with respect to the fixed frame is noted $\mathbf{p}$. The error vector $\mathbf{e}_t = (\mathbf{p}_t - \mathbf{p})$ therefore includes the error between the desired macro manipulator position vector $\mathbf{p}_t$ and its actual position vector $\mathbf{p}$.

• $\mathbf{K}_{P\theta}\mathbf{e}_\theta$:
The gain matrix $\mathbf{K}_{P\theta}$ comprises the proportional gains related to the displacements of the LIP joints relative to their equilibrium configuration. The error vector $\mathbf{e}_\theta = (\mathbf{p}^*_\theta - \mathbf{p}_\theta)$ therefore represents the error between the position of the end-effector of the mini manipulator relative to the end-effector of the macro manipulator corresponding to the equilibrium configuration,

noted $\mathbf{p}_\theta^*$ and the actual position vector of the end-effector of the mini manipulator relative to the macro manipulator, $\mathbf{p}_\theta$. As described in Section 4.2, the motion of each of the passive modules of the mini manipulator can be described as an equivalent pendulum motion, which yields

$$\mathbf{p}_\theta = \begin{bmatrix} l_x \sin\theta_x & l_y \sin\theta_y & l_z \sin\theta_z \end{bmatrix}^T$$

where l_x, l_y, and l_z are the effective radii of curvature of each LIP joint and θ_x, θ_y, and θ_z are the equivalent angles of each LIP joint [1]. The equivalent LIP joint angles θ_x, θ_y, and θ_z are equal to zero when the LIP mechanisms are at their equilibrium configuration. Therefore, in order to maintain the manipulator still when it reaches its equilibrium configuration, the components of $\mathbf{p}_\theta^*$ are also equal to zero. For small angles, the relationship becomes quasi-linear, i.e., $\sin\theta \simeq \theta$, thereby ensuring an immediate response to small displacements of the end-effector which is required for fine manipulation.

• $\mathbf{K}_D\dot{\mathbf{e}}_\theta$:

The gain matrix $\mathbf{K}_D$ comprises the derivative gains related to the velocity of the end-effector of the mini manipulator relative to the velocity of the end-effector of the macro manipulator. The error vector $\dot{\mathbf{e}}_\theta = (\dot{\mathbf{p}}_\theta^* - \dot{\mathbf{p}}_\theta)$ therefore includes the velocity of the end-effector of the mini manipulator relative to the macro manipulator, noted $\dot{\mathbf{p}}_\theta$, and the desired value of this velocity vector, noted $\dot{\mathbf{p}}_\theta^*$, which is equal to zero. This term mainly reduces the oscillations around the equilibrium configuration of the mini manipulator.

• $\mathbf{K}_F\mathbf{e}_f$:

The gain matrix $\mathbf{K}_F$ comprises the gains associated with the filtered (low-pass) error vector $\mathbf{e}_\theta$ applied to the relative displacement of the mini manipulator with respect to the macro manipulator. This term stably increases the controller DC gain and adds virtual inertia and damping to the response. It makes the interaction more intuitive and comfortable for the operator when a high-force input is performed, which is directly related to a large LIP joint displacement due to the effect of gravity, such as a push-away motion. This virtual dynamics is not felt when an interaction or a sharp change of direction is initiated because of the gain vector $\mathbf{K}_{P\theta}$. Depending on the dynamics of the LIP joints (radius of curvature, weight, friction) this term might not be necessary.

• $\mathbf{K}_{NL}\mathbf{f}_{NL}$:

The gain matrix $\mathbf{K}_{NL}$ comprises the gains that regulate the effect that the nonlinear functions $\mathbf{f}_{NL}$ have on the reference velocity $\dot{\mathbf{p}}_{ref}$. This nonlinear function should generate relatively larger response when the end-effector is near its physical boundaries in order to avoid any

1. The vertical parasitic motions induced by the horizontal motions (x and y) are not considered in the evaluation of the vertical z-motion (Sarrus mechanism) since they can be shown to be negligible.

contact with mechanical limits and to counter the effect of gravity. For the uMan, in order to alleviate the partial payload that the human operator has to haul, the nonlinear functions for the horizontal LIP joints are related to the parasitic vertical motion of the pendulums such that

$$f_{NL}(\theta_x) = sign(e_{\theta x})\frac{x_{\theta z}}{x_{\theta znorm}}, \tag{4.3}$$

$$f_{NL}(\theta_y) = sign(e_{\theta y})\frac{y_{\theta z}}{y_{\theta znorm}}, \tag{4.4}$$

with

$$x_{\theta z} = l_x[1-\cos\theta_x], \tag{4.5}$$

$$y_{\theta z} = l_y[1-\cos\theta_y], \tag{4.6}$$

where $e_{\theta x}$ and $e_{\theta y}$ are the horizontal components of $\mathbf{e}_\theta$, and $x_{\theta znorm}$ and $y_{\theta znorm}$ are the heights at which it is desired to obtain $f_{NL}(\theta) = 1\ m/s$. It is recalled that the equivalent LIP joint angles θ_x and θ_y are equal to zero when the LIP mechanisms are at their equilibrium configuration. The effect of this nonlinear function (red dashed line) on the reference velocity is illustrated in Fig. 4.8. The linear function (blue dashed-dotted line) represents a component of the function $\mathbf{K}_{P\theta}(\mathbf{e}_\theta)$ — linear for small angles — and the combination of both corresponds to the black solid line. Larger angles are thus more penalized and thereby generate relatively larger responses. For the Sarrus mechanism, it was found that the nonlinear function is optional since

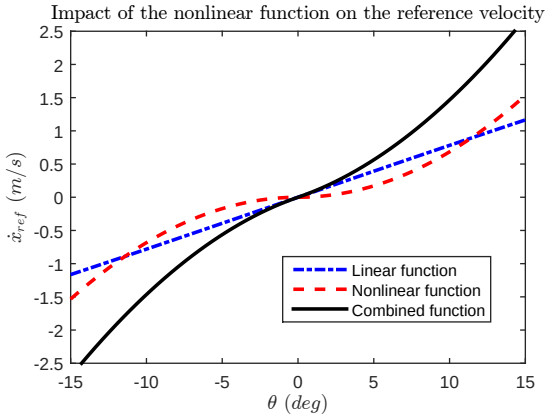

FIGURE 4.8 – The effect of adding a nonlinear function to the linear reference velocity output.

there is no pendulum effect and since the passive range of motion is large enough to prevent ever reaching the physical limits when loaded. Nevertheless, a nonlinear function should be added to the outer control law when the passive range of motion is small.

4.3.3 Stability analysis

Before implementing the control law it is important to assess the behaviour of each of the interaction parameters as well as their limit. Using a theoretical model, it is possible to obtain

a first estimate of the stable interval for the gain values $\mathbf{K}_P$, $\mathbf{K}_D$, $\mathbf{K}_F$, and $\mathbf{K}_{NL}$. A general guideline for the manual implementation and intuitiveness assessment is also deduced from this analysis. The dynamics of the end-effector for a single dof is based on the following pendulum equation, namely,

$$ml\ddot{\theta} = F\cos\theta - mg\sin\theta - m\ddot{p}\cos\theta \tag{4.7}$$

where m is the payload value including the weight of the suspended part of the mini mechanism, F is the horizontal human input force, g is the gravitational acceleration, and $\ddot{p}$ is the macro robot acceleration.

From the dynamic equation (4.7) and the control law (4.2), a simulation is designed in order to represent the behaviour of the end-effector in the x-direction. The speed of the macro robot is limited to 1 m/s, the pendulum weight, m, is equal to 30 kg, and its effective length is equal to 0.6 m. The macro manipulator motion is also delayed by 0.15 second which is deduced from the real macro manipulator dynamics. This simulation provides a clear methodology for the evaluation of the highest stable gains for all parameters. More specifically, it was found that the gains have to be tuned in the following order : $\mathbf{K}_P$, $\mathbf{K}_{NL}$, $\mathbf{K}_D$, and then $\mathbf{K}_F$. The approach is defined as follows :
i) K_P, which yields a quick and immediate response, is first tuned to the highest stable gain with small damped oscillations,
ii) K_{NL}, which generates larger responses for larger mini displacements, is then tuned following the same criterion,
iii) K_D, which reduces the oscillations around the mini manipulator's rest position, is tuned to damp as much as possible the small oscillations,
iv) K_F, which stably increases the controller DC gain and introduces small virtual inertia and damping for push-away motion, is tuned to a stable gain that does not significantly slow down the settling time.

The stable boundaries found for each of the gains are : $K_P = [1.5;\ 7.5]$, $K_{NL} = [0;\ 0.6]$, $K_D = [0;\ 0.85]$, and $K_F = [0;\ 35]$. A simulation example of the resulting stable controller including the four cooperative gains is depicted in Fig. 4.9. Moreover, an unstable high gain response corresponding to each of the steps of the tuning procedure is illustrated in order to demonstrate that the final control law, in addition to being stable, has the highest DC gain response. It is important to note that these values are computed with a theoretical model and have to be adjusted afterwards with the real macro-mini manipulator using the same procedure.

4.3.4 Cooperative mode

When the cooperative mode is enabled, it is necessary to prescribe the positions of the macro manipulator as the desired trajectory position inputs $\mathbf{p}_t$ in order to obtain a pure pHRI. It is also possible to set the components of $\mathbf{K}_{Pt}$ equal to zero for redundancy purposes. With

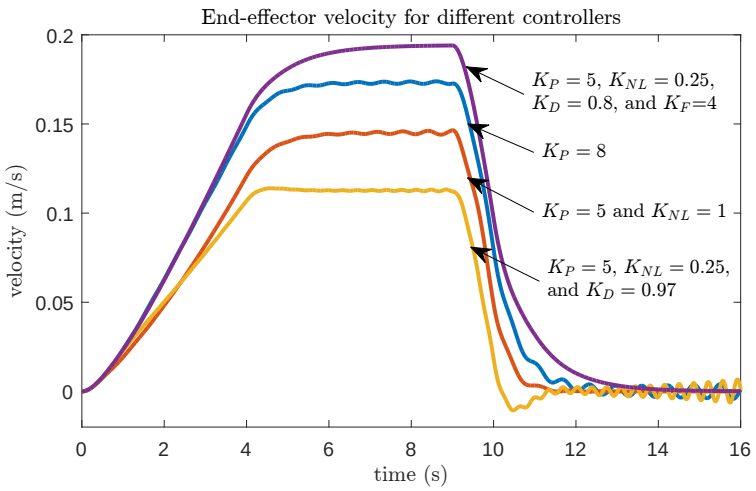

FIGURE 4.9 – Three unstable responses with partial control laws and high gain values, and a stable response with the proposed control law and adequate gain values. The input is a horizontal force on the end-effector going from 0 N to 10 N in 4 seconds followed by a constant 10 N input for 5 seconds which then ends by a force release to 0 N in 1 second.

this approach, the only input is then the LIP joint angles, i.e., the human and environment interactions. The equilibrium positions $\mathbf{p}_\theta^*$, $x_{\theta z}^*$, and $y_{\theta z}^*$ in cooperative mode for each LIP joint are acquired when the system is initialized and the mechanism is stationary. The same control parameter values are used when the uMan is loaded, apart from the equilibrium position z_θ^* for the vertical LIP joint (Sarrus mechanism) which is predefined depending on the payload to be handled. This procedure is necessary in order to take into account both states, namely the loaded and unloaded states.

4.3.5 Autonomous mode

When the autonomous mode is enabled, the desired trajectory position vector $\mathbf{p}_t$ is defined by the assisted trajectory generation and the components of $\mathbf{K}_{Pt} \neq 0$. The optimal approach to use this unique controller is to maintain the other terms active in the control law — which depend on the LIP joint angles — in order to stabilize the uMan as well as to react to external contacts. It is also advisable to keep the control parameter values used for the cooperative mode. Using this approach, the mode switch (autonomous to cooperative) for a physical human intervention — which is described in the next subsection — is smoother. However, this approach is only feasible if the autonomous trajectory does not produce high jerks. Indeed, high-frequency variations in the acceleration favour large oscillations of the LIP joints and thereby reduce the positioning accuracy and can even eventually trigger the collision detection. In a case where the planned trajectory generates high jerks, an easy solution would be to reduce all the parameter gains used for the autonomous mode such that $\mathbf{K}_{Pt}$ could be smaller. This approach can still lead to a precise positioning but slightly deteriorates the collision switching

smoothness, namely the switch from autonomous to cooperative. This mode switching issue thus justifies the development of an effective means of generating low jerk trajectories in order to fully exploit the potential of the underactuacted redundant manipulator.

4.3.6 Trajectory generation

In a context of pHRI, it is expected to have an adaptable autonomous trajectory motion. Indeed, it should be easy to program the desired trajectory, as well as the task to be performed, depending on the environment, and to be able to physically interrupt the robot motion at any time. Therefore, an effective trajectory should include many way points and the ability to be automatically replanned. A relevant approach in order to consider these issues is to use cubic splines (Bartels et al. [1987]). The cubic spline has the advantage of being continuous up to the third derivative and to be computationally efficient. On-line recomputing is thereby easier and the jerk, i.e., the time derivative of the acceleration, is thus continuous.

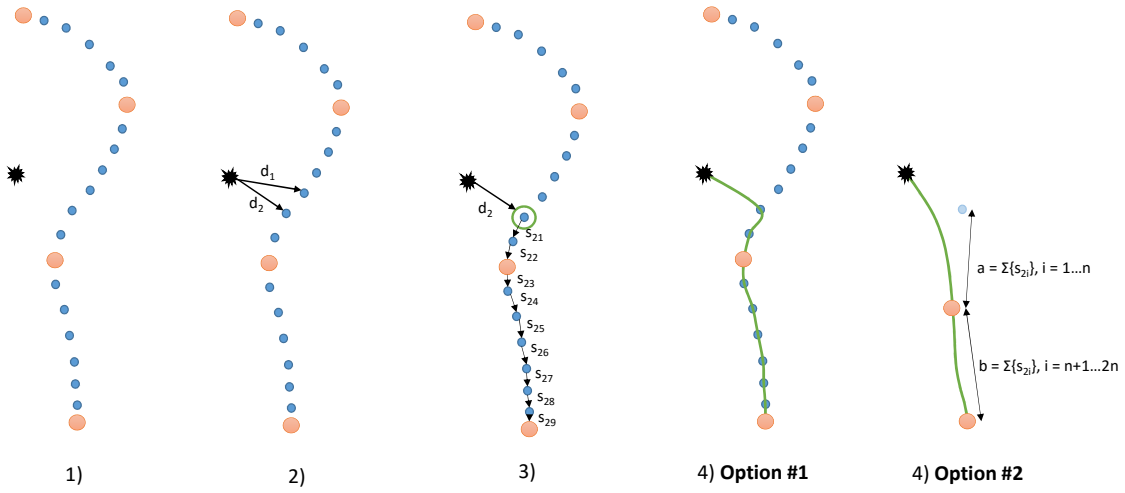

FIGURE 4.10 – Replanning algorithm : Steps to recompute the best trajectory using a cubic spline.

With the help of an intuitive user interface, the operator can physically teach the desired trajectory to the uMan by recording a set of main points. Depending on the total trajectory length, a time duration is associated with each segment between the main points. Then, a trajectory planning algorithm can be used. A simple choice in this case is to use an adapted version of the A^* search algorithm (Hart et al. [1968]) in order to find the optimal set of points to reach the final destination. More specifically, the step-by-step algorithm is illustrated in Fig. 4.10 and described as follows :

1. Compute the entire trajectory from the desired starting position to the final destination

based on a cubic spline using the recorded main points. The resulting spline is composed of a list of way points.

2. Find the two way points that are the closest to the actual robot end-effector position using the Euclidean distance (d_1 and d_2).
3. From these two way points find the closest one relative to the final main point n using the sum of each remaining sub segment s_{xi} (with $\sum_{i=1}^{n} s_{1i}$ and $\sum_{i=1}^{n} s_{2i}$)
4. Compute the new trajectory with a cubic spline
   a) **Option #1** : using the remaining way points.
   b) **Option #2** : using new equidistant main points. These new main points are located on the initial spline but are equidistant from each other as well as from the starting way point. For instance, if there are only two remaining main points the total sum of each remaining sub segment is divided in two and the result redefines the new locations, as shown in Fig. 4.10. Note that the final main point is never relocated.

The first option leads to a more accurate trajectory but generates high jerks and high accelerations when launched close to the initial spline. It thereby requires the control parameter gains to be smaller in autonomous mode. On the other hand, the second option is slightly less accurate but allows more time to accelerate and yields smoother curves reducing the high jerks in the replanning.

4.3.7 Collision detection

In addition to its intuitiveness, one of the most important features of the uMan is its safe behaviour. Indeed, the LIP joints provide a very fast response to contacts but the macro manipulator still has to react accordingly when in autonomous motion. The proposed collision detection which is implemented in the uMan drastically improves the detection time for any disturbances in its planned trajectory and produces a smooth transition to the cooperative mode. Indeed, when a collision is detected, the autonomous parameter gain values transit linearly at a pre-defined rate to the cooperative parameter gain values. If the transition rate is too fast, it generates a large reaction force on the heavy macro manipulator which therefore disengages the joint safety clutches. On the other hand, if the transition rate is too slow the macro manipulator maintains its desired trajectory motion slightly longer which produces a larger angle at the LIP joint and generates a slingshot effect because of the control correction on the angle displacement. For the proposed manipulator and controller, it has been found heuristically in experimentation that a switching rate of 12 Hz is leading to the smoothest transition.

The algorithm that triggers the detection uses the equation of motion of a pendulum suspended to a moving cart, which yields, for a single degree of freedom,

$$0 = \ddot{x}\cos\theta + g\sin\theta + l\ddot{\theta} \tag{4.8}$$

where $\ddot{x}$ is the acceleration of the macro manipulator joint, g is the gravitational acceleration, l is the equivalent radius of curvature of the LIP joint, and θ and $\ddot{\theta}$ are respectively the LIP joint angle and angular acceleration. After linearization and simplification for small angles, the equation yields

$$0 = \ddot{x} + g\theta. \tag{4.9}$$

Considering that (4.9) is a simplification of (4.8) and that some inherent dynamics such as friction might be present, the proper way to use this equation is to transform it into the following inequality,

$$|\ddot{x} + g\theta| < c_{lim} \tag{4.10}$$

where c_{lim} is the threshold to detect a contact with the LIP joint during an autonomous motion. This threshold is determined heuristically and should not trigger false collision detections in the autonomous mode but should be sensitive enough in order to detect light contacts. If the actual acceleration of the macro manipulator $\ddot{x}$ is too noisy, then the desired acceleration $\ddot{x}_t$ can be used but c_{lim} should be adjusted accordingly, i.e, most probably increased.

It is a good practice to add redundancy when considering safety issues. This is why two other collision detection methods are implemented in the prototype. The first one limits the Cartesian acceleration of the LIP joints and the second one limits their displacement, yielding respectively

$$\ddot{\mathbf{p}}_\theta^T \ddot{\mathbf{p}}_\theta < a_{lim}^2 \tag{4.11}$$

$$(\mathbf{p}_\theta^* - \mathbf{p}_\theta)^T (\mathbf{p}_\theta^* - \mathbf{p}_\theta) < p_{lim}^2 \tag{4.12}$$

where a_{lim} and p_{lim} are respectively the thresholds on the acceleration and on the displacement of the mini manipulator with respect to the macro manipulator, which is directly related to the motion of the LIP joints. These methods can be slower to trigger the detection or even ineffective — as depicted in Section 4.4.1 — but they should nonetheless be integrated into the algorithm.

4.4 Experimental validation

Even though the capability of the active-passive architecture to minimize the impedance felt by the operator at the end-effector has been demonstrated in Labrecque et al. [2016], it is still necessary to assess the viability of the uMan regarding safety and effective fine manipulation. Therefore, the collision detection is investigated for safety, a peg-in-hole task is evaluated for fine manipulation, and two different assembly mock-up tasks are performed to quantitatively assess realistic physical human-robot interactions.

The control parameter values used for the uMan prototype presented in Section 4.2 and shown in Fig. 4.6 are given in appendix 4.7.1. The ranges of motion of the HIA and LIP joints are

also presented in appendix 4.7.1. A programmable logical controller (PLC) is used to manage the basic states and safety features of the gantry system such as limit switches and hardware faults. The control law (4.2) and its associated state machine are thereby implemented on top of this PLC using *RT-LAB* and *MATLAB/Simulink*. Only encoders are used as input and feedback sensors for the uMan control. However, two six-axis force/torque sensors can be appended at the end-effector for analysis purposes, depending on the task to be evaluated.

4.4.1 Collision detection validation

The first feature to be evaluated is the collision detection. It is important to implement the technique that will detect a collision as quickly as possible and that produces the smallest impact force. Moreover, it should be assessed in a standard pHRI industrial context by respecting the physical and psychological interaction limits recommended by previous works on the subject. For instance, in order to prevent any psychological trauma, the speed of the robot's end-effector should be limited to 0.6 m/s in autonomous mode (Rahimi and Karwowski [1990]). Furthermore, it has been established in Yamada et al. [1997] that the static and dynamic tolerance contact force F_c — with a minimum contact area of 0.0015 m^2 — is 50 N for a human being.

First, the superiority of the contact index — based on (4.10) — using the pendulum-on-a-moving-cart dynamics is demonstrated in comparison to the other two methods — based respectively on (4.11) and (4.12) — proposed in Section 4.3.7, namely the acceleration index and the position index. The thresholds for the three different collision detections are summarized in table 4.1 for each LIP joint, i.e., each direction. The unloaded state allowing a smaller range of motion than the loaded state for the vertical LIP joint (Sarrus mechanism), it is thus required to have different position thresholds depending on whether or not a payload is grasped by the end-effector.

TABLE 4.1 – Thresholds for collision detection.

Joints	X	Y	Z
$c_{lim}(m/s^2)$	0.42	0.42	0.5
$a_{lim}(m/s^2)$	0.5	0.5	1
$p_{lim}(m)$	0.06	0.06	unloaded : 0.01 ; loaded : 0.05

Fig. 4.11 shows a collision detection in the horizontal Y-direction using the acceleration index. The autonomous motion was set to reach a speed of 0.5 m/s until the impact. In this case the contact index was inactive in order to show that the acceleration index could potentially lead to similar detection timing results. Indeed, with a small acceleration threshold a_{lim} the collision detection can be quite fast but can be falsely triggered when higher autonomous accelerations are desired. For this reason, a_{lim} is usually set above 0.7 m/s^2. However, the worst case, if there is only an acceleration index, would be a compliant collision unable to trigger the detection.

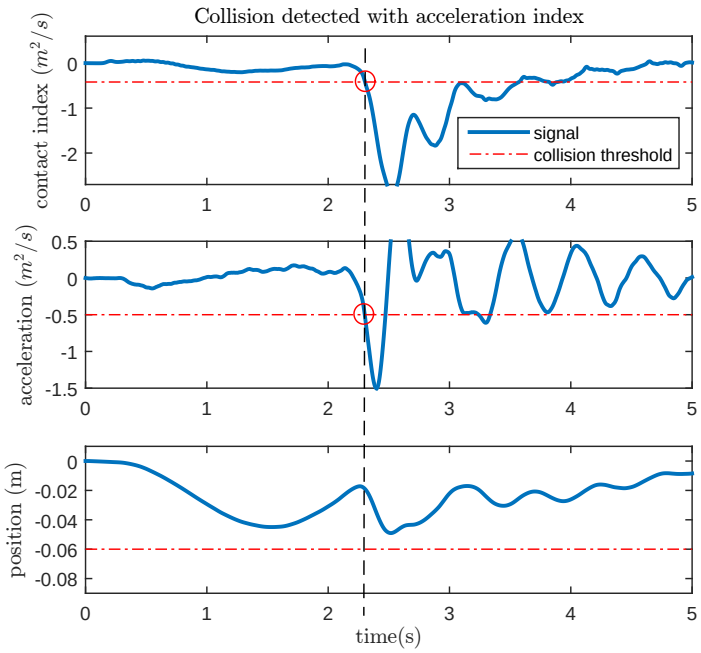

FIGURE 4.11 – Collision detected with the acceleration index (contact index inactive). The red circles identify the points where the thresholds are reached and the collision detection is triggered. In this case, the contact index and the acceleration index are reached at the same time, without triggering the position index.

This issue is demonstrated in Fig. 4.12 where the collision is detected by the position index but not the acceleration one. In this case, the inactive contact index detected the collision 0.5 s earlier than the position index. The contact index detects on average a collision within 0.1 to 0.2 second depending on the manipulator velocity. The contact index is therefore faster to respond and more reliable than the two basic collision detections.

The enhanced safety provided by the collision detection is now discussed by considering the forces generated by a collision with two different surfaces, namely a static hard wooden surface and a compliant human hand. The robot's end-effector reaches a speed between 0.5 and 0.6 m/s before it hits the surfaces. As expected, the collision with the rigid surface produces larger impact forces. However, the peak force is never above 30 N, as depicted in Fig. 4.13, and remains much smaller than the pain tolerance limit F_c of 50 N. It is also interesting to see in Fig. 4.13 that a collision with an unconstrained human hand generates forces smaller than 10 N. The collision detection specially developed for the active-passive uMan leads to a safe shared human-robot workspace.

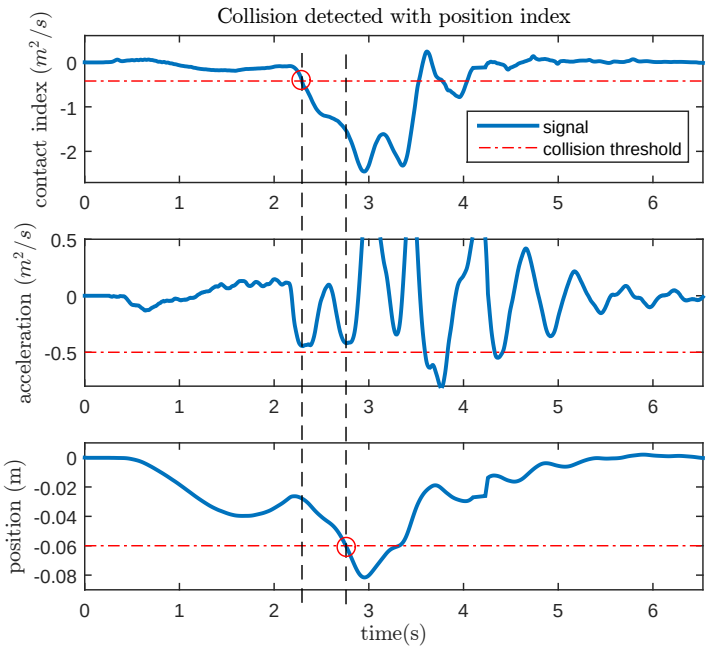

FIGURE 4.12 – Collision detected with the position index (contact index inactive). The red circles identify the points where the thresholds are reached and the collision detection is triggered. In this case, the contact index, if activated, would have triggered the collision detection before the position index, without triggering the acceleration index.

4.4.2 Peg-in-hole validation

The second feature to be assessed is the ease of fine manipulation and its resulting effectiveness. Unfortunately, the ease of manipulation is not a feature that can be directly measured like inertia and interaction forces. For this reason, a specific peg-in-hole task has been designed to assess the two main features that can be used to define the ease of manipulation, namely effort and intuitiveness. Using this specific peg-in-hole task, the uMan is compared to the state-of-the-art admittance control commonly used in pHRI (Lecours et al. [2012]). The set-up for the task consisted of a 4-hole rectangular pattern and a peg appended to the uMan's end-effector carrying a payload of 11.4 kg (25 lbs) as illustrated in Fig. 4.14. The peg has a diameter of 25.70 mm while the holes have a diameter of 26.00 mm. The admittance control is used with the three LIP joints completely locked and with the end-effector force/torque sensor as the operator inputs. A second force/torque sensor, mounted on the peg, is used to record the contact forces with the environment. The admittance parameter values used for this task are found heuristically in order to generate the fastest motions possible without producing unstable contacts ($m = 35\ kg$ and $c = 396\ Ns/m$ for the axis normal to the task surface).

Three tests were performed, namely, a 4-hole run in 30 seconds with the admittance control (as fast as possible), a 4-hole run in 30 seconds with the uMan (in order to match the admit-

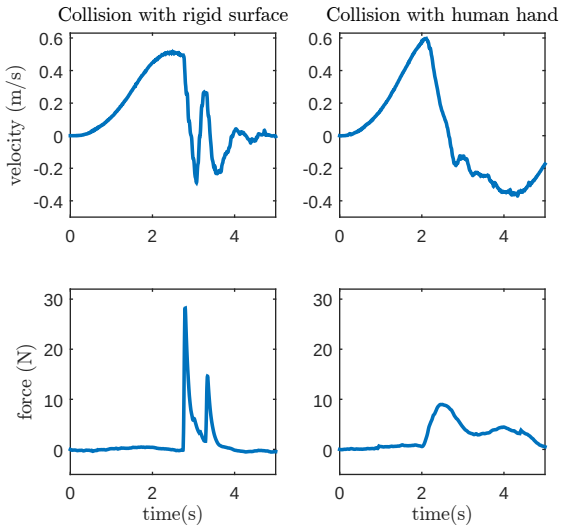

FIGURE 4.13 – Examples of the normal forces generated by collision of the uMan with different environments during an autonomous motion.

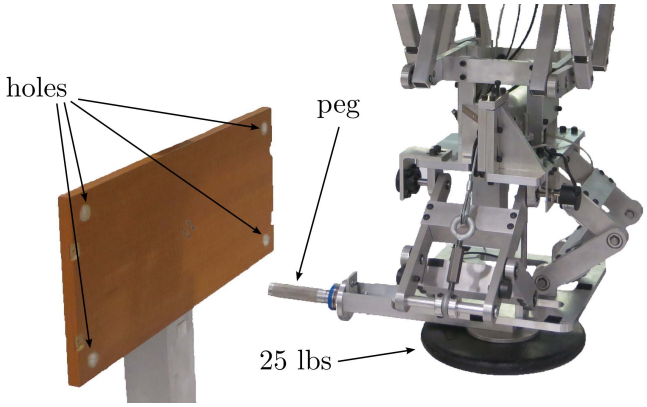

FIGURE 4.14 – Set-up for the peg-in-hole task.

tance execution time), and a 4-hole run in 14 seconds with the uMan (as fast as possible). The 30-second admittance and 30-second uMan runs are performed in order to compare the forces applied by the operator and generated on the environment with controlled speed and acceleration. This comparison gives a measure of the reduction of the human effort provided by the uMan, for a given task. The fast uMan run is then performed in order to compare — with the 30-second admittance run — the speed of execution and the required operator force to achieve similar environment forces. This comparison gives a measure of the improvement in the intuitiveness.

An example of the forces generated on the environment for a peg insertion and peg pull out during an admittance control and a 30-second uMan run is shown in Fig. 4.15. It can be observed that the 30-second uMan peg insertion force at about 0.8 second is approximately

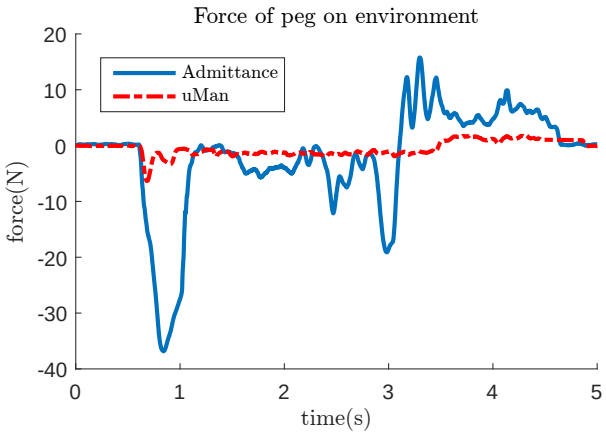

FIGURE 4.15 – Example of the normal forces generated on the rigid environment during the peg-in-hole task for the admittance control and the uMan for the 30-second tests.

four times smaller than the admittance control peg insertion force. This result is confirmed with the box plots shown in Fig. 4.16, representing two runs of each test, i.e., eight peg insertions.

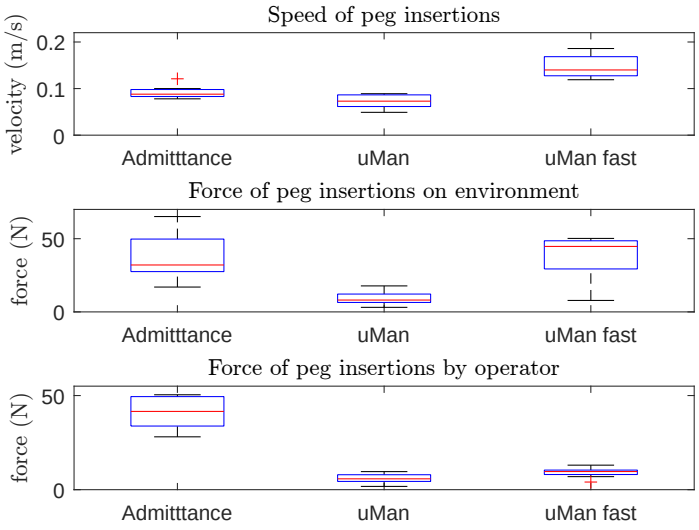

FIGURE 4.16 – Examples of the normal forces applied on the rigid environment during the peg-in-hole task for the admittance control and the uMan. The boxplots give the minimum, maximum, first quartile, third quartile, and median values for each test, including eight peg insertions.

Indeed, it is clear, from Fig. 4.15 and Fig. 4.16, that for the same execution speed, the uMan requires significantly smaller forces from the operator and produces smaller forces on the

environment. These results demonstrate that the exact same task can be executed with considerably less effort using the uMan than using the admittance control. It is also shown that the uMan can performed the peg insertion twice as fast as with the admittance control while generating similar forces on the environment but with smaller operator forces. The uMan's speed advantage, which also requires smaller operator forces than for the slower admittance control, demonstrates its superior intuitiveness. These conclusions are also true for the forces generated during peg pull outs, excepted that the fast uMan forces on the environment are much smaller (around 10 N).

Therefore, due to its resulting ease of manipulation, the macro-mini uMan enables fast and low-impedance interactions with constrained and unconstrained environments. As mentioned in the first part of this chapter, the main reasons for the effectiveness of the uMan is that its macro-mini architecture allows a complete decoupling of the dynamics of the robot and of the human operator, due to the redundant active (macro) and passive (mini) joints. With this architecture, all the work in the manipulative space is done by the human operator, therefore minimizing the mechanical impedance.

4.4.3 Assembly tasks validation

The last feature to be evaluated is the adaptability of the uMan to different industrial contexts. In order to demonstrate this feature, mock-ups of real assembly tasks were tested in the laboratory. A simple user interface, shown in Fig. 4.17, was also developed in order to provide an intuitive and adaptable communication channel and programming interface between the operator and the uMan.

Three simultaneous means of interaction were possible with the uMan : a physical interaction with the end-effector, a remote controller attached to the end-effector, and a graphical user interface (GUI) on a computer screen. The physical interaction provided the cooperative motion, the collision detection, and the automatic return trigger. The remote controller was directly linked to the GUI and included a button for each feature present in the GUI.

The first mock-up validation is a trunk deck lid attachment application (deck lid : 11.2 kg). A picture of the interaction is presented in Fig. 4.18. A specific state machine, shown in Fig. 4.19, is designed in order to cover all aspects of a practical deck lid attachment task.

Using a physical interaction with the uMan, the operator has to define the pick-up, place-down, and certain way point locations for the autonomous trajectory. The autonomous mode is then launched, i.e., the robot fetches the first deck lid. Once the first deck lid has reached the operator's workstation, a screwing task is performed in cooperation with the uMan in order to maintain the deck lid in place. The uMan is then sent back to fetch the second deck lid while the operator is finishing the first deck lid installation. A collision and a hands-on-payload interaction is then performed with the second deck lid in order to complete the

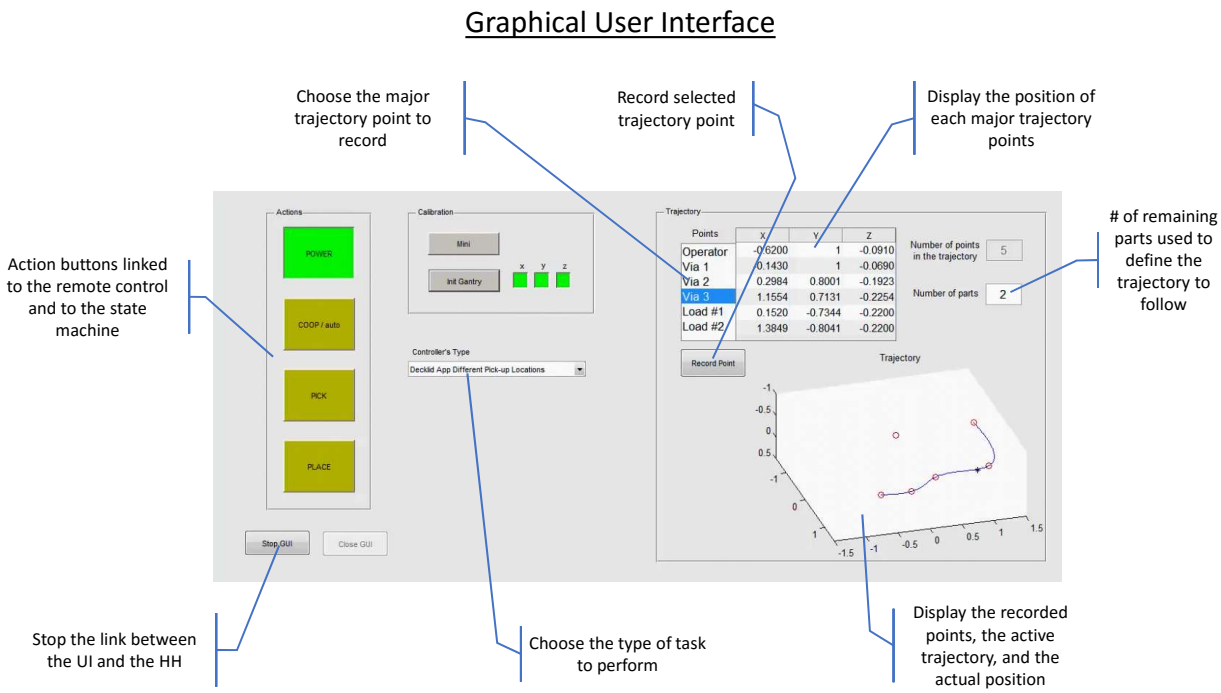

FIGURE 4.17 – Graphical user interface specifically designed for the uMan.

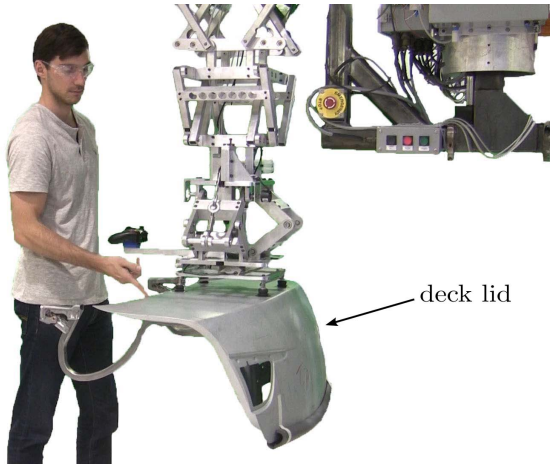

FIGURE 4.18 – Laboratory set-up used to emulate the assembly of a deck lid on a vehicle.

planned trajectory with a physical human-robot cooperation. In short, this task involves a simple trajectory/task teaching, an autonomous motion towards the part and towards the operator working zone, an autonomous part pick-up, a cooperative motion, a cooperative screwing task, and a collision detection.

The deck lid demonstration assessed the capabilities of the uMan to operate safely in the same workspace as a human being and to improve the operator's efficiency while reducing the

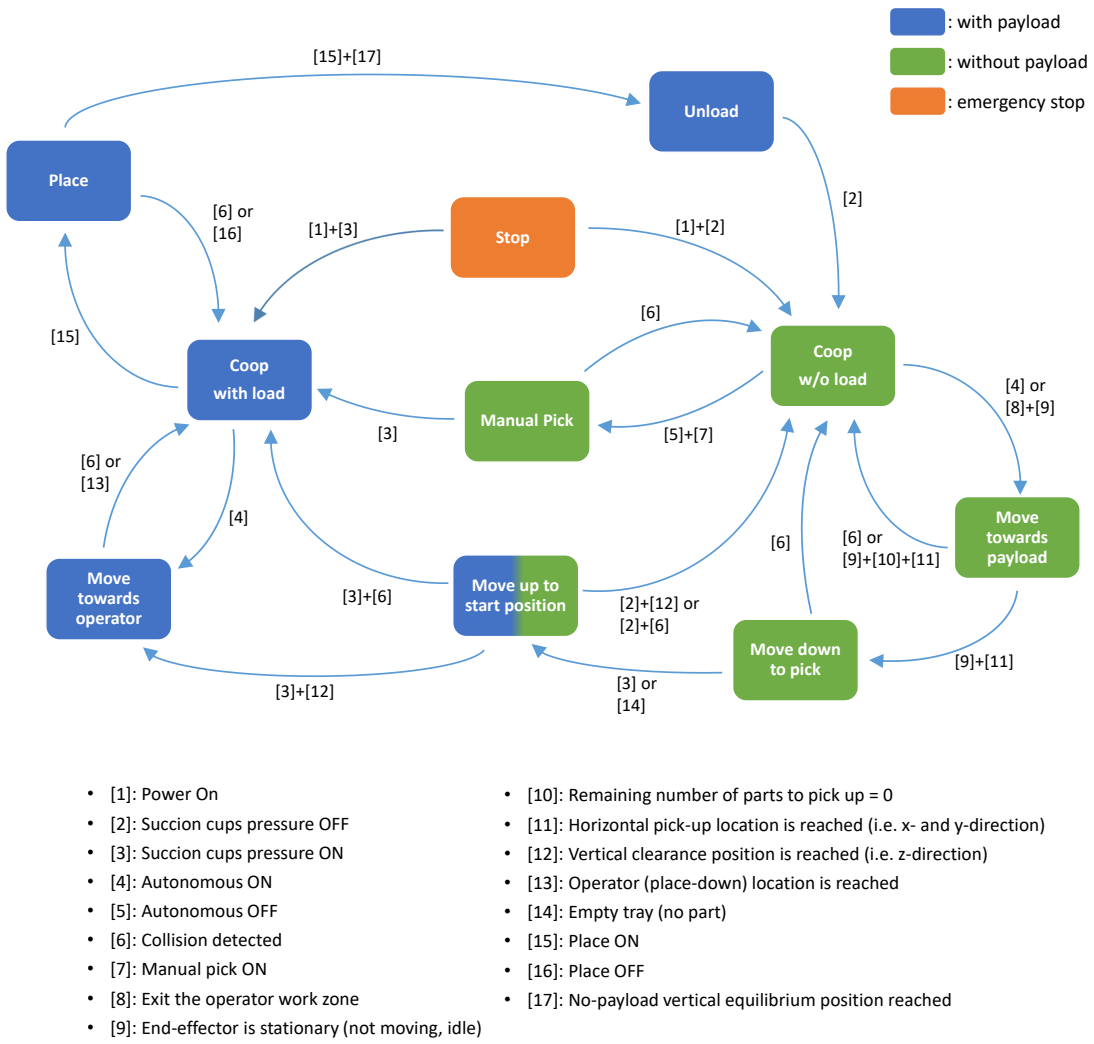

FIGURE 4.19 – State machine diagram for the deck lid application.

required physical efforts. In particular, the low impedance interaction makes the adjustment and screwing task much easier than with an admittance controller because of the natural and intuitive response of the uMan to the operators fine motions.

The second validation is a mock-up battery insertion application (mock-up battery : 10 kg). A picture of the interaction is presented in Fig. 4.20.

In this validation, the operator has to pick up the mock-up battery with an off-centred end-effector using a physical human-robot interaction. Once the battery is picked up, the operator has to perform a tight in-and-out insertion task that is not feasible without the assistance of the uMan. In short, this task involves a cooperative pick and place, a cooperative precise positioning, and a demonstration of the stability in the presence of rigid contacts as well as

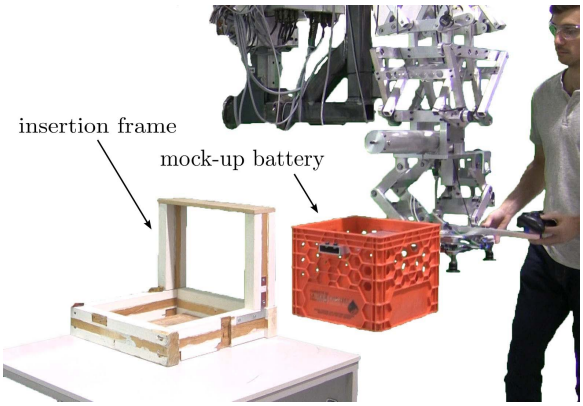

FIGURE 4.20 – Laboratory set-up used to emulate the insertion of a battery in the tight housing of a vehicle.

the direct environment feedback to the operator.

The mock-up battery insertion application assessed the capabilities of the uMan to enable cooperative fine manipulations with an off-centred payload and to allow hard contacts with any environment. The direct feedback to the operator of the contacts with the environment is provided by the low-impedance mini manipulator and yields a very stable and intuitive interaction.

4.5 Video demonstrations

Four videos showing the different experimental validations are available at

http://robot.gmc.ulaval.ca/publications/these-de-doctorat

The collision detection video demonstrates the impacts with the rigid surface and with the human hand, as well as different interferences during autonomous motion (*Chap4_ Collisions.mp4*). The peg-in-hole video shows the speed advantage of the uMan over the admittance control (*Chap4_ Peg_ in_ Hole.mp4*). The deck lid video shows the trajectory recording with the user interface as well as the execution of the mixed autonomous/collaborative deck lid installation(*Chap4_ Decklids.mp4*). Finally, the battery video demonstrates the tight insertion task, the stable bilateral contacts and the direct feedback using the mock-up battery (*Chap4_ Battery.mp4*).

4.6 Conclusion

This chapter introduced a novel underactuated macro-mini architecture adapted for pHRI in an industrial context, namely the uMan (underactuated manipulator). The mechanical design and the resulting advantages of the low-impedance passive joints (X, Y and Z motion) were described in detail. The advanced control of the uMan was then presented together with the

recommended approach for the trajectory planning and the new dynamics-dependent collision detection. The results of the experimental validations were then presented and discussed in order to demonstrate that the concepts developed in this work provide low-impedance physical interaction, which yields a very intuitive and effective manipulation environment as well as a safe cooperative workspace. Considering these positive results, the uMan is believed to have the potential to lead to effective architectures of robotic assistants.

4.7 Appendix

4.7.1 uMan parameters

The filter used for the error signal e_f in equation (4.2) is a first-order low-pass filter with a cutoff frequency of 0.318 Hz. It is also important to reiterate that for the cooperative mode the diagonal components of the gain matrix $\mathbf{K}_{Pt}$ were set to zero for redundancy in the algorithm, although this is not mandatory.

TABLE 4.2 – Control parameters.

Joints	X	Y	Z
K_{Pt}	7	7	7
$K_{P\theta}$	5	7.5	4
K_D	1	1	0
K_F	4	0	1
K_{NL}	0.25	0.5	0
l	0.6	0.6	0.2848
$x_{\theta znorm}$	0.008	0.008	–

TABLE 4.3 – Range of motion.

Joints	X	Y	Z
$HIA(m)$	3.30	2.15	0.52
$LIP(m)$	0.190	0.190	unloaded : 0.036 ; loaded : 0.100

4.7.2 Validation of the low effective impedance using the first prototype

It is desired to obtain a robotic manipulator that can effectively follow a human being's interaction capabilities. To this end, it is required to reduce the control delay — if not eliminate it completely — and to respond quickly to high frequency inputs whatever payload the robot carries. In order to assess the effectiveness of the macro-mini (active-passive) mechanism proposed in this work, some preliminary tests were performed to compare the first prototype of the proposed architecture to a fully actuated robot using the state-of-the-art admittance control with optimal parameters.

Test-Bench Design

In order to fairly compare both architectures, during the experimentation, the mini component is always appended to the macro manipulator, however the passive joints are locked for the fully actuated experiment. Using this approach, the prototype keeps the same weight and interaction set-up for both experiments which minimizes the undesirable experimental variations. The mini component of the prototype, attached to a 3-dof actuated gantry system, is shown in figure 4.21 with an example of a passive motion, and the complete macro-mini manipulator is shown in figure 4.22.

FIGURE 4.21 – LIP (mini) component of the macro-mini robotic manipulator attached to a 3-dof gantry structure (macro, not shown here). This architecture allows the x and y horizontal motions.

The mini component includes two identical four-bar passive parallelogram structures mounted orthogonally in series and each generating a pendulum dynamics. The length of the vertical bars are designed to be long enough in order to obtain a large radius of curvature, here 35.5 cm, and thereby, to emulate horizontal motions in x and y. The nonlinear parasitic z-motion (vertical motion) due to the pendulum-type architecture generates a vertical force, which increases with the motion angle and the payload weight, and that passively brings the end-effector back to its equilibrium configuration. However, this return force also acts against the operator's ease of motion for large displacements. Indeed, the parasitic z-motion increases with the pendulum angle, which in turn increases the fraction of the weight of the payload that the operator has to support. To counter this effect, the nonlinear function for the macro-mini controller is chosen as

$$f_{NL}(\Delta z) = \text{sign}(\Delta x) k_z \Delta z \tag{4.13}$$

with

$$\Delta z = l[1 - \cos(\Delta\theta)] \tag{4.14}$$

where k_z is a gain used to modulate the compensation on the horizontal motions proportionally to the z-displacement of the end-effector, Δz. Parameter l is the radius of curvature of the

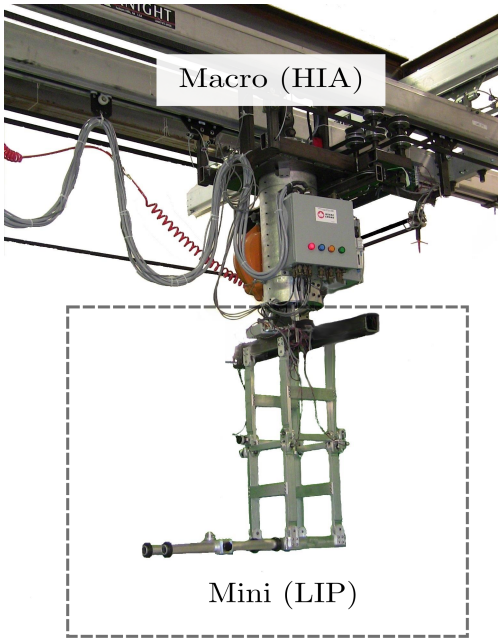

FIGURE 4.22 – Macro-mini manipulator. Macro : 3-dof gantry manipulator. Mini : 2-dof passive mechanism (horizontal motions).

pendulum and $\Delta\theta$ is the angle produced by the pendulum's displacement from its equilibrium point. For both horizontal motions, namely x and y, the corresponding angle is read by an encoder located at a rotational joint on each parallelogram. A 6-dof force/torque sensor is also mounted between the operator handle and the end-effector in order to read the applied forces. Conveniently, the handle can also support a variety of payloads.

When the passive joints are locked, for the macro-only version of the robot, the force/torque sensor is used to measure the operator's input force and control the macro manipulator. Therefore, the admittance control described in section 4.3 is used in that case (it is recalled that the force/torque sensor is not used for control purposes in the macro-mini version of the robot). In order to obtain the lowest possible impedance, the smallest parameters, m and c, that generate stable interactions, have been found heuristically for that specific experimental set-up.

Each passive parallelogram has a mass of approximatively 9 kg. Therefore, the mini component of the robot has a total mass of 18 kg while the high-inertia macro has an equivalent moving mass of 500 kg in the direction of x-axis and 350 kg in the direction of y-axis. [2] The control parameters for the macro-mini manipulator are

$$k_P = 6,\ k_D = 1.5,\ k_z = 0.1,\ \text{and}\ l = 0.355\ m,$$

2. The macro component of the manipulator was designed for large payloads. Its architecture is described in detail in Gosselin et al. [2013].

while for the macro-only manipulator the selected parameters are

$$m = 35\ kg \text{ and } c = 80\ Ns/m.$$

It is also important to mention that a payload of 16 kg (35 lbs) was mounted on the handle for the experimentation, leading to a total moving mass of 384 kg in the y-axis. The desired inertia reduction is thus more than 10 times the actual inertia making the chosen admittance parameters in fact quite low for such a system, but still optimal for this experimental set-up.

Results and discussion

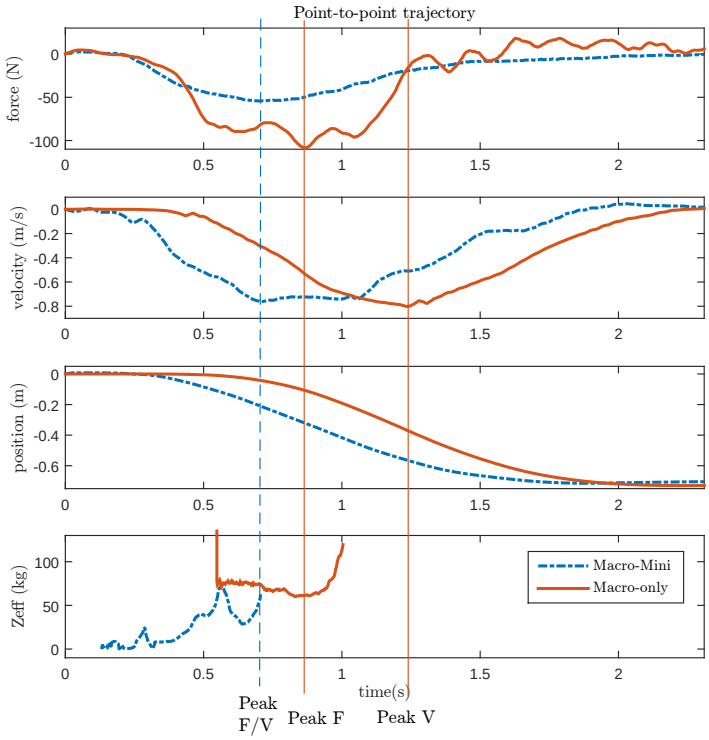

FIGURE 4.23 – Force, velocity and position responses, and effective impedance felt by the operator during the acceleration phase for the point-to-point task with the macro-mini (in dashed blue) and the macro-only manipulator (in solid red). Peak F and Peak V represent respectively the peak force and velocity of each manipulator.

The preliminary tests that were conducted to assess the performance of the macro-mini architecture are simple point-to-point tasks for which the input force, the velocity and position of the payload, and the effective impedance felt by the operator are studied. Example experimental results for a 0.7 m linear displacement in the direction of the y-axis of the robot are shown in figure 4.23. The results for the macro-mini manipulator are represented by blue dashed lines, while the results for the macro-only manipulator are represented by red solid lines. For this specific task, the operator had to bring the payload to the 0.7 m target as fast as

possible with a velocity limit of 0.8 m/s of the active joint of the macro. Several improvements can be noticed with the macro-mini robot in comparison to the macro-only robot. The first important benefit is the absence of delay in the response. Indeed, it can be observed that, for the macro-mini robot, the motion is engaged immediately when an input force is applied to the system (at about 0.2 s), whereas the macro-only robot induces a delay of approximately 0.3 s. This delay can be easily observed when considering the elapsed time between the peak force ($Peak\ F$) and the peak velocity ($Peak\ V$) of each response, as indicated in Figure 8. Indeed, it can be observed that the peak force and the peak velocity coincide in the case of the macro-mini robot while the peaks are separated by a delay of 0.3 s in the case of the macro-only robot. This delay is clearly perceptible by the operator and makes the interaction significantly less intuitive (the operator feels that they are dragging the robot). In both cases the velocity constraint was reached, but the macro-mini plateaued for a period of 0.4 s which means that it could have fulfilled the task even faster considering the exact same input force if the velocity limitation had been higher. Actually, the amount of force required to attain the peak velocity is also a strong positive for the low-impedance interaction achieved with the passive system. Effectively, the necessary force to achieve 0.8 m/s was approximately 50 N for the macro-mini while it was required to apply twice the force for the macro-only robot (approximately 100 N). This result can be a major issue for pHRI, regarding safety, efficiency, and ergonomic considerations.

Another well-known problem in pHRI can be observed on the input force graph where a tight virtual mass reduction can generate an unstable behaviour. Here, for the macro-only robot, the high impedance of the macro mechanism combined with the stiff dynamics of the interaction apparatus (force/torque sensor, payload, parallel bars) produces an oscillating force input that requires higher admittance parameters in order to be filtered. Failing to do so would lead to discomfort for the operator or simply to an uncontrollable interaction. In order to further compare the two manipulator architectures, the effective impedance felt by the operator during the acceleration phase is plotted in figure 4.23. Here, the effective impedance is computed as an effective inertia, as follows

$$Z_{eff} = m_{eff} = f/a; \tag{4.15}$$

where f is the force applied by the operator and a is the acceleration of the end-effector. Obviously, in the portion of the trajectory where the acceleration is close to zero, the computed effective impedance becomes too large to be significant. The effective impedance is therefore not shown on the graph for these portions of the trajectory. For the macro-only manipulator with the optimal admittance parameters, the impedance felt is extremely high before the end of the delay and then it is quasi-constant between 60 to 76 kg. The macro-mini leads to a lower effective admittance, namely a short peak at 24 kg — which roughly corresponds to the passive mechanism plus payload weight ($16 + 9 = 25\ kg$) — is observed before the end of the slight delay. The impedance then drops to 8 kg, and then slowly increases, due to gravity, to an effective impedance peak at around 70 kg that directly implies that the limit of the range

of motion of the passive mechanism is reached. Indeed, this inertia is close to the limit in impedance reduction achieved by the macro-only manipulator.

In summary, the macro-mini mechanism eliminates the inherent delay, requires less than half the force to achieve the same velocity, generates a more stable interaction, and reduces considerably the effective impedance during the acceleration phase. Results obtained with other trajectories confirm the above observations.

4.7.3 Video demonstration

The accompanying video demonstrates the effectiveness of the macro-mini robotic manipulator (*Annexe_ Chap4_ Low_ Impedance.mp4*). The first part shows the intuitive interaction with the robot for large and fine motions without any payload, followed by an interaction with a 16 kg (35 lbs) payload. The fast point-to-point task is then presented for both the macro-mini and the macro-only mechanisms with the 16 kg payload. The video is available at

http://robot.gmc.ulaval.ca/publications/these-de-doctorat

Conclusion

L'approche générale et les solutions proposées dans cette thèse contribuent directement à l'amélioration et à l'implantation d'interactions physiques humain-robot efficaces en industrie. En effet, afin d'atteindre une collaboration intuitive, efficace et sécuritaire, plusieurs aspects contraignants de la robotique coopérative sont étudiés dans ce travail. Ces aspects contraignants sont les contacts bilatéraux à hautes fréquences, l'utilisation d'architectures de commande différentes pour chaque type d'interaction nécessitant des lois de commutations complexes, les efforts engendrés par l'opérateur durant la coopération, la stabilité favorisée au détriment de la performance, la sécurité dans l'espace de l'opérateur et le niveau intuitif de l'interaction.

Pour les manipulateurs entièrement actionnés, les solutions proposées sont une loi de commande en admittance variable unifiée pour les interactions unilatérales et bilatérales, une amplification efficace des forces de l'opérateur, un algorithme d'optimisation permettant d'affiner les lois de commande à des performances qui se trouvent aux limites de la stabilité robuste, et ce, peu importe la configuration d'un robot à plusieurs degrés de liberté et, finalement, une interaction physique sur la totalité de la structure actionnée du robot.

Pour les manipulateurs combinant des articulations actives et passives tel que le uMan, les solutions sont une loi de commande unique régissant simultanément les modes autonome et coopératif, une réduction de l'impédance ressentie par l'opérateur en-dessous des standards en pHRI, une interaction physique sur toute la structure accessible à l'opérateur (mini manipulateur), une détection de collision hautement réactive menant à des actions autonomes sécuritaires dans l'espace de travail de l'opérateur et, finalement, des interactions bilatérales générant un retour d'effort direct (sans délais) à l'opérateur grâce aux articulations passives.

Au final, deux approches principales d'interaction sont présentées, une pour chaque type d'architecture de manipulateur robotisé étudié, à savoir, entièrement actionné et macro-actif avec mini-passif. Chaque approche a ses propres avantages et inconvénients, mais les deux définissent des techniques avancées et viables de coopération humain-robot intuitives directement applicables à l'industrie d'assemblage.

Futures avancées

Les concepts développés dans cette thèse ont le potentiel d'être approfondis et même d'engendrer de nouvelles contributions. Quelques idées sont présentées ici :

Premièrement, sachant que la commande en admittance bilatérale avec deux capteurs ne répond pas aussi rapidement que la commande développée avec les articulations passives, mais qu'elle permet de générer une amplification des efforts de l'humain sur l'environnement, il serait intéressant d'étudier la possibilité de combiner les deux. En effet, en ajoutant une compliance qui est mesurée (ex : encodeur) à l'articulation qui inclut le capteur d'efforts, il serait possible d'obtenir des contacts à très hautes fréquences stables et hautement réactifs (sans délais à l'impact), tout en ayant accès à l'amplification.

Deuxièmement, une nouvelle architecture parallèle pour le mini manipulateur basée sur le concept du tripteron (Kong and Gosselin [2002]) est actuellement à l'étude. Ce nouveau mécanisme permet de réduire le poids et le volume du mini, mais permet surtout de rendre l'effort nécessaire pour déplacer le pendule des articulations horizontales indépendant de la charge utile. Le prototype du mécanisme est montré à la Fig. 4.24.

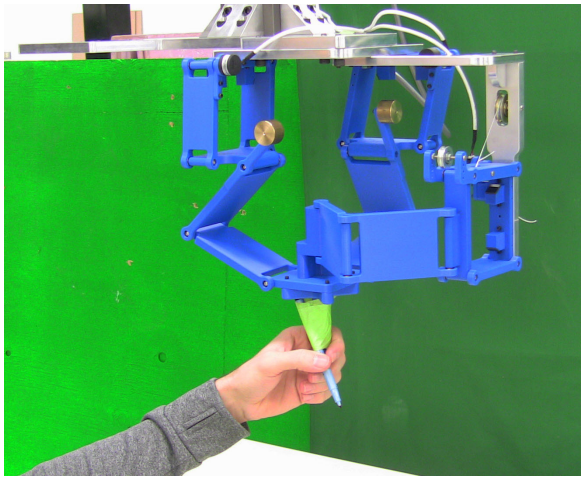

FIGURE 4.24 – Prototype du mécanisme parallèle tripteron (mini manipulateur) monté sur un système gantry (macro manipulateur).

Finalement, une nouvelle planification de trajectoire, basée sur la deuxième option présentée à la Section 4.3.6, devra être optimisée et testée afin de valider la réduction réelle de la dérivée de l'accélération et afin d'atteindre le plein potentiel de l'architecture de robot collaboratif proposé dans cette thèse.

Who you are is defined by the values you are willing to struggle for.

Mark Manson

Bibliographie

P. Akella, M. Peshkin, Ed Colgate, W. Wannasuphoprasit, N. Nagesh, J. Wells, S. Holland, T. Pearson, and B. Peacock. Cobots for the automobile assembly line. In *IEEE International Conference on Robotics and Automation (ICRA)*, volume 1, pages 728–733, 1999. doi : 10.1109/ROBOT.1999.770061.

A. Albu-Schäffer, C. Ott, and G. Hirzinger. A unified passivity-based control framework for position, torque and impedance control of flexible joint robots. *The International Journal of Robotics Research*, 26(1) :23–39, 2007. doi : 10.1177/0278364907073776.

R. H. Bartels, J. C. Beatty, and B. A. Barsky. *An Introduction to Splines for Use in Computer Graphics & Geometric Modeling*. Morgan Kaufmann Publishers Inc., San Francisco, CA, USA, 1987. ISBN 0-934613-27-3.

T. L. Brooks. Telerobotic response requirements. In *IEEE International Conference on Systems, Man and Cybernetics*, pages 113–120, Nov 1990. doi : 10.1109/ICSMC.1990.142071.

S.P. Buerger and N. Hogan. Complementary stability and loop shaping for improved human-robot interaction. *IEEE Transactions on Robotics*, 23(2) :232–244, April 2007. ISSN 1552-3098. doi : 10.1109/TRO.2007.892229.

B. Cagneau, G. Morel, D. Bellot, N. Zemiti, and G.A. d'Agostino. A passive force amplifier. In *IEEE International Conference on Robotics and Automation (ICRA)*, pages 2079–2084, 2008. doi : 10.1109/ROBOT.2008.4543513.

A. Campeau-Lecours, S. Foucault, T. Laliberté, B. Mayer-St-Onge, and C. Gosselin. A cable-suspended intelligent crane assist device for the intuitive manipulation of large payloads. *IEEE/ASME Transactions on Mechatronics*, 21(4) :2073–2084, 2016. ISSN 1083-4435. doi : 10.1109/TMECH.2016.2531626.

S.K. Chan and P.D. Lawrence. General inverse kinematics with the error damped pseudoinverse. In *IEEE International Conference on Robotics and Automation*, pages 834–839 vol.2, 1988. doi : 10.1109/ROBOT.1988.12164.

P. H. Chang and J. Kim. Telepresence index for bilateral teleoperations. *IEEE Transactions on Systems, Man, and Cybernetics, Part B : Cybernetics*, 42(1) :81–92, Feb 2012. ISSN 1083-4419. doi : 10.1109/TSMCB.2011.2160849.

A. Cherubini, R. Passama, A. Crosnier, A. Lasnier, and P. Fraisse. Collaborative manufacturing with physical human–robot interaction. *Robotics and Computer-Integrated Manufacturing*, 40 :1 – 13, 2016. ISSN 0736-5845. doi : http://dx.doi.org/10.1016/j.rcim.2015.12.007.

N.P. Chironis. *Mechanisms and mechanical devices sourcebook*. New York : McGraw-Hill, 1991.

Ed Colgate and N. Hogan. An analysis of contact instability in terms of passive physical equivalents. In *IEEE International Conference on Robotics and Automation (ICRA)*, pages 404–409 vol.1, May 1989. doi : 10.1109/ROBOT.1989.100021.

J. E. Colgate. Coupled stability of multiport systems—theory and experiments. *Journal of Dynamic Systems, Measurement, and Control*, 116(3) :419–428, Sep 1994. doi : 10.1115/1.2899237.

J. E. Colgate and N. Hogan. Robust control of dynamically interacting systems. *International Journal of Control*, 48(1) :65–88, 1988. doi : 10.1080/00207178808906161.

J.E. Colgate. Robust impedance shaping telemanipulation. *IEEE Transactions on Robotics and Automation*, 9(4) :374–384, Aug 1993. ISSN 1042-296X. doi : 10.1109/70.246049.

J.E. Colgate and J.M. Brown. Factors affecting the z-width of a haptic display. In *IEEE International Conference on Robotics and Automation (ICRA)*, pages 3205–3210 vol.4, May 1994. doi : 10.1109/ROBOT.1994.351077.

J.E. Colgate, M. Peshkin, and S.H. Klostermeyer. Intelligent assist devices in industrial applications : a review. In *IEEE/RSJ International Conference on Intelligent Robots and Systems (IROS)*, volume 3, pages 2516–2521 vol.3, 2003. doi : 10.1109/IROS.2003.1249248.

A. De Santis, B. Siciliano, A. De Luca, and A. Bicchi. An atlas of physical human-robot interaction. *Mechanism and Machine Theory*, 43(3) :253–270, 3 2008. ISSN 0094-114X. doi : 10.1016/j.mechmachtheory.2007.03.003.

V. Duchaine and C.M. Gosselin. General model of human-robot cooperation using a novel velocity based variable impedance control. In *EuroHaptics Conference and Symposium on Haptic Interfaces for Virtual Environment and Teleoperator Systems*, pages 446–451, 2007. doi : 10.1109/WHC.2007.59.

S.D. Eppinger and W.P. Seering. Understanding bandwidth limitations in robot force control. In *IEEE International Conference on Robotics and Automation (ICRA)*, volume 4, pages 904–909, 1987. doi : 10.1109/ROBOT.1987.1087932.

F. Ficuciello, A. Romano, L. Villani, and B. Siciliano. Cartesian impedance control of redundant manipulators for human-robot co-manipulation. In *IEEE/RSJ International Conference on Intelligent Robots and Systems (IROS)*, pages 2120–2125, Sept 2014. doi : 10.1109/IROS.2014.6942847.

C. Gosselin, T. Laliberté, B. Mayer-St-Onge, S. Foucault, A. Lecours, V. Duchaine, N. Paradis, Dalong Gao, and R. Menassa. A friendly beast of burden : A human-assistive robot for handling large payloads. *Robotics Automation Magazine, IEEE*, 20(4) :139–147, Dec 2013. ISSN 1070-9932. doi : 10.1109/MRA.2013.2283651.

A Haddadi and K. Hashtrudi-Zaad. Bounded-impedance absolute stability of bilateral teleoperation control systems. *IEEE Transactions on Haptics*, 3(1) :15–27, Jan 2010. ISSN 1939-1412. doi : 10.1109/TOH.2009.48.

S. Haddadin, M. Suppa, S. Fuchs, T. Bodenmüller, A. Albu-Schäffer, and G. Hirzinger. Towards the robotic co-worker. In Cédric Pradalier, Roland Siegwart, and Gerhard Hirzinger, editors, *Robotics Research*, volume 70 of *Springer Tracts in Advanced Robotics*, pages 261–282. Springer Berlin Heidelberg, 2011. ISBN 978-3-642-19456-6. doi : 10.1007/978-3-642-19457-3_16.

P. E. Hart, N. J. Nilsson, and B. Raphael. A formal basis for the heuristic determination of minimum cost paths. *IEEE Transactions on Systems Science and Cybernetics*, 4(2) : 100–107, July 1968. ISSN 0536-1567. doi : 10.1109/TSSC.1968.300136.

K. Hashtrudi-Zaad and S. E. Salcudean. Analysis of control architectures for teleoperation systems with impedance/admittance master and slave manipulators. *The International Journal of Robotics Research*, 20(6) :419–445, 2001. doi : 10.1177/02783640122067471.

K. Hashtrudi-Zaad and S.E. Salcudean. Transparency in time-delayed systems and the effect of local force feedback for transparent teleoperation. *IEEE Transactions on Robotics and Automation*, 18(1) :108–114, Feb 2002. ISSN 1042-296X. doi : 10.1109/70.988981.

N. Hogan. On the stability of manipulators performing contact tasks. *IEEE Journal on Robotics and Automation*, 4(6) :677–686, Dec 1988. ISSN 0882-4967. doi : 10.1109/56.9305.

K.H. Hunt. Prismatic pairs in spatial linkages. *Journal of Mechanisms*, 2(2) :213 – 230, 1967. ISSN 0022-2569. doi : http://dx.doi.org/10.1016/0022-2569(67)90042-0.

K. Irino, T. Tsumugiwa, and R. Yokogawa. Development of mechanical regulator of physical human-robot interaction to stabilize the impedance control in a constraint state (in japanese). *Transactions of the Japan Society of Mechanical Engineers Series C*, 79(802) : 2048–2061, 2013. doi : 10.1299/kikaic.79.2048.

A. Jazayeri and M. Tavakoli. Revisiting llewellyn's absolute stability criterion for bilateral teleoperation systems under non-passive operator or environment. In *IEEE/RSJ International Conference on Intelligent Robots and Systems (IROS)*, pages 70–75, Oct 2012. doi : 10.1109/IROS.2012.6385949.

L. A. Jones. Kinesthetic sensing. Technical report, Massachusetts Institute of Technology, Department of Mechanical Engineering, Cambridge, MA, 2000. URL http://bdml.stanford.edu/twiki/pub/Haptics/PapersInProgress/jones00.pdf.

H. Kazerooni. Human-robot interaction via the transfer of power and information signals. *IEEE Transactions on Systems, Man and Cybernetics*, 20(2) :450–463, 1990. ISSN 0018-9472. doi : 10.1109/21.52555.

X. Kong and C. Gosselin. Kinematics and singularity analysis of a novel type of 3-crr 3-dof translational parallel manipulator. *The International Journal of Robotics Research*, 21(9) : 791–798, 2002. doi : 10.1177/02783649020210090501.

K. Kosuge, Y. Fujisawa, and T. Fukuda. Control of robot directly maneuvered by operator. In *IEEE/RSJ International Conference on Intelligent Robots and Systems (IROS)*, volume 1, pages 49–54 vol.1, 1993. doi : 10.1109/IROS.1993.583078.

J. Krüger, T.K. Lien, and A. Verl. Cooperation of human and machines in assembly lines. *{CIRP} Annals - Manufacturing Technology*, 58(2) :628 – 646, 2009. ISSN 0007-8506. doi : http://dx.doi.org/10.1016/j.cirp.2009.09.009.

P. D. Labrecque and C. Gosselin. Performance optimization of a multi-dof bilateral robot force amplification using complementary stability. In *IEEE Conference on Control Applications (CCA)*, pages 519–526, Sept 2015. doi : 10.1109/CCA.2015.7320682.

P. D. Labrecque, J. M. Haché, M. Abdallah, and C. Gosselin. Low-impedance physical human-robot interaction using an active-passive dynamics decoupling. *IEEE Robotics and Automation Letters*, 1(2) :938–945, July 2016. ISSN 2377-3766. doi : 10.1109/LRA.2016.2531124.

P.D. Labrecque and C. Gosselin. Robotic force amplification with free space motion capability. In *IEEE International Conference on Robotics and Automation (ICRA)*, pages 134–140, May 2014. doi : 10.1109/ICRA.2014.6906600.

X. Lamy, F. Colledani, F. Geffard, Y. Measson, and G. Morel. Achieving efficient and stable comanipulation through adaptation to changes in human arm impedance. In *IEEE International Conference on Robotics and Automation (ICRA)*, pages 265–271, May 2009. doi : 10.1109/ROBOT.2009.5152294.

X. Lamy, F. Colledani, F. Geffard, Y. Measson, and G. Morel. Human force amplification with industrial robot : Study of dynamic limitations. In *IEEE/RSJ International Conference on*

Intelligent Robots and Systems (IROS), pages 2487–2494, 2010. doi : 10.1109/IROS.2010.5651677.

D.A Lawrence. Stability and transparency in bilateral teleoperation. *IEEE Transactions on Robotics and Automation*, 9(5) :624–637, Oct 1993. ISSN 1042-296X. doi : 10.1109/70.258054.

A. Lecours, B. Mayer-St-Onge, and Clement Gosselin. Variable admittance control of a four-degree-of-freedom intelligent assist device. In *IEEE International Conference on Robotics and Automation (ICRA)*, pages 3903–3908, 2012. doi : 10.1109/ICRA.2012.6224586.

Jian Li, M. Tavakoli, and Qi Huang. Absolute stability of multi-dof multilateral haptic systems. *IEEE Transactions on Control Systems Technology*, 22(6) :2319–2328, Nov 2014. ISSN 1063-6536. doi : 10.1109/TCST.2014.2301840.

Yanmei Li and Imin Kao. Stiffness control of a three-link redundant planar manipulator using the conservative congruence transformation (CCT). In *IEEE International Conference on Robotics and Automation (ICRA)*, volume 3, pages 3698–3703 vol.3, Sept 2003. doi : 10.1109/ROBOT.2003.1242164.

F. B. Llewellyn. Some fundamental properties of transmission systems. *Proceedings of the IRE*, 40(3) :271–283, March 1952. ISSN 0096-8390. doi : 10.1109/JRPROC.1952.273783.

D. W. Marquardt. An algorithm for least-squares estimation of nonlinear parameters. *Journal of the Society for Industrial and Applied Mathematics*, 11(2) :431–441, 1963. doi : 10.1137/0111030.

Fernando G. Martins. Tuning pid controllers using the ITAE criterion*. *Int. J. Engng Ed.*, 21(5) :867–873, 2005.

A. Montagner, A. Frisoli, S. Marcheschi, E. Sanchez, and M. Bergamasco. Optimal control of a robotic system for human power enhancement. In *EuroHaptics Conference and Symposium on Haptic Interfaces for Virtual Environment and Teleoperator Systems*, pages 212–218, 2007. doi : 10.1109/WHC.2007.88.

Alexander Mörtl, Martin Lawitzky, Ayse Kucukyilmaz, Metin Sezgin, Cagatay Basdogan, and Sandra Hirche. The role of roles : Physical cooperation between humans and robots. *The International Journal of Robotics Research*, 2012. doi : 10.1177/0278364912455366.

Wyatt S. Newman and Yuandao Zhang. Stable interaction control and Coulomb friction compensation using natural admittance control. *Journal of Robotic Systems*, 11(1) :3–11, 1994. doi : 10.1002/rob.4620110103.

C. Ott, A. Kugi, and G. Hirzinger. On the passivity-based impedance control of flexible joint robots. *IEEE Transactions on Robotics*, 24(2) :416–429, 2008. doi : 10.1109/TRO.2008.915438.

C. Ott, R. Mukherjee, and Y. Nakamura. Unified impedance and admittance control. In *IEEE International Conference on Robotics and Automation (ICRA)*, pages 554–561, 2010. doi : 10.1109/ROBOT.2010.5509861.

A. Packard and J. Doyle. The complex structures singular value. *Automatica*, 29(1) :71–109, 1993.

A Peer and M. Buss. Robust stability analysis of a bilateral teleoperation system using the parameter space approach. In *IEEE/RSJ International Conference on Intelligent Robots and Systems (IROS)*, pages 2350–2356, Sept 2008. doi : 10.1109/IROS.2008.4650582.

P. Pitakwatchara, S. Warisawa, and M. Mitsuishi. Force feedback augmentation method for the minimally invasive surgical system. In *IEEE/RSJ International Conference on Intelligent Robots and Systems (IROS)*, pages 1564–1569, 2006. doi : 10.1109/IROS.2006.282042.

M. Rahimi and W. Karwowski. Human perception of robot safe speed and idle time. *Behaviour & Information Technology*, 9(5) :381–389, 1990. doi : 10.1080/01449299008924252.

J. Roy and L.L. Whitcomb. Adaptive force control of position/velocity controlled robots : theory and experiment. *IEEE Transactions on Robotics and Automation*, 18(2) :121–137, 2002. ISSN 1042-296X. doi : 10.1109/TRA.2002.999642.

J.K. Salisbury. Active stiffness control of a manipulator in cartesian coordinates. In *IEEE Conference on Decision and Control including the Symposium on Adaptive Processes*, pages 95–100, Dec 1980. doi : 10.1109/CDC.1980.272026.

M. S. Shaikh and P. E. Caines. On the hybrid optimal control problem : Theory and algorithms. *IEEE Transactions on Automatic Control*, 52(9) :1587–1603, Sept 2007. ISSN 0018-9286. doi : 10.1109/TAC.2007.904451.

M. Spong. Modeling and control of elastic joint robots. *ASME Journal of Dynamic Systems, Measurement, and Control*, 109(4) :310–318, Dec 1987. doi : 10.1115/1.3143860.

T. Sugihara. Solvability-unconcerned inverse kinematics by the levenberg-marquardt method. *IEEE Transactions on Robotics*, 27(5) :984–991, 2011. ISSN 1552-3098. doi : 10.1109/TRO.2011.2148230.

T.S. Tadele, T. de Vries, and S. Stramigioli. The safety of domestic robotics : A survey of various safety-related publications. *Robotics Automation Magazine, IEEE*, 21(3) :134–142, Sept 2014. ISSN 1070-9932. doi : 10.1109/MRA.2014.2310151.

P. Tsarouchi, S. Makris, and G. Chryssolouris. Human–robot interaction review and challenges on task planning and programming. *International Journal of Computer Integrated Manufacturing*, 29(8) :916–931, 2016. doi : 10.1080/0951192X.2015.1130251.

T. Tsumugiwa, R. Yokogawa, and K. Hara. Variable impedance control with regard to working process for man-machine cooperation-work system. In *IEEE/RSJ International Conference on Intelligent Robots and Systems (IROS)*, volume 3, pages 1564–1569 vol.3, 2001. doi : 10.1109/IROS.2001.977202.

R.Q. van der Linde and P. Lammertse. Hapticmaster – a generic force controlled robot for human interaction. *Industrial Robot : An International Journal*, 30(6) :515–524, 2003. doi : 10.1108/01439910310506783.

C. W. Wampler. Manipulator inverse kinematic solutions based on vector formulations and damped least-squares methods. *IEEE Transactions on Systems, Man, and Cybernetics*, 16 (1) :93–101, Jan 1986. ISSN 0018-9472. doi : 10.1109/TSMC.1986.289285.

J.T. Wen, D.O. Popa, G. Montemayor, and P.L. Liu. Human assisted impedance control of overhead cranes. In *IEEE International Conference on Control Applications (CCA)*, pages 383–387, 2001. doi : 10.1109/CCA.2001.973895.

Jr. Wyatt, J.L., L.O. Chua, J. Gannett, I Goknar, and D. Green. Energy concepts in the state-space theory of nonlinear n-ports : Part i-passivity. *IEEE Transactions on Circuits and Systems*, 28(1) :48–61, Jan 1981. ISSN 0098-4094. doi : 10.1109/TCS.1981.1084907.

Y. Yamada, Y. Hirasawa, S. Huang, Y. Umetani, and K. Suita. Human-robot contact in the safeguarding space. *IEEE/ASME Transactions on Mechatronics*, 2(4) :230–236, 1997. ISSN 1083-4435. doi : 10.1109/3516.653047.

J. Yan and S.E. Salcudean. Teleoperation controller design using h infin ;-optimization with application to motion-scaling. *IEEE Transactions on Control Systems Technology*, 4(3) : 244–258, May 1996. ISSN 1063-6536. doi : 10.1109/87.491198.

Ping-Lang Yen and Shuo-Suei Hung. Cooperative force control of a hybrid cartesian parallel manipulator for bone slicing. *Robotica*, 31 :173–182, February 2013. ISSN 1469-8668. doi : 10.1017/S0263574712000161.